Masterarbeit Nr. 445

Experimental investigations of active and passive drag-reducing devices over a D-shaped bluff body

Philipp Oswald
Matrikelnummer 4338471

Ausgegeben: Prof. Dr.-Ing. R. Radespiel
Institut für Strömungsmechanik
Institutsleiter: Prof. Dr.-Ing. R. Radespiel
Technische Universität Braunschweig

Betreuer: Dr. Richard Semaan

Veröffentlichung: September 2017

Eidesstattliche Erklärung

Hiermit erkläre ich, Philipp Oswald, geb. am 05.10.1988, des Eides statt, die vorliegende Masterarbeit selbstständig und ohne fremde Hilfe verfasst und keine anderen als die angegebenen Hilfsmittel verwendet zu haben.

Braunschweig, 11.09.2017

Abstract

This work experimentally investigates passive and active drag-reducing devices over a D-shaped bluff body. The base configuration as well as four passive trailing edge flaps are tested at different Reynolds number. Active drag reduction through jet actuation over a Conada flap is tested in combination with open and closed loop control. Closed loop control is optimized using machine learning control with genetic programming.

Good drag reduction of up to 40 % is achieved with passive devices. Open loop control at frequencies higher than the natural vortex shedding frequency and duty cycles below 50 % yields low drag for different blowing intensities. The highest achieved drag reduction is 43 %. Blowing at the natural vortex shedding frequency was found to be detrimental. Closed loop control laws achieved comparable drag reduction to open loop control, often at similar actuation characteristics. Machine learning control also yielded efficient drag reduction control laws using one-sided actuation but those didn't achieve the same drag reduction.

Contents

Nomenclature

Latin labels

b	actuation signal
b_{open}	fixed actuation signal voltage for valve opening
C_D	drag coefficient
C_μ	momentum coefficient
d	diameter
D	drag force
f_n	natural vortex shedding frequency
h	height
I_{in}	incoming momentum
I_{out}	outgoing momentum
J	cost function
K	control law
N_i	population size
N_e	number of elite individuals
N_p	tournament size
P_c	crossover probability
P_m	mutation probability
P_r	replication probability
p	static pressure
p_0	total pressure
q	dynamic pressure
s	sensor signal
S_j	blowing slot cross-section
S_0	reference surface area
St	Strouhal number
t	time
T	period
T_{test}	testing time for one control law
u	velocity
w	width

Greek labels

α	duty cycle
γ	weighting factor

ν	kinematic viscosity
ρ	density
ζ	blowing rate

Subscripts

j	jet
∞	free stream

Abbreviations

FIFO	First In First Out
FPGA	Field Programmable Gate Array
MLC	Machine Learning Control
NSGA	Nondominated Sorting Genetic Algorithm
PIV	Particle Image Velocimetry
RANS	Reynolds Averaged Navies Stokes
URANS	unsteady Reynolds Averaged Navies Stokes
VI	Virtual Instrument
ZNMF	Zero Net Mass Flux

Chapter 1

Introduction

1.1 Motivation

A major aspect when considering the aerodynamics of a body is it's drag. A force resisting the body's movement through a fluid. For an average road vehicle about 30% of it's tractive force is lost to aerodynamic drag [19]. Assuming it is driven by an internal combustion engine with an efficiency of about 30% this means that drag accounts for about 9% of the vehicle's fuel consumption.

Naturally, it is desirable to reduce the aerodynamic drag of any body that is exposed to fluid flow. The most straight forward way would be to make it completely streamlined. However, for practical considerations, this is often not possible. Therefore many real world objects, like transport vehicles or buildings have a shape that can be described as a bluff body. This means that, relative to their length, their cross-section has a considerable height.

At high velocities the flow around bluff bodies is largely affected by flow separation and a turbulent wake forming behind the body [18]. The low pressure in the resulting dead water region accounts for most of the body's drag. In order to reduce the drag it is therefore most promising to influence the formation of vortices behind the body.

Early investigations on drag reduction of bluff bodies date back as far as 1933 when Frey [10] tested drag reduction by addition of deflector plates, but it is an ongoing field of research. For example Longa et al. [6] published an approach to reduce drag by jet actuation and linear feedback control this year.

The aim of this project is to experimentally qualify different methods for drag reduction of a D-shaped bluff body. Therefore drag measurements have been conducted at the LNB wind tunnel, situated at the Institute for Fluid Mechanics at TU Braunschweig. Passive and active drag reducing devices have been investigated. For passive drag reduction, different pairs of flaps with different geometries have been attached to the upper and lower trailing edge of the body. For active drag reduction, a pair of Coanda flaps have been attached to the back side of the model, allowing flow control through Coanda blowing.

Open and closed loop control methods are tested for their ability to efficiently reduce the drag of the body. The control law for closed loop control is optimized through a genetic algorithm. This approach to find an optimal control law is also know as machine learning control (MLC). This is the first time MLC is being implemented at this institute and to the authors knowledge also the first time it is used to control the turbulence in the wake of a D-shaped bluff body.

The flap geometries are the result of a previous study undertaken at the institute. The aim of that study was shape optimization of active and passive drag reducing devices for a D-shaped

bluff body by the use of a genetic algorithm and numerical simulation. The drag measurements of this study also serve as validation for the numerical results.

1.2 Bluff body aerodynamics

There are several different criteria that can be used to distinguish whether a body can be categorized as a bluff or a slim / streamlined body. One common criteria is the geometric shape of a body. It is considered bluff if it's dimension perpendicular to the free stream direction is comparable to it's dimension along the free stream direction. This means that even a seemingly streamlined body like a flat plate or an airfoil can become bluff bodies at an increased angle of attack. Also, a slim piece of wire spanned perpendicularly to the direction of flow is aerodynamically a bluff body, due to it's cylindrical cross-section. Another criteria to determine whether a body can be categorized as bluff is the question which component dominates it's aerodynamic drag. When the drag is dominated by viscous drag, the body is called streamlined, and when it is dominated by pressure drag, the body is called bluff.

Around streamlined bodies the flow usually stays attached to the surface. When a viscous fluid passes around the body a boundary layer forms. The flow velocity directly on the surface is zero. With increasing distance from the surface, the velocity asymptotically approaches the free stream velocity. Shear stresses within the boundary layer result in a force acting on the body in the direction of flow, called viscous drag. The aerodynamics of bluff bodies is affected by flow separation as the flow is often not able to follow the body's contour. As a result, large dead water regions can form in which the flow forms eddies and the pressure is decreased. The combination of increased pressure around the stagnation point on the front of the body and decreased pressure on it's back results in a force acting on the body in direction of the flow. This is called pressure drag. Bluff bodies are subject to viscous and pressure drag but pressure drag usually reaches higher values. Pressure drag is therefore dominating the viscous drag and is responsible for the generally higher overall drag of bluff bodies.

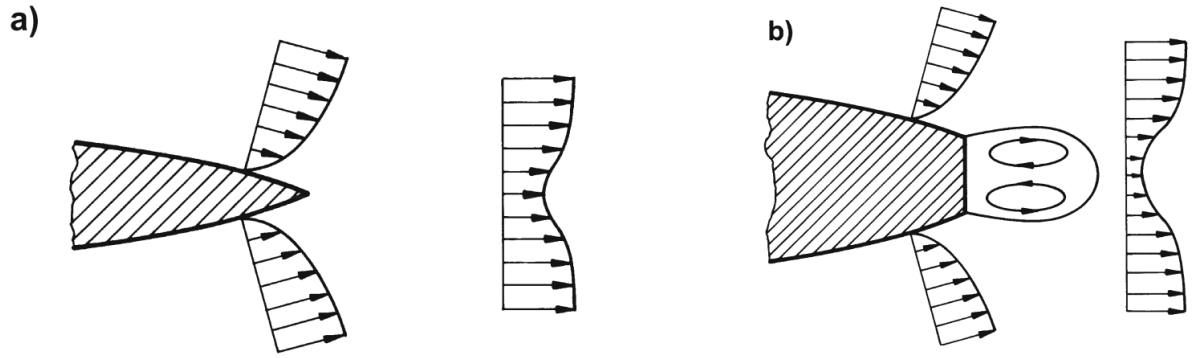

Figure 1.1: Schematic drawing of the flow over a) a streamlined and b) a bluff body [18]

In the following paragraphs, flow separation and wake formation are discussed in more detail. The presence of a body in the flow causes displacement of the fluid and the flow is therefore accelerated until it approaches the body's widest section. Flow acceleration is connected with a decrease in static pressure. After the fluid has passed the widest section, it is decelerated again and the static pressure is increasing. This is a conversion process between kinetic energy in the flow and an energy potential in the form of static pressure. During the acceleration of the flow the boundary layer has been subject to increased friction with the bodies surface and has therefore lost energy. If it's kinetic energy is not sufficient to keep up with the increase of pressure in the decelerated flow, particles in the boundary layer come to a full stop or even start

moving backwards. This causes the flow to separate from the body. The position of the separation points depends on the Reynolds number of the flow and generally moves upstream with increasing Re. A turbulent boundary layer however can move the separation point downstream again, as turbulence improves the exchange of energy between the boundary layer and the surrounding flow and therefore delays separation. This mechanism is the reason for flow separation from bluff bodies without a distinct trailing edge, like cylinders. Figure 1.2 shows a flow visualization around a cylinder for two different Reynolds numbers. Bodies with a blunt trailing edge on the other hand usually have fixed separation points at their trailing edge. The invariance of the separation point with Re also causes the drag to change less with the Reynolds number. For the example of a vertical plate there is practically no dependence at all [18].

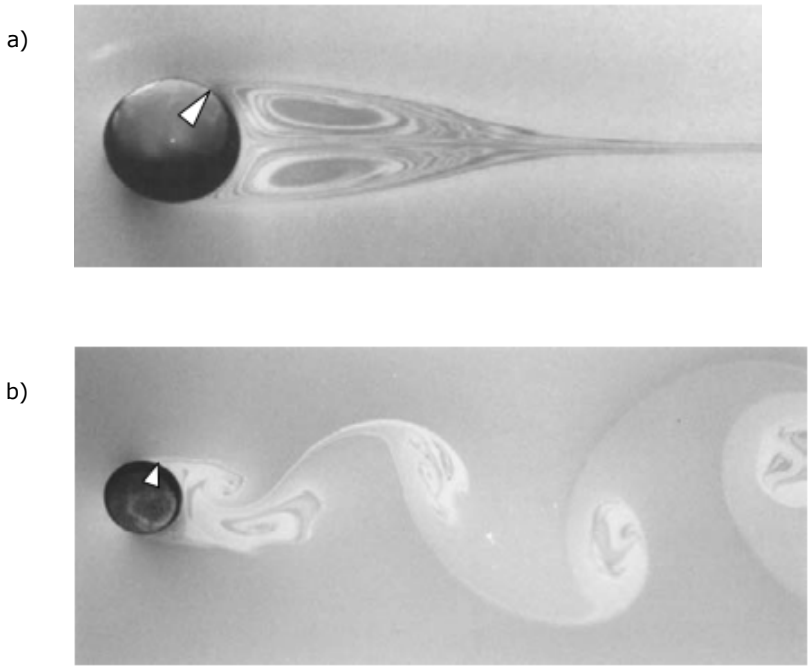

Figure 1.2: Visualisation of flow around a cylinder a) at Re = 35 and b) at Re = 100, white triangles mark separation points, taken from Wu et al. [31]

After separation, the boundary layer changes into a turbulent shear layer between the main flow and the wake of the body. This shear layer greatly influences the structure of the separated flow. Turbulent mixing between the shear layer and the underlying volume causes momentum transfer into the dead water region, driving vortices in the wake. For commonly analysed bluff bodies shear layers form either one-sided or two-sided. Two examples are shown in figure 1.3.

Figure 1.3: Formation of shear layers a) one-sided b) two-sided, taken from [18]

As a simplification one- and two-sided flow separation can be viewed as two dimensional processes.

An example for one-sided separation is the flow over a backward facing step. The shear-layer forming at the step drives the upper layer of the underlying volume, moving it in direction of the flow, thereby decreasing the pressure in the rest of the volume. The decreased pressure pulls the widening shear layer farther down and a dead water region with partial recirculation is formed. The length of the dead water region and the pressure in it are typically higher for one-sided separation than for two-sided separation.

Two-sided separation is characterized by strong interaction between the two shear layers, resulting in high vorticity a short dead water region and low pressure. The process is described in more detail by Tombazis and Bearman [29] also referring to Gerrard [13]. The momentum transport from the shear layers feeds vorticity to newly forming vortices at the back of the body. While a vortex is growing in size the position of it's centre relative to the body hardly changes. Once the vortex has become large enough it will start to draw in the opposite shear layer which transports vorticity of the opposite sign. This interrupts the growth of the vortex and causes it to shed from the body. Afterwards, the formation of a new vortex starts from the opposite shear layer. This process continues to periodically produce and shed vortices, which are then convected downstream and slowly move away from the horizontal centre line of the wake. They form a von Kármán vortex street.

The frequency with which vortices are shed from a bluff body is characteristic for a body and can be described by a dimensionless number, the Strouhal number. It is defined by the formula:

$$St = \frac{f_n h}{u_\infty} \tag{1.1}$$

Where h denotes the height of the body, f_n is the natural shedding frequency and u_∞ the free stream velocity. As mentioned by Pastoor et al. [24], the dominant Strouhal numbers of bluff bodies are usually within a range of 0.2 for cylinders and 0.26 for short D-shaped bodies. In their own experiments with a D-shaped bluff body in a Reynolds number range of $2.3 \cdot 10^6$ to $7.0 \cdot 10^6$, they have measured Strouhal numbers in the range of 0.23 to 0.25. The Reynolds numbers investigated in this work are within that range, too.

Furthermore it shall be mentioned that for bluff bodies, the body's height is often considered the relevant length scale for the calculation of the Reynolds number. The formula therefore reads:

$$Re = \frac{u_\infty h}{\nu} \tag{1.2}$$

1.3 Passive drag reduction

The earliest attempts to reduce the drag of bluff bodies have been made by trying to change the flow passively. This usually means changing the shape of the body, it's physical properties or adding devices like plates or flaps that are not moved actively. This approach is appealing as a drag reduction comes at no energetic cost. Furthermore passive drag reduction is usually technically uncomplicated to implement, using no moving pieces and should therefore be very reliable. On the other hand, passive solutions are often not very practical. In the real world many bluff bodies are bluff for other than aerodynamic reasons. Changing their shape can therefore come with other drawbacks and might simply not be an option. Truck trailers for example are usually shaped like cuboids to maximise their transport volume within the legal limits for their dimensions. Any change in their shape would reduce their volume.

This section focusses on 2D flow over bodies with two-sided separation as this is a commonly investigated type of bluff body flow and also the type of flow around the model used in the experiments described in the following chapters. As described in section 1.2 flow with two sided separation (see figure 1.3 b)) is dominated by strong interaction between the two opposing shear layers, causing strong energy dissipation, large vortex structures and low pressure at the base. As pressure drag is the dominant form of drag for bluff bodies, all drag reduction approaches aim at increasing the pressure at the base of the body. To achieve this goal, the structure of the separation region has to be altered. Table 1.1 gives an overview of different approaches that have been investigated so far.

Mechanism	**Method**	**Authors**
inhibition of shear layer interference	splitter plate	Roshko [25] Tanner [28] Leder [21]
increase of boundary layer thickness	increased surface roughness	Whitmore & Naughton [30]
wake shaping	deflector plates	Frey [10]

Table 1.1: Overview of passive drag reduction approaches

Drag reduction by attachment of a splitter plate to the base of the body has been investigated by Roshko [25], Tanner [28], Leder [21] and many others. Roshko and Leder describe the influence of the length of a splitter plate directly attached to the base of the body as well as the influence of the distance between the base of the body and a rather short splitter plate positioned behind it. A part of their results is shown in figure 1.4. The left graph is showing the Strouhal number S and the base pressure coefficient c_{ps} over the non-dimensional distance c/d between the end of cylinder with diameter d and the end of a splitter plate with length 1.14 d. One can see that up to a distance of about 3.8 the base pressure increases while the Strouhal number decreases. After 3.8 there is a sudden drop in the base pressure and a sudden increase in the Strouhal number. A similar behaviour can be seen in the right graph where the drag coefficient is plotted over the similarly defined length of a splitter plate attached to a vertical plate of height D or the distance between the back of the vertical plate and the end of a detached splitter plate of half that length. The drag coefficient for the unconnected splitter plate (white squares) reaches a minimum at a non-dimensional distance of about 4 and then sharply increases again to values similar to a minimum distance of 0.5. For the attached splitter plate (black crosses), the drag coefficient generally decreases with the length of the splitter plate with the exception of a small local maxima at about 4.0.

Splitter plates separate the upper and lower shear layers and flow separation areas and prevent their interaction. This changes the characteristics of vortex formation behind the body from a flow region with two sided formation of shear layers to two flow regions with one sided formation of shear layers. As mentioned before this type of flow is associated with a longer dead water region and higher base pressure. As one would expect, a longer splitter plate is more efficient at separating the two shear layers. The more interesting result is that a shorter splitter plate, placed in the right distance from the body, can yield a similar drag reduction. This indicates that at a distance of about 3 to 4 heights of the body there is a region in which the two shear layers interact the most. Roshko additionally observed an influence on the Strouhal number. As the splitter plate is pushed farther into the interaction region, the vortex formation frequency decreases. Tanner examined the effects of length and thickness of splitter plates. He found that higher length as well as higher thickness of the splitter plate can decrease the drag. A thicker plate effectively covers more of the body's base leaving less surface exposed to the reduced pressure in the dead water region. The base area of the splitter plate would instead be exposed to higher pressure farther downstream.

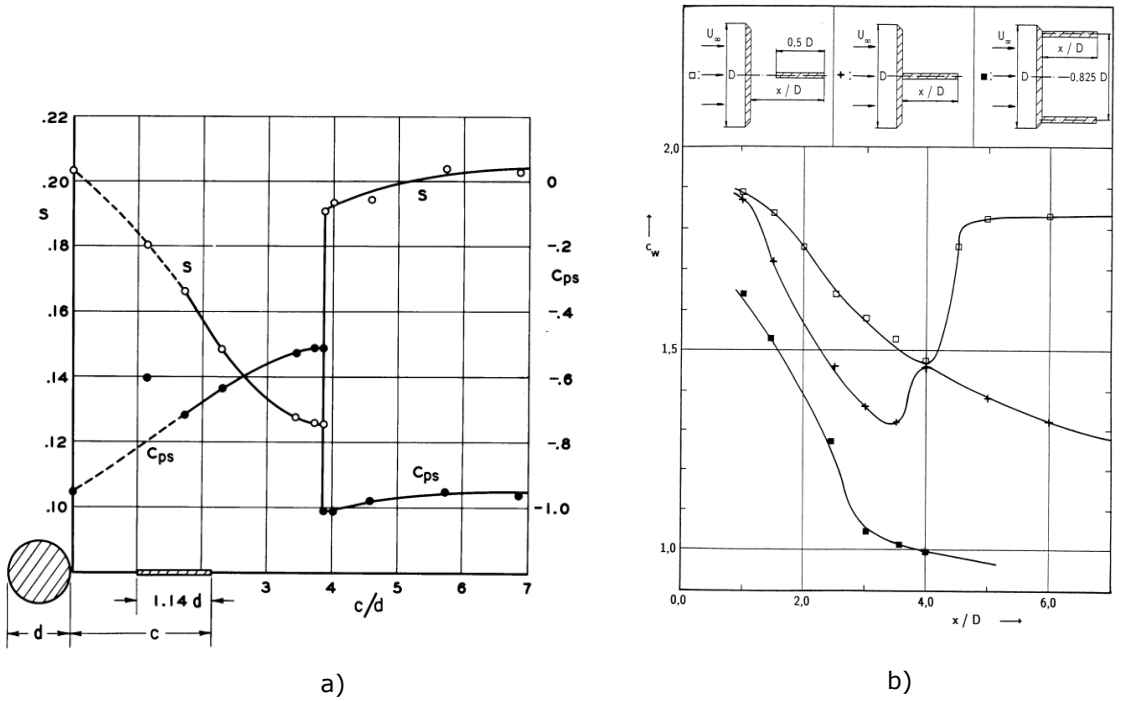

Figure 1.4: Impact of splitter plates on drag and Strouhal number, modified from Leder [21] and Roshko [25]

Whitmore and Naughton investigated drag reduction of a bluff body by an increase in it's surface roughness. The idea is based on the observation that there is a correlation between viscous drag on the forebody and pressure drag at the base. Pressure drag decreases with increasing viscous drag. For bluff bodies the pressure drag is usually much higher than the viscous drag and figure 1.5 shows that in the region of low viscous drag C_f and high pressure drag $C_{d_{base}}$, the slope between the two is particularly steep. This means that a small increase in viscous forebody drag can yield a significant decrease in base pressure drag. Following the curve one can conclude that there is an optimal working point where the total drag is minimized. The explanation for this correlation is that a higher viscous drag at the forebody leads to a thicker boundary layer downstream. This also means a wider shear layer at the separation point. This is said to cause less pressure reduction due to acceleration of flow in the dead water region and also a reduction of the strength of the vortices forming behind the body. Whitmore and Naughton tested this effect on a D-shaped bluff body model. They increased the surface roughness of the forebody by addition of exchangeable micromachined brass overlays. They managed to find a trade-off between viscous and pressure drag that reduces the total drag by 15 % compared to a smooth body.

Frey [10] investigated the effects of a staggered set of deflector plates at the trailing edges of buff bodies with a blunt base. The idea is to redirect the flow inwards to the base of the body and therefore effect a smoother flow over the the sharp edge and a higher pressure at the base. He tested this for different body shapes, varying e.g. the radius of the trailing edges. For the least aerodynamic shapes the measured drag reduction by addition of splitter plates was about 70 %. Leder points out that such a high drag reduction could not actually be achieved in concrete applications yet. The effect itself however is not questioned and can actually be compared to the redirection of flow through a Coanda yet, which will be further discussed in section 1.4.

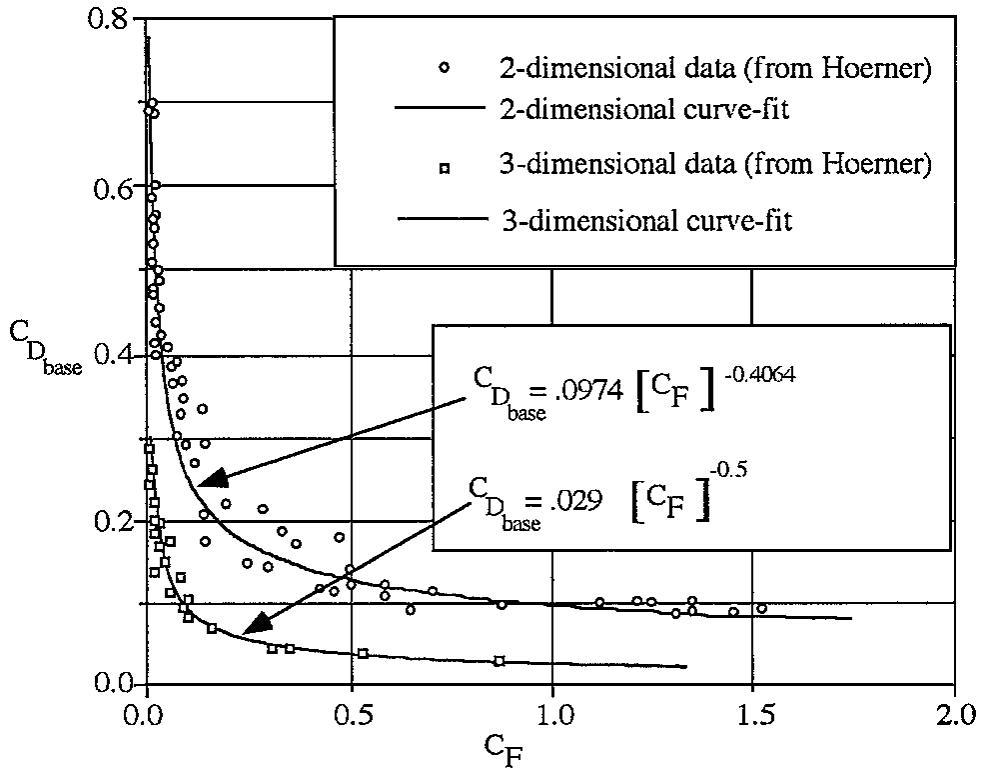

Figure 1.5: Correlation of viscous and pressure drag, taken from [30]

1.4 Active drag reduction

1.4.1 Open loop control

Active drag reduction approaches have one common disadvantage. That is, they all need energy to drive some form of actuation trying to change the flow. Additionally moving actuation mechanisms are more complex than passive devices and therefore often more expensive and less reliable. Advantages are that the flow can be influenced with less need for change in the geometry of the body and it's outer dimensions.

Bearman [1] investigated effects on the flow around a two-dimensional D-shaped body with elliptical leading edge and a blunt base by constant blowing through porous material covering almost the entire base of the body. The effects were examined at Reynolds numbers between $1.3 \cdot 10^4$ and $4.1 \cdot 10^4$ and different blowing intensities. Particular interest was given to the base pressure, vortex shedding frequencies and the distance of vortex formation. At sufficiently large blowing rates the formation of an alternating vortex street was suppressed entirely, leading to a higher base pressure and lower drag. Strong enough blowing through the base was found to separate the upper and lower shear layers comparable to the effect of a splitter plate. Furthermore the vortex formation distance was observed to correlated linearly with a decrease in base pressure. A maximum drag reduction of about 66 % was achieved. The energy invested in blowing was not considered. Furthermore the effect of blowing at fixed frequencies was not investigated.

Henning [15] investigated active drag reduction of a two-dimensional D-shaped bluff body model by open loop as well as closed loop turbulence control. The flow was influenced by two actuation slots at the trailing edges pointing outwards at an angle of 45 degree. The actuation was driven by speakers, causing a periodic change of blowing and suction from the slots at controllable frequencies and amplitudes. As the amount of air blown from the slot and sucked back in balance out, this type of actuation is called zero-net-mass-flux (ZNMF) actuation. For open

loop tests the effect of synchronous as well as 180 degree phase shifted actuation form both slots at different frequencies and blowing intensities were examined. The aim of synchronous actuation was to synchronize the development of both shear layers. Highest drag reduction was achieved while blowing with a frequency that corresponds to a Strouhal number of $St = 0.15$. The drag reduction was attributed to successful suppression of the formation of alternating vortices, as indicated by a smoke visualization shown in figure 1.6. Actuation at the natural vortex shedding frequency of $St = 0.23$ was found to increase the drag coefficient over the value of unactuated flow. Henning associated this to an amplification of the wake instability. This effect is even stronger when the actuation from both slots is driven with an 180 degree phase shift. Under optimal conditions a drag reduction of 15 % was achieved. An increase in the length of the recirculation region by 38 % was observed also.

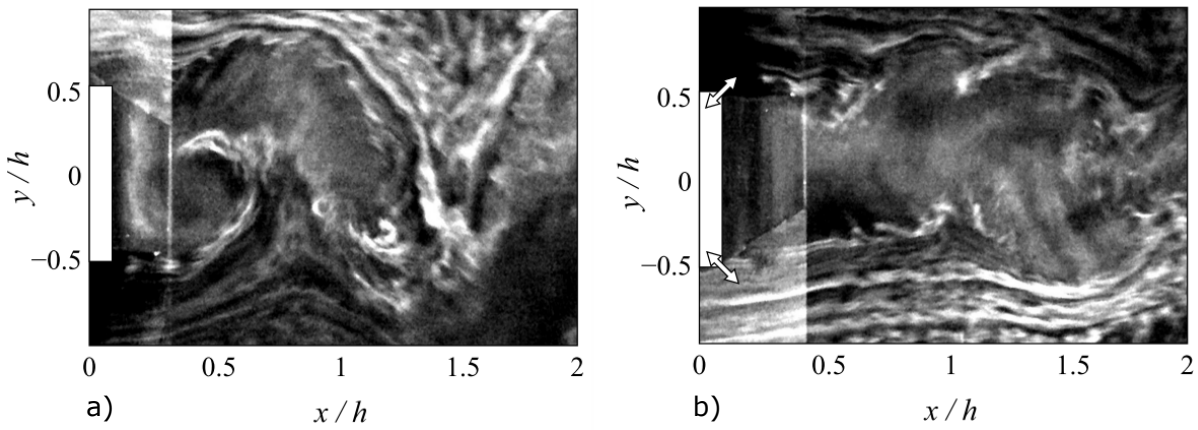

Figure 1.6: Smoke visualization of the flow in the wake of a D-shaped bluff body at $Re = 23000$, a) undisturbed natural flow, b) flow affected by optimal open loop actuation through ZNMF actuators (Henning [15])

Geropp and Odenthal [12] tested drag reduction of a bluff body by blowing two horizontal jets of air through slots at the trailing edges, over Coanda surfaces at the back of the body. The Coanda effect causes the jet streams to adhere to and follow the contour of curved surfaces. As the study was undertaken in an automotive context, they tested this on a two dimensional car shaped body. They argue that the typically two-dimensional behaviour of two shear layers interacting to form a recirculation region of two contra-rotating time averaged stationary vortices, also extends across the three dimensional rear of a car. As for many other approaches, the aim of this method is to increase the base pressure by influencing the formation of vortex structures in the dead water. As figure 1.7b shows, the recirculating region disappeared completely. The authors further describe that the outer flow was entrained by Coanda blowing, separation was prevented and the near wake was re-energized. A combination of blowing into the dead water tangentially and diversion of jets and outer flow by the Coanda effect lead to a reduction in dissipation, an increasing base pressure and therefore a drag reduction. During the experiments the blowing velocity was kept constant and different free stream velocities and therefore Reynolds numbers were tested. This resulted in different blowing rates ζ (ζ_R in figure 1.7):

$$\zeta = \frac{u_j}{u_\infty} \tag{1.3}$$

At high blowing rates all beneficial effects were overshadowed by the amount of momentum the jets add to the flow even leading to a measurement of negative drag. Optimal blowing rates to observe the positive aerodynamic effects of Coanda blowing were determined to be in the range of 1.5 to 2.5. At a blowing rate of 2.0 the authors measured an increase in base pressure of up to 50 % which, when considering all aerodynamic forces results in a drag reduction of 10 %.

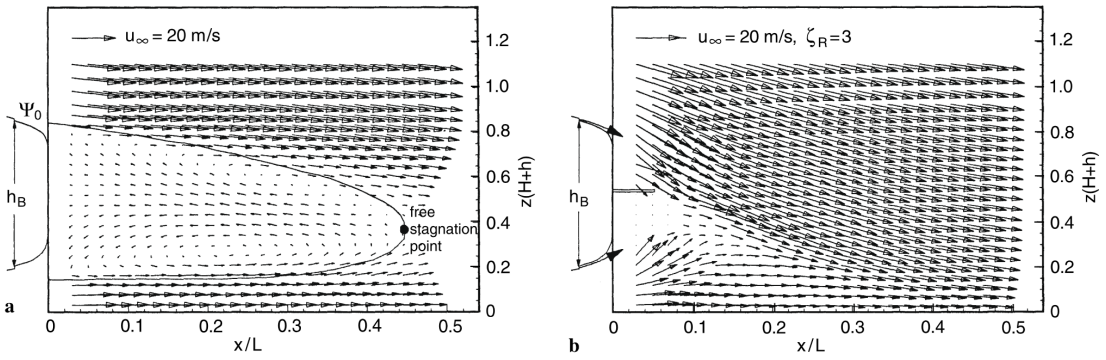

Figure 1.7: Laser Doppler Anemometry measurements of flow behind the model at $Re = 6.6 \cdot 10^5$ a) without blowing b) blowing rate of 3, taken from [12]

1.4.2 Closed loop control

While the actuation of open loop control is only dependent on time, closed loop control takes sensor signals into account. The actuation is made dependent on the measurement of parameters representing the state of the system that is to be controlled. This offers further degrees of freedom to improve the control efficiency. A further advantage is that the actuation can automatically adapt to different flow conditions. Difficulties with closed loop control are the correct determination of the state of the flow and the determination of a control law that correctly maps the sensor signals to an actuation command.

Pastoor et al. [24] examined different closed loop turbulence control strategies for drag reduction of the flow around a D-shaped body. Like Henning [15] they used a model with two ZNMF-actuation slots at the trailing edges. They have implemented and tested two different closed loop control strategies, an adaptive controller that finds optimal actuation parameters by slope seeking and a physically motivated phase controller.

Adaptive slope seeking control was used to automatically adapt the actuation amplitude to the current state of the flow to achieve the most efficient drag reduction. The actuation frequency was fixed to that corresponding a Strouhal number of $St = 0.15$ which has been found in previous open loop experiments to work best to synchronize the shear layers. The goal of the control is to find a maximum base pressure and therefore drag reduction at the least actuation amplitude. The optimal working point can be found without the need of a dynamical model of the plant. The local is slope is determined by sinusoidal modifications of the actuation amplitude. This control method was tested for Reynolds numbers from 40500 up to 70000. It was found that the optimal actuation amplitude decreases with increasing Reynolds number, while the base pressure can be maintained. Drag reductions of 15 % were measured.

Phase control is motivated by the idea that symmetrical formation of both shear layers can be enforced by actuation from just one slot at a fixed phase difference to the pressure oscillations caused by periodic vortex shedding on the opposite side of the model's base. A sketch of the model and the control concept is shown in figure 1.8. With the control switched on, an average actuation frequency corresponding to $St \approx 0.15$ resulted, which is similar to the optimal actuation frequency found by open loop control but did not have to be given manually. Investigation of the coherent flow structures showed resemblance to those of open loop actuation also. The controller was tested for Reynolds numbers from 23000 to 70000. An average drag reduction of 15 % was achieved at up to 48 % less actuation energy than needed for slope seeking control. The reduction in actuation energy stems primarily form the use of only one instead of two actuation slots. As the slots only covered half the span of the model, the authors expect a drag reduction of up to

30 % if slot covering the whole span are used.

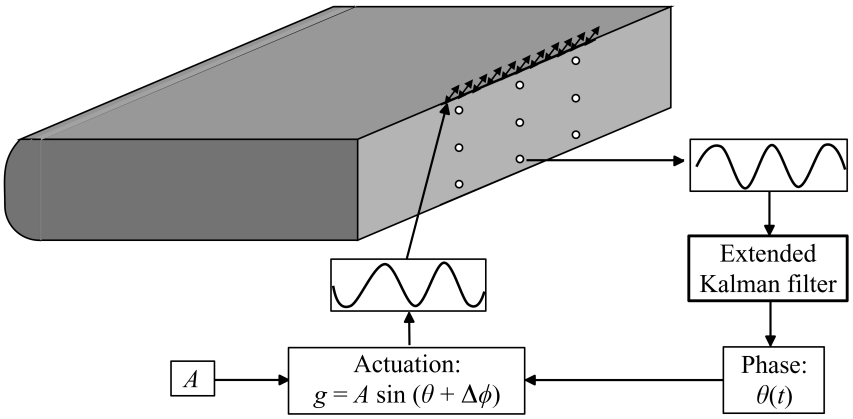

Figure 1.8: Sketch of the D-shaped body model and concept to implement phase control by estimation of the vortex formation phase from pressure oscillations at the lower side and phase shifted actuation from the upper side, (Pastoor [24])

Longa et al. [6] numerically investigated drag reduction of a D-shaped bluff body by linear feedback control. The control strategy was motivated by the observation that the time averaged base pressure and therefore also drag are correlated to wake flow fluctuations. The target of the controller is to achieve mean drag reduction by manipulation of these fluctuations. It was chosen to sense the wake fluctuations by the time varying values of the base pressure as this would also be easily accessible in an experimental implementation of the control. Spatially integrating the pressure on the upper and lower side with opposing signs yielded a particularly strong fluctuation signal. ZNMF-actuation was implemented by slots on the upper and lower side of the model and pointing 45 degree outwards. The controller was tested in two-dimensional Large-eddy simulations at a Reynolds number of 10000. The controller was found to achieve it's primary goal of attenuating the fluctuations in the wake. Consequently, a delay of the roll-up of shear layer vortices was observed, pushing the vortices further downstream and extending the recirculation region in x-direction. The time-averaged base pressure on the body by was increased by 38 %.

Gautier et al. [11] investigated closed loop separation control over a backward facing step by machine learning control (MLC) based on genetic programming. The study is of interest as both separation control and drag reduction by turbulence control can be reduced to the fundamental problem of controlling separated flows and shear layers. As machine learning control is also used in the current study it is explained in more detail in section 2.2. Actuation was implemented by slotted jets about two step heights upstream of the step. The step model and actuators are shown in figure 1.9. The slots open with a 45 degree angle from the wall surface into the stream. The actuation is capable of blowing and suction. The target of closed loop control was a reduction of the recirculation area measured by online particle image velocimetry (PIV) at the lowest possible actuation energy. For strong penalization of actuation it was given more weight than the recirculation area for the determination of the quality of a control law. The recirculation area used as only input to the control laws. The evolutionary process of machine learning control was found to have converged after the 9th generation. The best control law was showing non-proportional and non-monotonic dependence on the input signal and achieved a reduction of the recirculation zone of 80 %. The performance was found to be close to that of well tuned open loop forcing, however both approaches resulted in different control mechanisms. While open loop control used forcing at the natural vortex shedding frequency of about 1 Hz to excite Kelvin-Helmholtz vortices, the closed loop control law used resonance with the low frequency flapping mode instability at about 0.1 Hz. Variation of the Reynolds number also

showed that the performance of closed loop control was more stable.

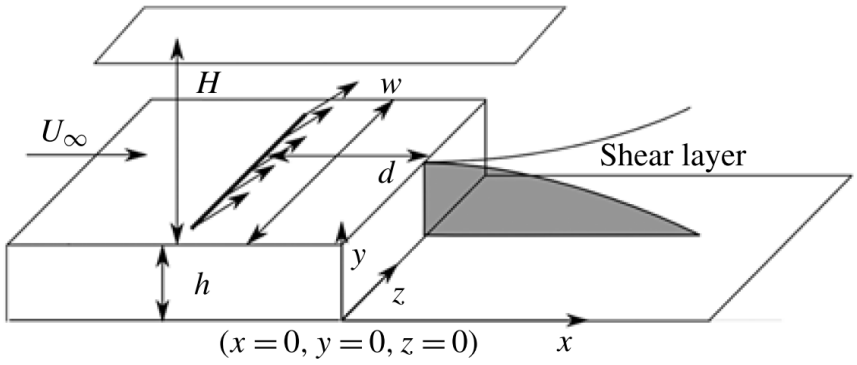

Figure 1.9: Sketch of the the backward facing step model geometry, actuators placed at distance $d/h = 2$ (Gautier et al. [11])

Chapter 2

Theoretical approach

2.1 Drag measurement

For comparability between differently shaped or sized bodies, the drag force acting on a body is normalized by the size of the body and the flow condition in terms of the free stream velocity.

$$C_D = \frac{D}{\frac{\rho}{2} \cdot U_\infty^2 \cdot w \cdot h} \tag{2.1}$$

The drag force D can be the sum of different forces acting on the body. For single, non-lifting bodies at subsonic speeds relevant forces originate from the friction between the bodies surface and the moving fluid and from an uneven pressure distribution over the body. These components are called friction drag and pressure drag. As mentioned before, pressure drag is the dominating form of drag for bluff bodies.

The drag force acting on a body can be measured in different ways. It can be measured directly e.g. by a balance or inferred by measurement of other properties. For the experiments presented in this work the drag is inferred by measurement of the pressure distribution in the wake of the model. The idea behind this is that the drag forces acting between the fluid and the body cause the fluid to lose momentum, which can be seen as a deficit in the velocity distribution behind the body. The velocity distribution can also be expressed in terms of the distributions of the static and total pressure. As the flow in the following experiments can be seen as two dimensional and the model is mounted horizontally, only vertical distributions are of interest. Figure 2.1 qualitatively shows velocity distributions before, closely behind and far behind a static body. Before the flow passes the body, velocity u_∞, total pressure $p_{0,\infty}$ and static pressure p_∞ are distributed uniformly. Shortly after passing the body, denoted by ②, one can see a deficit in the velocity distribution in the wake of the body. Total and static pressure are no longer distributed evenly either. Far behind the body, denoted by ①, velocity and total pressure show a lower but wider deficit while the static pressure has returned to a uniformly distributed p_∞.

A control volume for the definition of a momentum balance is best set up around the points A,B,C and D in figure 2.1. This way, a momentum balance set up for the x-direction is unaffected by volume forces as well as surface forces between the free surfaces. As the static pressure acting on the surfaces AD and BC is p_∞ on both sides, there is no resulting force on the fluid volume. The only force left to consider is the force acting on the contact surface between the control volume and the body. This force is equal to the drag force D and to the change in momentum between AD and BC. The flow of momentum entering the volume through AD and leaving it through CB

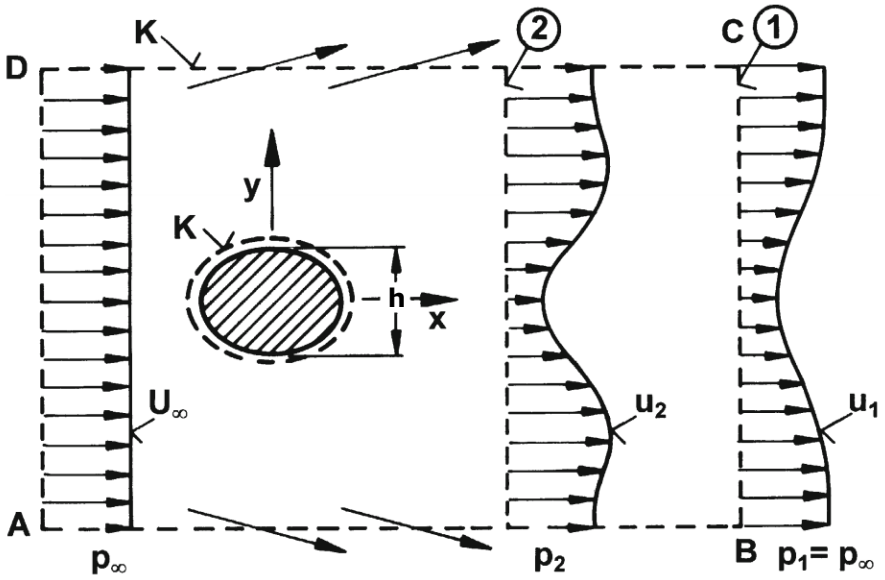

Figure 2.1: Spacial propagation of the velocity distribution, modified from [18]

is:

$$I_{in} = -\rho \cdot w \int u_\infty^2 dy \tag{2.2}$$

$$I_{out} = \rho \cdot w \int u_1^2(y) dy + \rho \cdot w \int u_\infty \left[u_\infty - u_1(y)\right] dy \tag{2.3}$$

The balanced of momentum entering and leaving the control volume is:

$$I_{in} + I_{out} = -\rho \cdot w \int u_1(y) \left[u_\infty - u_1(y)\right] dy = W \tag{2.4}$$

This can be restructured to show that the drag coefficient C_D is:

$$C_D = \frac{W}{\frac{\rho}{2} \cdot u_\infty^2 \cdot w \cdot l} = 2 \int \frac{u_1(y)}{u_\infty} \left[1 - \frac{u_1(y)}{u_\infty}\right] d\left(\frac{y}{h}\right) \tag{2.5}$$

Using the Bernoulli-equation this can be formulated as:

$$C_D = 2 \int \sqrt{\frac{q_1(y)}{q_\infty}} \left[1 - \sqrt{\frac{q_1(y)}{q_\infty}}\right] d\left(\frac{y}{h}\right) \tag{2.6}$$

This yields an expression for the drag coefficient depending only on the distribution of the dynamic pressure $q_1(y)$ along BC, far behind the body. However it is not possible in this and most other experiments to measure the pressure distribution far enough behind the body for the assumption of a uniform distribution of $p_1(y) = p_\infty$ to be valid. At a position behind the body where the pressure can actually be measured, the conditions of section ② hold. The method of Jones, as described in [17], can be used to express the theoretically necessary pressure distribution in section ① through actually measurable pressure distributions from section ② by using the equation of continuity and Bernoulli's equation. The corrected formula reads:

$$C_D = 2 \int \sqrt{\frac{p_{0,2}(y) - p_2(y)}{q_\infty}} \left[1 - \sqrt{\frac{p_{0,2}(y) - p_\infty}{q_\infty}}\right] d\left(\frac{y}{h}\right) \tag{2.7}$$

The spatial distributions of the total pressure $p_{0,2}(y)$ and the static pressure $p_2(y)$ can be measured by a pressure rake equipped with Pitot and Prandtl probes. To get an accurate measure of the drag, the measurement has to cover the whole width of the wake. For a rake smaller than the wake, this can be achieved by vertically traversing the rake. The region outside the wake does not contribute to the drag as the integrand in equation (2.7) has non-zero values only inside the wake. It is furthermore necessary to position the rake far enough downstream of the model, to ensure that the angle between the flow and the probes is small. As the free-stream static pressure p_∞ and dynamic pressure q_∞ are not measured directly they shall be expressed by values measurable by a rake also. Hofmacher [16] suggests expressing the free-stream static pressure p_∞ as the difference between the total pressure measured outside the wake $p_{0,outside}$ and the free-stream dynamic pressure q_∞:

$$p_\infty = p_{0,outside} - q_\infty \tag{2.8}$$

This replacement ensures that the integrand in equation (2.7) becomes zero outside the wake. Moreover, as mentioned by Houghton [17] q_∞ can in good approximation be expressed as the difference between total and static pressures measured outside the wake.

$$q_\infty = p_{0,outside} - p_{outside} \tag{2.9}$$

These two replacements can be summed up to the approximation that the total and static pressure in section ② outside the wake reach levels close to the free-stream conditions. Errors introduced by this approximation are tolerated as the main focus of this work is not to measure C_D at the highest possible accuracy but to quantify drag reduction by different methods. It is reasonable to assume that the error is small compared to the measured drag coefficients as this method has been used successfully for airfoils before. Equation (2.7) can therefore be written as:

$$C_D = 2 \int \sqrt{\frac{p_{0,2}(y) - p_2(y)}{p_{0,outside} - p_{outside}}} \left[1 - \sqrt{\frac{p_{0,2}(y) - p_{outside}}{p_{0,outside} - p_{outside}}} \right] d\left(\frac{y}{h}\right) \tag{2.10}$$

The drag coefficient can now be calculated based on pressure values measured only by a rake. Figure 2.2 shows an exemplary distribution of total and static pressure over the vertical coordinate y and visualizes the different pressures necessary for drag determination.

A measurement by a pressure rake gives a set of discrete values along the two pressure distributions. In order to get full, continuous pressure distributions a function is fitted to each set of discrete data points. The following function has proven suitable to fit the data in previous tests by Shao [26]:

$$\frac{p(y) - p_\infty}{p_{min} - p_\infty} = (1 + ay^2)^{by^2} \tag{2.11}$$

In this equation p_{min} is lowest pressure value in the middle of the wake. The values for p_∞ and p_{min} have to be found separately. The variables a and b are model parameters. Optimal values have to be found by a fitting procedure. To improve the degree of automation in the fitting procedure, the model described by equation (2.11) has been adapted by replacing the variables p_∞ and p_{min} by model parameters c and d therefore giving the fitting procedure the freedom to vertically translate and scale the model curve to best fit the data. A fifth model parameter e is introduced as a variable offset for the y-coordinates, allowing the fitting procedure to also translate the fitted curve horizontally. Moving all model parameters to the right hand side, the model function becomes:

$$p(y) = [1 + a(y - e)^2]^{b(y-e)^2} \cdot (d - c) + c \tag{2.12}$$

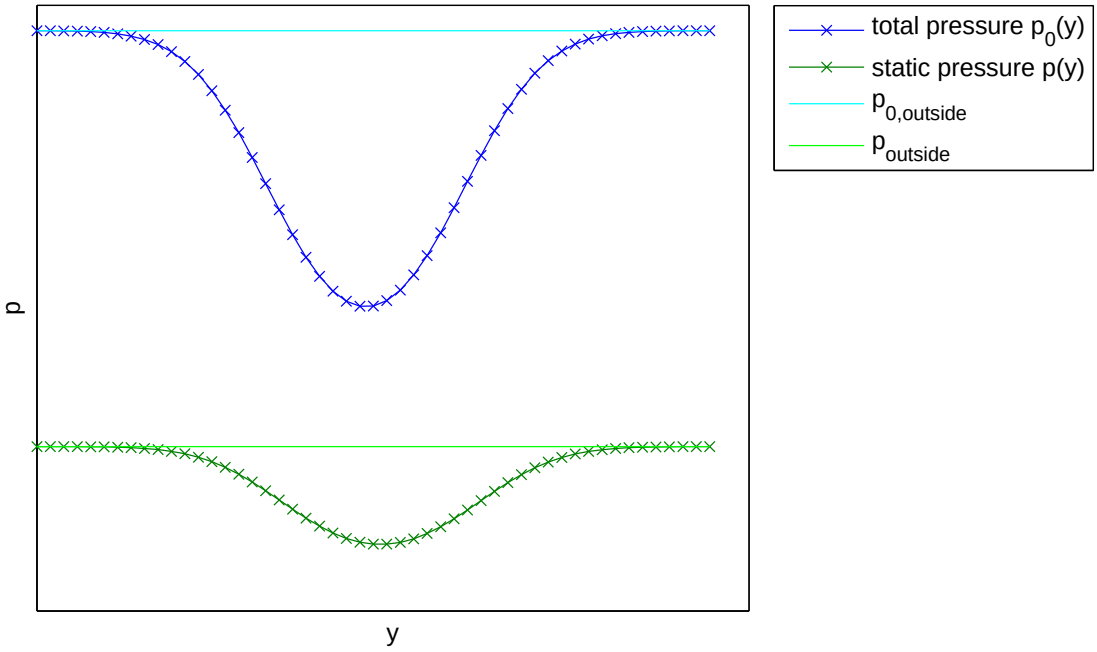

Figure 2.2: Exemplary distribution of the total and static pressures as measured by a rake in the wake of a bluff body

MatLab's inbuilt nonlinear regression function "nlinfit" is then used to find model parameters a to e that result in an optimal fit of the model function to a given set of data points by minimizing the mean squared differences between the measured data and the corresponding results of the model function. This method has shown to be suited to find a continuous function that matches a given set of discrete pressure values very well as long as the number of data points is high enough. The minimum number of data points available for the fitting is limited by the number of Pitot and Prandtl probes on the rake and how many rake positions can be used. For the following experiments drag coefficients will have to be determined from a minimum of one rake position with a rake containing 22 Pitot and 5 Prandtl probes. Equation (2.12) has shown good results when fitted to a distribution of 22 total pressure data points. It is however not suited to be fitted to a distribution of 5 static pressure data points as the number of data points equals the number of model parameters. To overcome this problem, the assumption is made that the wake leaves a similarly shaped deficit in the total as well as static pressure distributions. In equation (2.12) the shape of the curve is affected only by the parameters a and b while c,d and e only cause translation and scaling of that shape. After having determined the shape from fitting a model to the total pressure distribution, this shape can then be used in the fitting process of the static pressure data. This means that equation (2.12) can still be used to fit the more sparse static pressure data but the number of parameters to be determined by nonlinear regression is reduced by fixing a and b to the values determined for the total pressure data. Consequently only the three parameters c,d and e have to be optimized. Figure 2.3 shows an exemplary fit achieved with this method. Averaged over each distribution, the residuals are below 3 % of the measured values for the total pressure and below 1 % for the static pressure. This is lower than the error of the pressure measurement system used to obtain the data.

The resulting model functions describe the total and static pressure distributions $p_{0,2}(y)$ and $p_2(y)$ in the range of the measured data as continuous functions. These functions can be used in equation (2.10). Furthermore, the parameter c obtained for the total pressure can be used as $p_{0,outside}$ and the same parameter obtained for the static pressure can be used as $p_{outside}$. The integration is done by the MatLab function "integral" using global adaptive quadrature. This

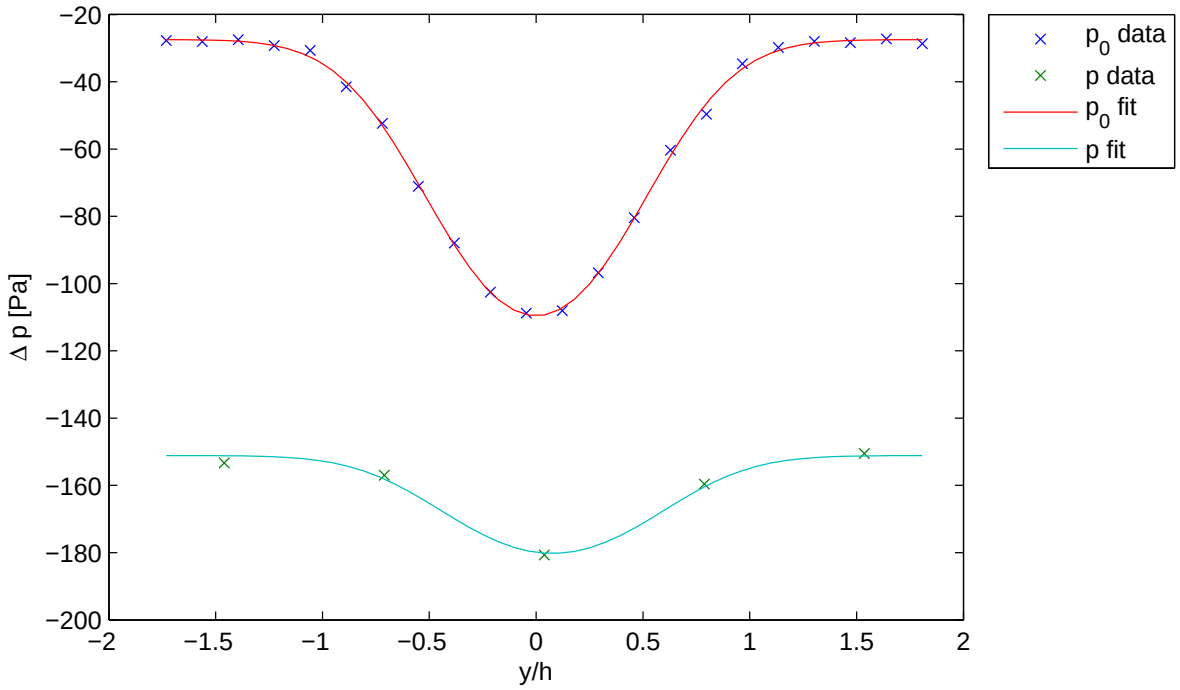

Figure 2.3: Distribution of total and static pressure in the wake of a D-shaped bluff body, fitted by a nonlinear model described by equation 2.12

way, the drag can be calculated automatically and reliably from a pressure measurement covering the wake. The automation is necessary primarily for the closed loop control experiments. The whole MatLab code can be found in appendix A.1.

2.2 Machine learning control

2.2.1 Fundamentals

Machine learning is an increasingly popular field with the aim of finding a model of a system by analysing large amounts of data. Different machine learning strategies have been used successfully in a manifold of different fields. The aim of machine learning control (MLC) is to use these methods to find an optimal control law $b = K(s)$, mapping sensor signals s to an actuation signal b to control a complex system while minimizing a cost function J. The hope is that a machine learning strategy can find control mechanisms that have not been found before due to the complexity of the system. The control problem of interest for the later described experiments is closed loop turbulence control.

An overview of different classes of control strategies based on how much they use mathematical knowledge of the system or data is shown in figure 2.4. Machine learning control is a model free control strategy. No mathematical knowledge about the system is used in the design of a control law. MLC finds an optimal control law in an unsupervised way, entirely based on data gathered from the system.

The machine learning technique that is of interest for the following closed loop turbulence control experiments is genetic programming. Genetic programming is a special type of the larger group of evolutionary algorithms. They mimic evolution like it is happening in nature through natural selection. This is achieved by repeatedly having a group of possible solutions for a given

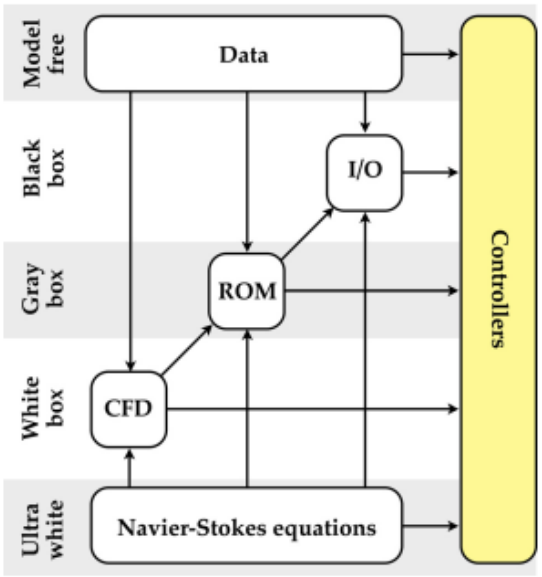

Figure 2.4: Control model hierarchy, taken from [3]

problem compete against each other in solving that problem. Characteristics of particularly well performing solutions are preserved and modified throughout the process by a set of rules.

A group of possible solutions is usually referred to as one generation, while a single solution is called an individual. The number of individuals per generation is called the population size. For a closed loop control problem, a solution is a control law of the aforementioned form $b = K(s)$. An algorithm implementing genetic programming starts with creating a random initial generation of a defined population size. Each individual of this generation is then tested for how good it performs in controlling the system. The performance has to be quantified by a cost function $J(b, s)$ that is usually defined to be smaller for better performing individuals. Once the performance of each control law is known, a second generation can be generated from the first through a set of genetic operations. These operations are replication, crossover and mutation. Defined probabilities P_r, P_c and P_m set the chances of each of these operations being used. To be able to apply the operations to the individuals, the individuals have to be defined as a set of genes that can be exchanged or modified. A selection process is used to choose which individuals from the first generation are used to create the second generation. The evolutionary process is repeated until a break criterion, like a target fitness or a maximum number of generations, has been met. This process is also described in pseudo-code in algorithm 2.1.

```
1  generation_0 = random_individuals(population_size)
2  i = 0
3
4  repeat
5   i++
6    for each individual j in generation_i do
7     cost_{i,j} = determine_cost(individual_{i,j})
8
9    for population_size times do
10    selection = select_individuals(generation_i))
11    individual_{i+1,j} = genetic_operations(selection)
12
13 until break criteria is met
```

Algorithm 2.1: Genetic programming algorithm pseudo code

As mentioned before, an individual has to be described by a set of genes. This is implemented by using a tree based expression for the control laws. This representation of individuals allows to optimize both the structure and parameters of a control law, which is essential for genetic programming. The result of an expression tree can be obtained at it's root form which a set of branching points and/or leafs emerge. Branching points represent mathematical operations as addition, subtraction, multiplication and division. They can however represent other mathematical functions also. From each branching point, new branches in the number of necessary operands to perform the operation emerge. The number of operands is also called the arity of the operator. Leafs end a branch and can represent either constants or variable inputs e.g. in the form of a sensor reading. The aforementioned genetic operations of replication, crossover and mutation can be performed easily on expression trees, as shown in figure 2.5. To perform a replication, an entire tree is simply copied. For a crossover operation, first one branch of each tree is chosen, then the two branches are swapped. The mutation operation chooses a branch from a single tree and replaces it by a randomly generated new branch.

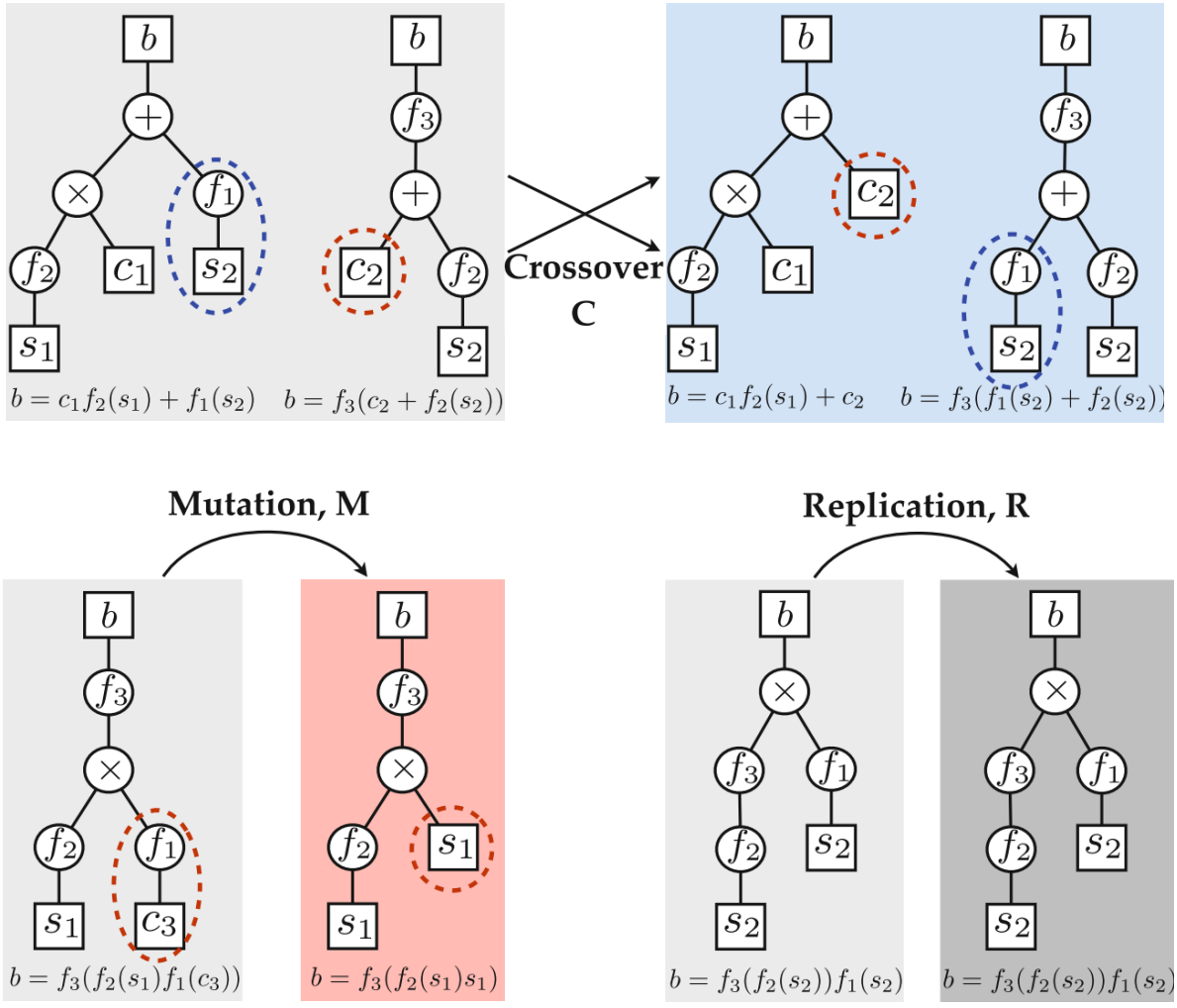

Figure 2.5: Genetic operations, each tree represents a control law in the form $b = K(\vec{s})$, f_i are arbitrary mathematical functions, modified from [9]

To select which individuals from one generation the genetic operations shall be performed on, a tournament selection process is used. First, a number N_p of individuals, defined as tournament size, is chosen randomly from the whole current generation. The individuals inside the tournament are then ranked by their cost function value and the best individual is chosen as winner of the tournament. There exist several different variations of this selection mechanism that all base

on the same principle. The choice of the exact method used for the experiments is mentioned in section 3.5.

One shortcoming of the basic algorithm described so far is that it can not guarantee that the evolutionary process will converge towards an optimum. The best individual from one generation could be lost in the process of generating a new generation in case it is simply not picked to compete in a tournament, is mutated or crossed with a bad individual. This would mean that minima in the search space could be found an lost again. To ensure that the evolutionary process converges towards an optimum, elitism has to be added to the progression from one generation to the next. Elitism guarantees that a set number N_e of best individuals is always copied to the next generation without undergoing a selection process.

One can already see that the behaviour and performance of genetic programming depends on the choice of several configuration parameters. The most important ones are summarized again in table 2.1. Each of these parameters can be found to affect the course of evolution by either promoting the exploration of new minima in the search space or the exploitation of already found minima. For each parameter promoting one often means demoting the other. The choice of values therefore means finding a suitable trade off.

Parameter	**Meaning**	**Increase promotes**
N_i	population size	exploration
P_m	mutation probability	exploration
P_r	replication probability	exploitation
P_c	crossover probability	exploitation
N_p	tournament size	exploitation
N_e	number of elite individuals	exploitation

Table 2.1: Most important MLC parameters and their impact on the progression through the search space

A larger population size N_i promotes exploration of the search space. As the initial generation is generated randomly, the resulting individuals should be scattered randomly throughout the search space also. A higher population size therefore means that the search space is initially explored more densely. This increases the chance of finding local minima. Increasing the population size does not demote exploitation directly but increases the number of individuals that have to be tested per generation. This means that it takes longer to evaluate the costs for one generation or that less generations can be evaluated in the same time, slowing down convergence.

The replication probability P_r determines the percentage of individuals in a new generation that are copied from an old generation. Replication serves as memory of good individuals or local minima in the search space. It is therefore helping in keeping individuals close to already found minima, enabling and promoting their exploitation.

The crossover probability P_c determines the percentage of individuals in a new generation that are generated by breeding of selected individuals from an old generation. Each individual has the same chance to be picked to enter a tournament. Good individuals however have a higher chance to win a tournament and be picked for breeding. If two good individuals are sitting close to the same minimum in the search space, there is a good chance that they are having similar genes. A crossover between them should therefore create a new individual that is close in the search space also, potentially exploiting a previously found minima even further.

The mutation probability P_m determines the percentage of individuals in a new generation that are generated by mutation of selected individuals from an old generation. As mutation randomly changes genes of an individual, it promotes that genetic programming keeps exploring random new locations in the search space, trying to find new minima.

Additionally the sum of the replication, crossover and mutation probabilities always has to be one. This means that increasing one of them always means reducing one or both of the others, further emphasizing the trade-off in the choice of values.

The tournament size N_p determines how many individuals of one generation are randomly picked to compete in a tournament. The set of all individuals that are added to a new generation through genetic operations consists only of individuals that have successfully passed the selection process. A higher tournament size means that there is a higher chance for the same good individuals to enter every tournament. Consequently the chance for a worse individuals to win a tournament is decreased. The genetic diversity in a new generation is decreased then as all offsprings originate from a smaller set of parents. For the search space this means that the distribution of individuals is focused more around already found minima, promoting their exploitation but demoting exploration of the rest of the search space.

The number of elite individuals N_e determines the number of individuals in a new generation that are copied from an old generation without having to compete in a selection process. Like replication, this is helping to keep individuals close to already found minima, enabling and promoting their exploitation.

Another important aspect of machine learning control is the choice of a cost function J to determine how well an individual is performing in the given task. For turbulence control in the wake of a D-shaped body, an obvious cost function would be the aerodynamic drag that is to be minimized. However, all active turbulence control strategies consume energy for an actuation mechanism. This energy is should be minimized also. Both of these objectives should be considered in the cost function. This can be achieved in two ways. The first way is to reduce this multi-objective problem to a single-objective problem. Therefore the costs of both objectives are combined into a single value, e.g. by a linear combination:

$$J = J_1 + \gamma \cdot J_2 \tag{2.13}$$

with $J_{1,2}$ being the individual cost functions of each objective and γ being a weighting factor. If both individual cost functions return a physically meaningful property, a sensible weighting factor can be given by that already. Otherwise a value has to be chosen in a different way, e.g. by comparison of known best and worst cases.

Alternatively the two individual cost functions can be handled as a true multi-objective problem. This means that both objectives are treated independently and an individual is attributed two cost values. Naturally a direct comparison between two individuals is not always possible this way and determination of a best individual is harder also. As stated by Luke [22], the predominant way multiple objectives are handled is by treating them in a Pareto-sense. Individual one is said to Pareto dominate individual two if it is better in at least one objective and at least equally good in all other objectives. For two objectives, the relation between all individuals can be visualized in conveniently in a Pareto plot, as shown in figure 2.6. Each axis represents the value of one cost function. Each individuals is represented by a point with coordinates equal to it's cost values. Individuals that are not dominated by others are called nondominated. In the plot, they form the Pareto nondominated front or just Pareto front. For each of these individuals, one can not find any other individual that is better in one objective without being worse in another. For multi-objective optimization each individual on the Pareto front is considered to be optimal. The target of optimization is to push the entire front towards more efficient solutions. It can also be shown that each point on the front represents an optimal single objective solution for a specific γ in equation (2.13). All individuals with the same cost value calculated by equation (2.13) for a given weight, lie on a straight line in the Pareto plot. Any individual on one side of the line has a higher cost, while any individual on the other side has a lower cost. If this line is made to intersect tangentially with the Pareto front, all but one individual should be on the side of the line that represents a higher cost. The individual on the line is the optimal single-objective solution

for that line/weight. Multi-objective optimization can therefore be seen as a generalisation of single-objective optimization.

While Pareto nondomination allows to identify a set of optimal solutions and multi-objective optimization tries to improve all of them, a tournament selection method still has to choose a single individual for each genetic operation throughout the evolution. Again, there exist many different approaches to this problem. The implementation of genetic programming used for the following experiments uses the NSGA-II algorithm, as proposed by Deb et al [7]. Two parameters are considered in the NSGA-II selection process. The first parameter is the nondomination rank. Individuals on the original pareto front are attributed a nondomination rank of one. After removing this front from the the set of individuals, a new front can be identified. All individuals on this new front are attributed a nondomination rank of two. This process is continued until a rank is found for each individual. The nondomination rank is the primary factor considered for the selection. An individual with a lower rank is always chosen over one with a higher rank. If two individuals are of the same rank, their crowding-distances are compared. An individual's crowding distance is calculated as the sum of the distances in each objective between the individual and it's closest neighbour in the Pareto plot. The individual with the higher distance is chosen as the space around it is less densely explored.

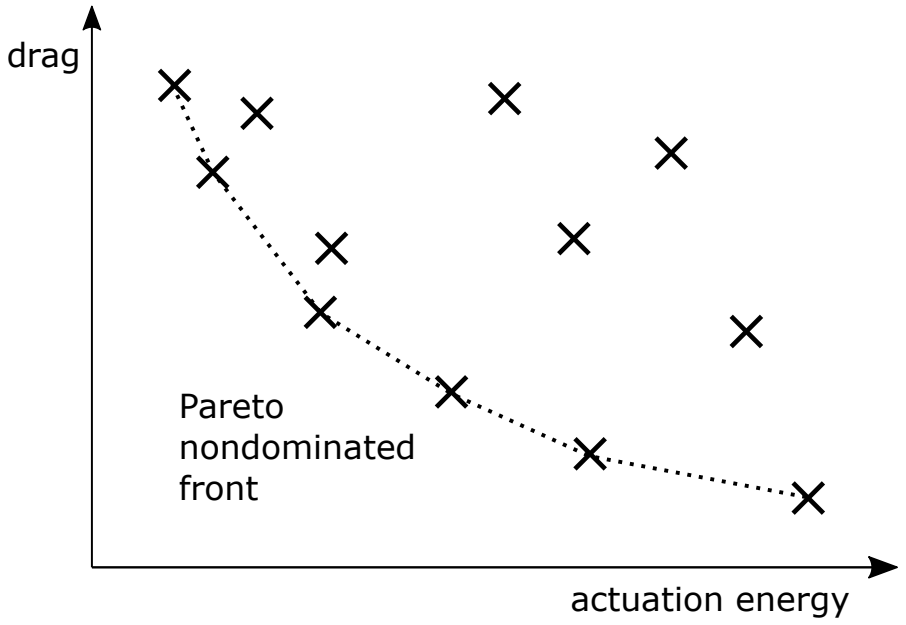

Figure 2.6: Pareto plot showing the pareto nondominated front for the objectives drag and actuation energy, note that both objectives are defined to be better at smaller values

In the following experiments MLC is used to find an optimal control law for closed loop turbulence control in the wake of a D-shaped bluff body. The cost for an individual has to be determined through an experiment during which the control law is applied. The conceptual design of an MLC run is shown in figure 2.7. The bluff body model in the wind tunnel takes the place of the dynamical system that is described mathematically in the figure. In an inner, fast loop, sensor signals are read from the model and a controller computes the corresponding actuation signal that is sent back to the model's actuators. While the inner loop is running, the cost is calculated and returned to the outer loop i.e. the genetic programming trying to optimize the control law.

When using an experiment instead of a mathematical model as dynamical system, additional aspects have to be considered. First of all, measurable quantities have to be chosen that indicate

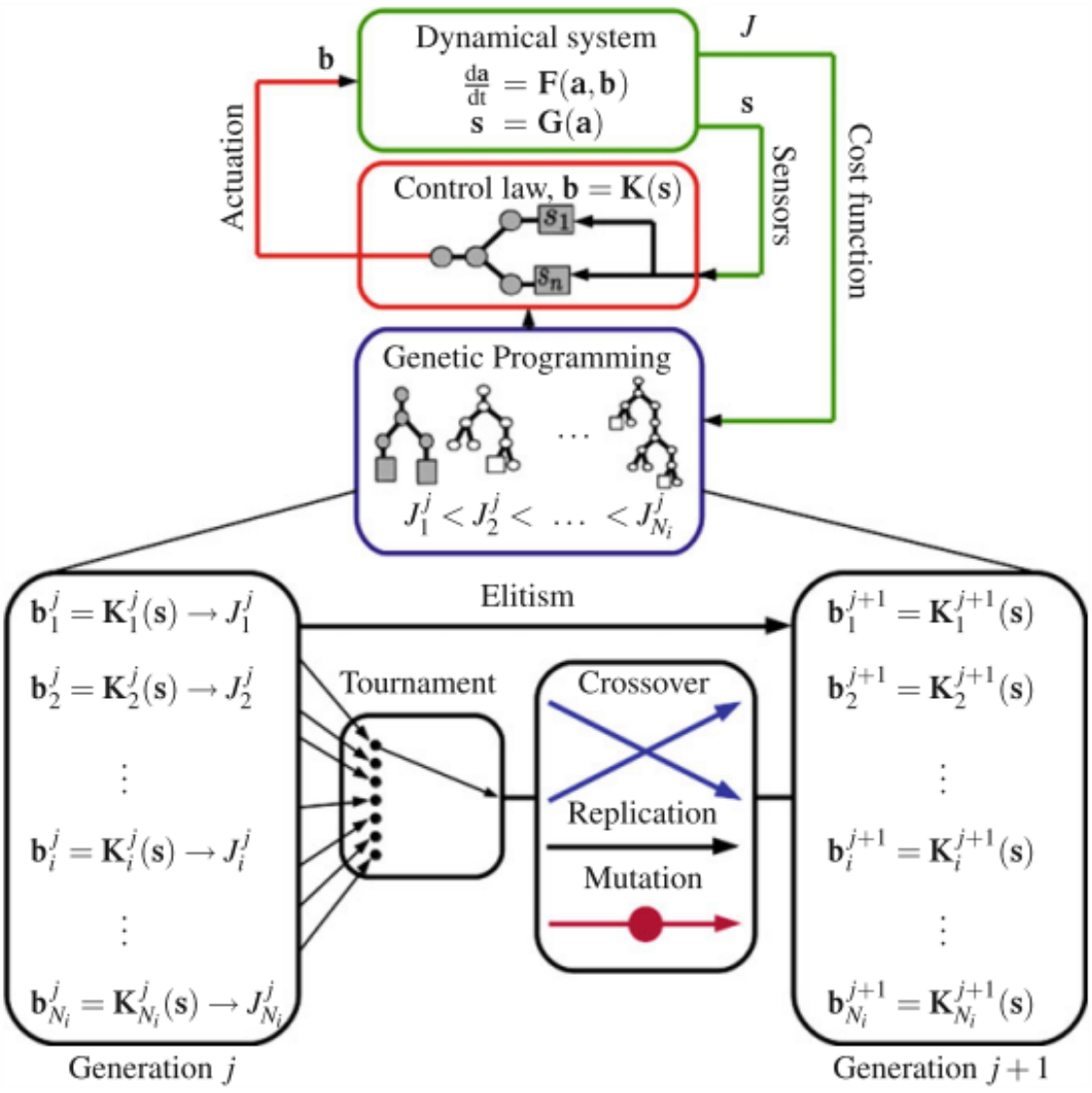

Figure 2.7: Control design for machine learning control applied to dynamical system, taken from [9]

the state of the flow and it has to be ensured that the used sensors are able to accurately measure these quantities without too much noise. This is further discussed in section 2.2.2 for the sensors used as control inputs and in sections 2.2.3 and 3.3 for the sensors used for the determination of costs. Moreover, real world actuators are subject to limitations e.g. in actuation strength, response time or the set of possible states. More details on the actuators can be found in section 3.

Details on the tested cases and selected parameters can be found in section 3.5.

2.2.2 Feature engineering

In classical machine learning, a feature is an individual measurable property or characteristic of a phenomenon being observed [2]. The target of feature engineering is to identify or create features that are particularly useful for the machine learning process. For a turbulence control experiment, features can be raw sensor signals, artificial signals derived from raw sensor signals or other completely artificial signals.

Raw sensor data is available from five microphones and two time resolved pressure sensors (Kulite sensors). The microphones are located at the base of the bluff body model, arranged in a vertical line along the span-wise middle of the model. The pressure sensors are located in the far wake of the model, also arranged in a vertical line, one on either side of the middle of the wake. Both sensor groups are supposed detect the state of vortex formation and shedding. The microphones are capable of picking up pressure fluctuations at the base of the model. Each side of the model's base should experience a decrease in pressure while a vortex is forming and an increase after the vortex has shed. This pressure footprint of vortex formation has been observed by Pastoor et al [24] on a similar model. Equally, a vortex passing one of the time resolved pressure sensors in the wake should be noticed as a short drop in pressure. The pressure sensors have the advantage of being less sensitive to acoustic noise in the wind tunnel but have the disadvantage of being less sensitive in general due to their relatively high pressure range.

Figure 2.9 shows the power spectral density of the raw microphone signals measured at a Reynolds number of about $4.6 \cdot 10^4$. The microphones are arranged in a vertical line with microphone one being in the bottom most position and microphone five in the top most position. Peaks in the spectra can be seen close to 30 Hz, 60 Hz and 120 Hz. The largest peak is at 60 Hz, corresponding to a Strouhal number of about 0.23. This is in good accordance with the Strouhal number observed for a D-shaped bluff body by Pastoor et al [24] and can therefore be identified as the natural vortex shedding frequency for this flow. It shall be noted that while this frequency is dominant especially in the signals of the outermost microphones, it is hardly relevant at all in the signal of the microphone positioned in the middle. The inverse is true for the peak at 120 Hz. This frequency is more dominant in signals of microphones closer to the middle. This can also be explained with vortex shedding. During one vortex shedding period, two vortices are shed form the body. One from the upper and one from the lower side. As it is visible in figure 2.8, a vortex is causing the highest pressure drop on the side from which it is rolling up. Pressure fluctuations picked up by the outer microphones are therefore dominated by one of the two vortices forming within the natural vortex shedding period. A microphone in the middle senses a smaller pressure drop from each vortex but is affected by both vortices equally. Fluctuations therefore occur at twice the natural shedding frequency. The peaks at 60 Hz and 120 Hz show that the microphones are able to pick up information about the vortex shedding process. The peak near 30 Hz can not clearly be linked to a flow phenomena. It is possible that every second vortex shed from one side is a little stronger. It could also be noise from the motor driving the wind tunnel that was running at 30 Hz during this measurement.

Figure 2.10 is showing the power spectral density of one raw Kulite pressure sensor signal measured at a Reynolds number of about $4.6 \cdot 10^4$. Even though the raw signal is very noisy, the spectra

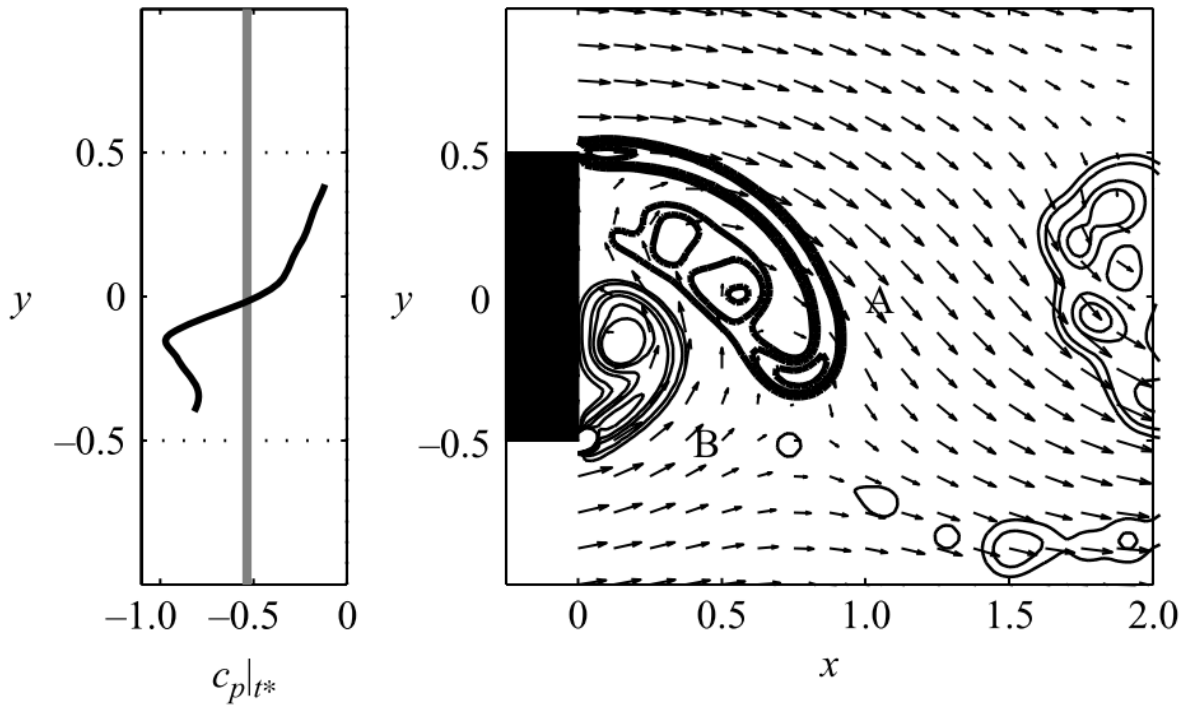

Figure 2.8: The footprint of a forming vortex in the pressure distribution on the base of a D-shaped bluff body, taken from [24]

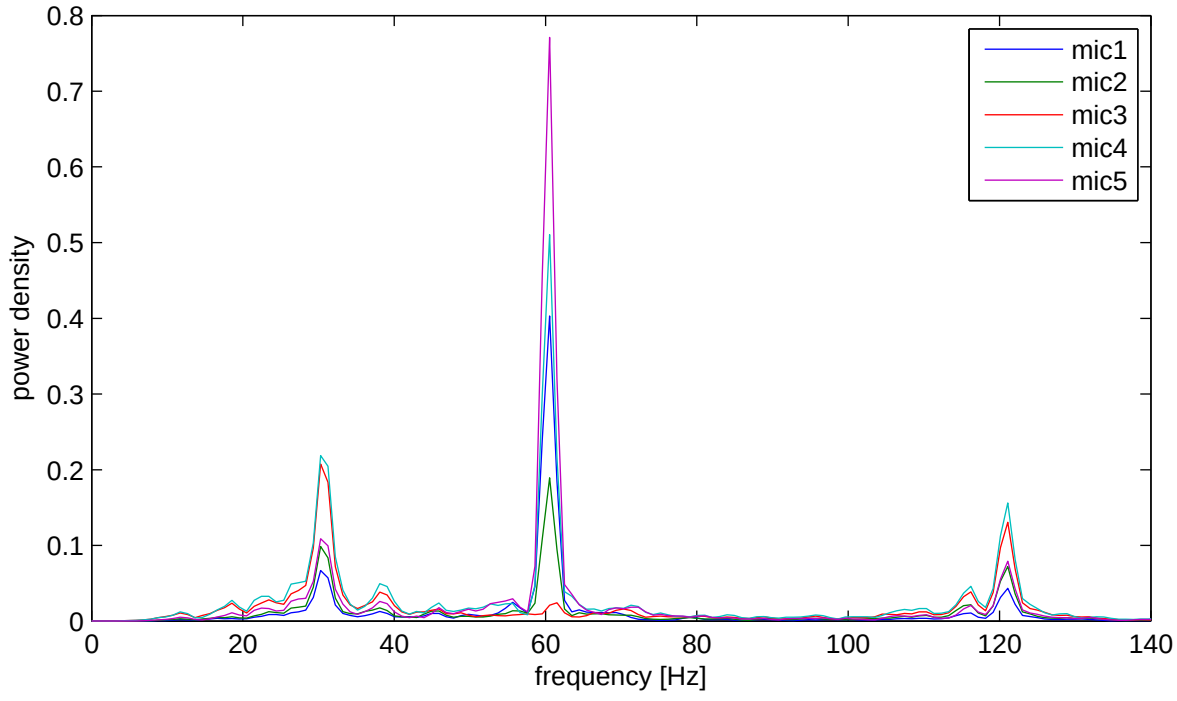

Figure 2.9: Power spectral density of the raw microphone signals for flow at $Re = 4.6 \cdot 10^4$

is showing a clear peak at about 60 Hz. This shows that the Kulite pressure sensors are able to pick up information about the vortices also. It has to be noted that while the microphones can only measure pressure fluctuations, the pressure sensors measure the pressure difference relative to reference pressure level.

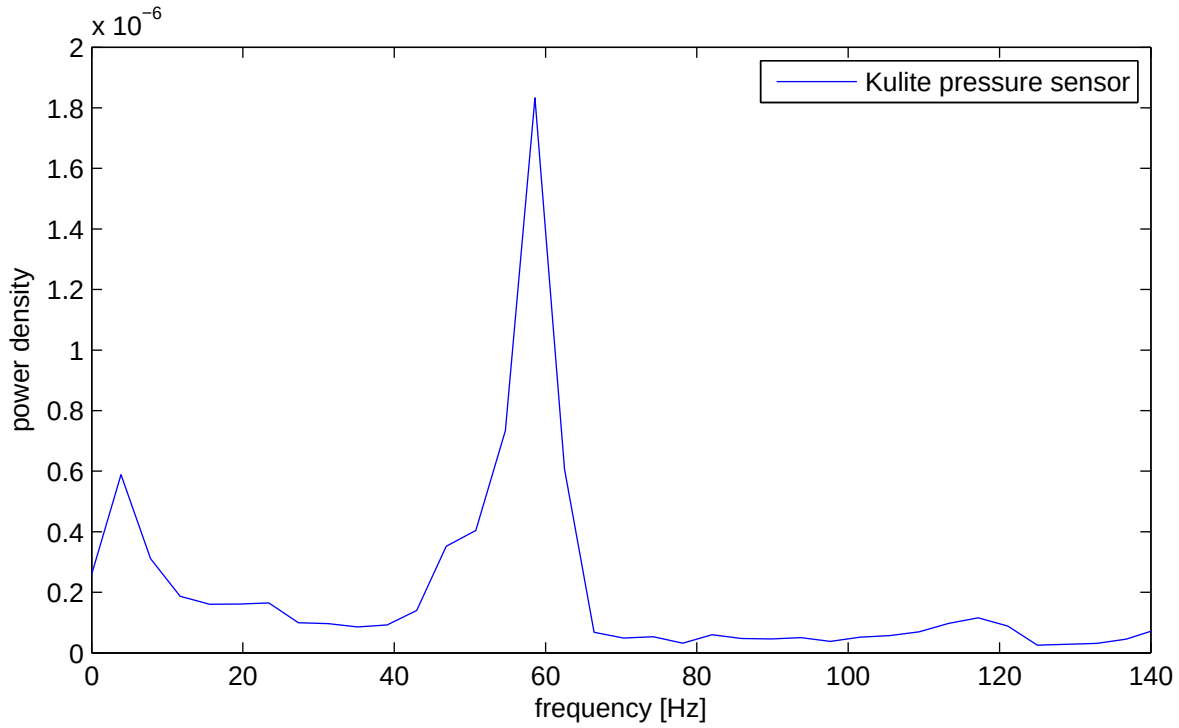

Figure 2.10: Power spectral density of Kulite pressure sensor signal for flow at $Re = 4.6 \cdot 10^4$

The raw sensor signals are the most obvious feature and the primary source of information about the state of the flow. Other features are mostly based on the attempt to extract additional information from the available sensor data. Table 2.2 gives an overview over all used features.

Feature	**Benefit**
raw signals	detect vortex shedding state from spacial distribution
filtered signals	attenuation of noise
standard deviation	detect fluctuation
time delay	detect vortex shedding state from temporal progression
difference between raw signals	detect phase of vortex
artificial sinus signals	provide stable clockwork signals

Table 2.2: Summary of features to be used by MLC as control law inputs

Filters can be applied to the sensors to remove unwanted parts of a signal, like noise. It has been observed that significant noise is coming from the opening of fast switching valves inside the model that control the flow through the blowing slots. When the valves are opened, a sharp negative peak can be observed in the microphone signals. This is shown in figure 2.11. An actuation signal of 0 V means the valves are closed. An actuation signal of 5 V means the valves are opened.

To filter out this and other potential noise, a Butterworth low pass filter is used. The cut-off frequency is chosen to be 100 Hz to prevent filtering out relevant fluctuations in the flow. The effect of the filter on a microphone signal is shown in figure 2.12. In this figure the voltage of the actuation signal opening the valves has been chosen to be 10 V. In contrast to figure 2.12 this

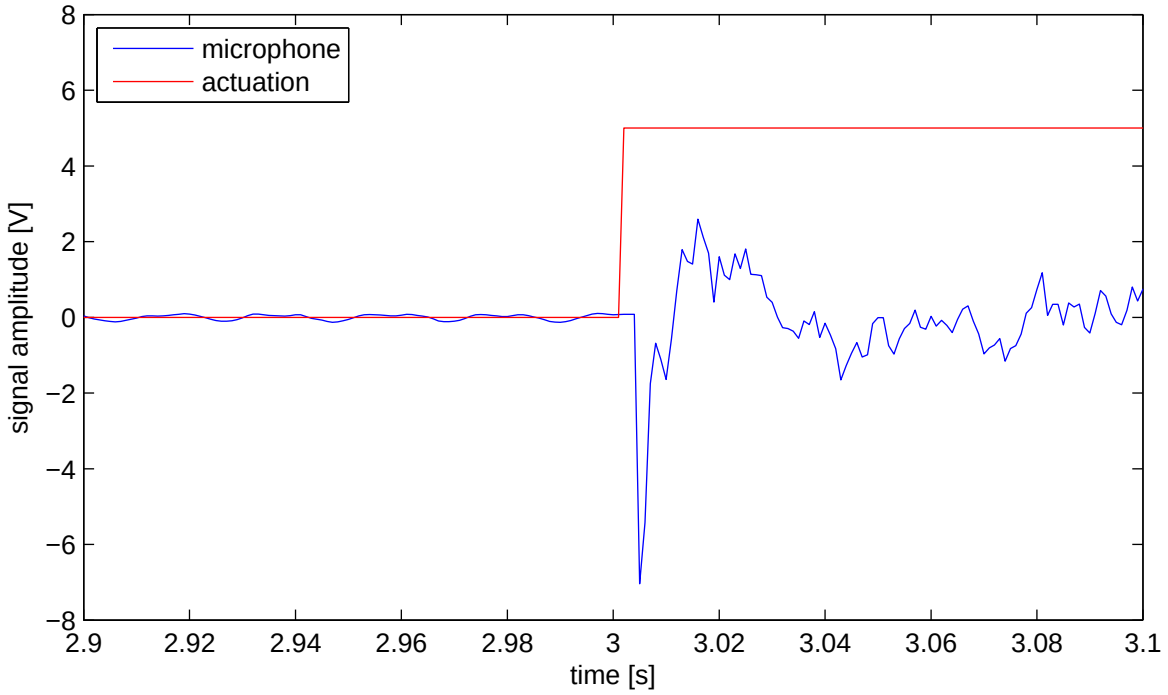

Figure 2.11: Impact of a switching valve on a microphone signal without flow through the wind tunnel

shows a set of signals measured when the wind tunnel was switched on. The noise from the valves is therefore less dominant. It can still be seen as first sharp negative peak after the opening of the valves and is successfully filtered out in the filtered signal. As expected, the filtered signal is less noisy overall and also has a small time delay of about three milliseconds.

As mentioned by Duriez et al [9], while filtering is useful to attenuate noise it also introduces a bias that can prevent MLC form finding unexpected mechanisms. The filtered signals are therefore added as separate features beside the raw sensor data.

Another approach to extract additional information from the raw data is to use the standard deviations of the the sensor signals. The standard deviation is calculated by the formula:

$$\sigma = \sqrt{\frac{1}{n}\sum_{i=1}^{n}(x_i - \overline{x})^2} \tag{2.14}$$

with n being the number of data points in a given signal, x_i a single value of the signal and $\overline{x}$ the mean value of the signal. To be able to use the standard deviation as a feature and therefore an input to a control law, it has to be calculated based on a sliding window of past signal values. Figure 2.13 shows a microphone signal and the derived standard deviation signal calculated based on a sliding window over the past 50 milliseconds.

The standard deviation quantifies how much a signal fluctuates within a given period of time. A connection between fluctuations in the flow and the time averaged drag has been observed in several previous experiments and even used for closed loop control by Dahan et al [5] and Dalla Longa et al [6]. Dalla Longa et al also provide a theoretical basis for this connection. Similar to how it's been described in section 2.1, they use mass and momentum conservation for a control volume around the body to find a term describing the drag coefficient. However, they consider time-dependent, fluctuating flow parameters. After splitting the time dependent parameters

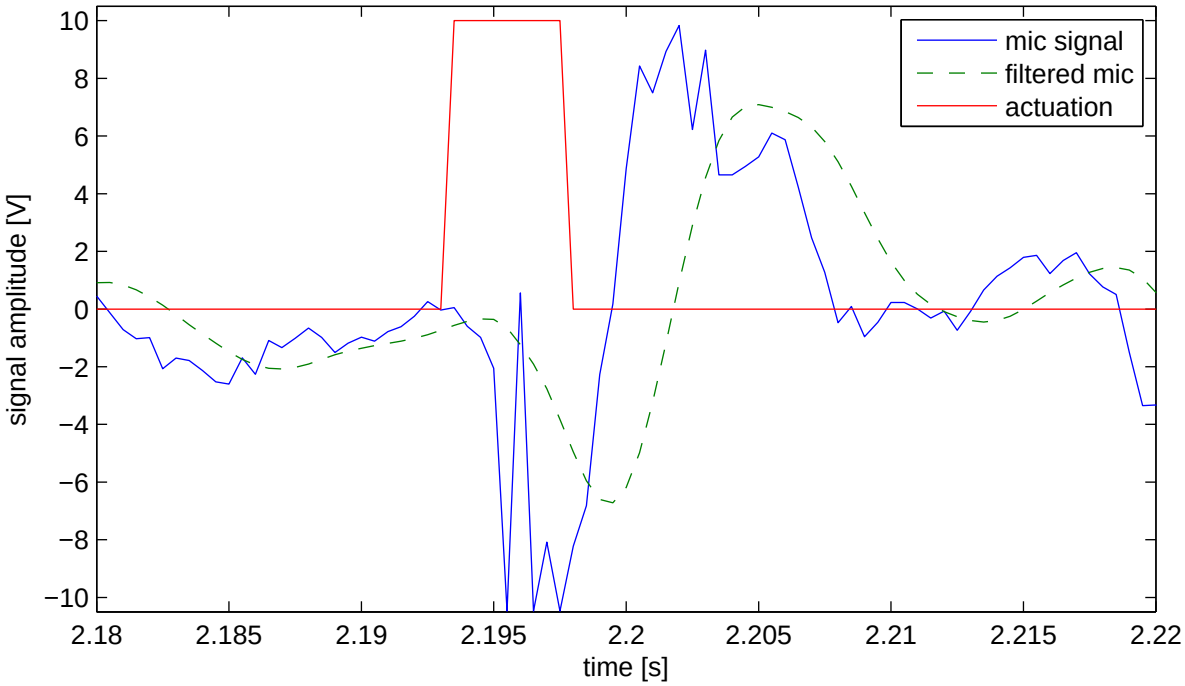

Figure 2.12: Impact of a switching valve on a microphone signal and a low pass filtered microphone signal a $Re = 5.0 \cdot 10^4$

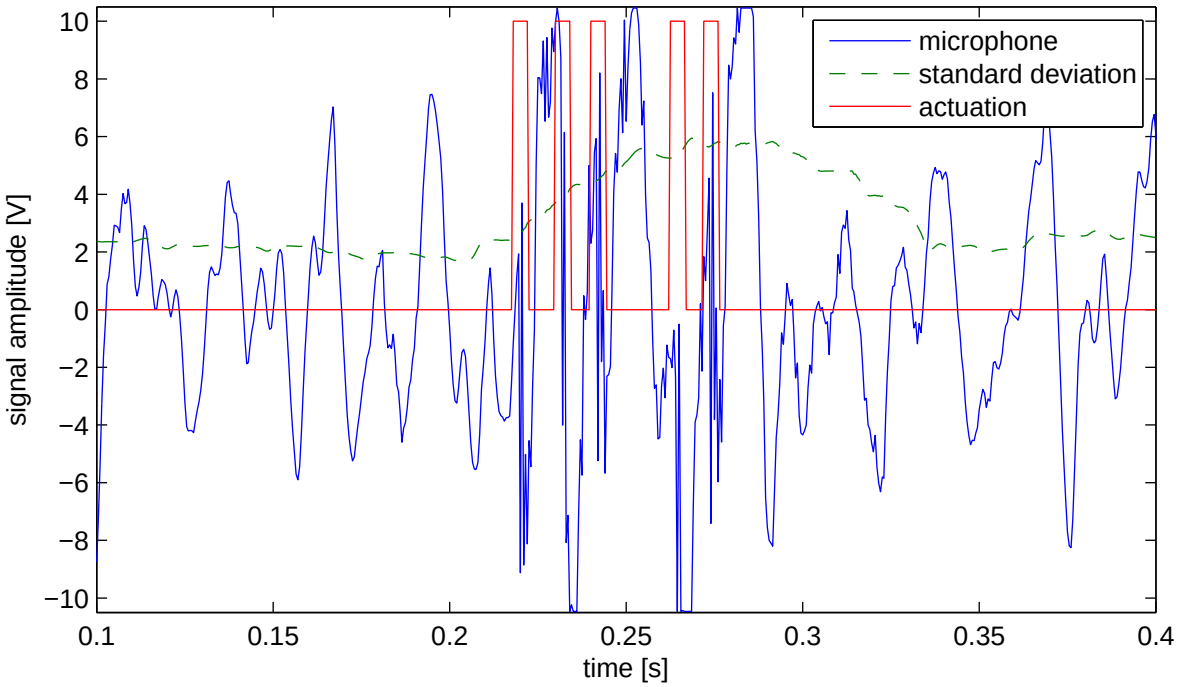

Figure 2.13: A microphone signal and it's standard deviation during partly actuated flow at $Re = 5.0 \cdot 10^4$

into averaged and fluctuating components, they are able to identify fluctuating components that contribute to a time averaged drag coefficient.

Furthermore it can be useful to provide a time delayed signal as an additional feature. This adds information about the temporal progression of a signal that would otherwise not be available to a control law as it only acts on instantaneous values of it's inputs. For a periodically oscillating signal like the microphone and pressure sensor signals, it is important to choose the right amount of time delay. A badly chosen time delay e.g. close to one period of the oscillation of the original signal would lead to a time delayed signal that differs from the original signal only by the noise level. Instead, a time delay of a quarter period is seem as a sensible choice. This corresponds to phase shift of -90 degree. If the original signal was a perfect sine wave, the time delayed signal would be a negative cosine wave. The original signal would therefore be the slope of the delayed signal. Even for a less perfect signal, the difference between original and delayed signal would still be a good indication for whether the original signal is increasing or decreasing. So far, the chosen time delay still depends on the oscillation period of the sensor signals. Without actuation, this would be the natural vortex shedding period. During an active turbulence control experiment however, the period might be different and throughout an MLC experiment, many different periods might occur. For practical considerations, the time delay still has to be constant. To choose a time delay, results from the open loop turbulence control experiments discussed in section 4.3 are used. It is assumed that the state of the flow during a good closed loop control run is similar to that during a successful open loop control run. When the highest drag reduction was achieved, the dominant frequency of the microphone signals was close to 100 Hz, corresponding to a period of about 10 milliseconds. The time delay has therefore been fixed to 2.5 milliseconds. Figure 2.14 shows a microphone signal and the corresponding time delayed signal during partly actuated flow at $Re = 5.0 \cdot 10^4$.

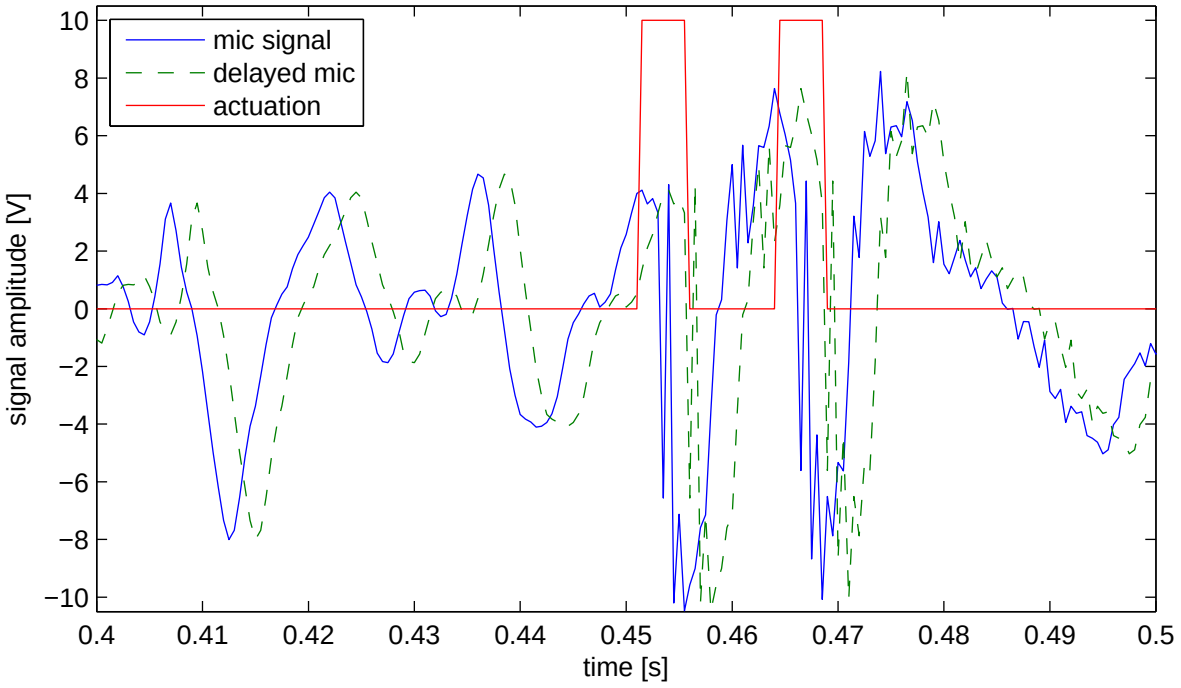

Figure 2.14: A microphone signal and the corresponding time delayed signal during partly actuated flow at $Re = 5.0 \cdot 10^4$

Additionally, the differences between fixed microphone signals have been chosen as features for MLC. For example the difference between the signal from the microphones in the uppermost

(microphone five) and lowermost (microphone one) position. This shall give information on the phase shift between the pressure fluctuations on the upper and lower side of the base. When vortices are shedding undisturbed, a phase shift of 180 degrees is expected, resulting in a strong difference signal whenever the individual signals reach their respective maximum and minimum. If vortex shedding is disturbed the difference signal is expected to be lower and reach values close to zero if both fluctuations are in phase. This yields the additional benefit that acoustic noise should be attenuated in the difference signal also, as the disturbances from a source of acoustic noise should reach all microphones with little phase shift, especially if the source is far away from the model. Figure 2.15 shows signals of the microphones one and five, sitting closest to the trailing edges of the blunt base and the difference signal during partly actuated flow at $Re = 5.0 \cdot 10^4$. Before a short burst of actuation, approximately up to second 0.45, a phase shift close to 180 degrees is visible between the two raw microphone signals. This further supports the previous observation that the microphones are able to detect the pressure footprint of vortex shedding. The difference signal oscillates at the same frequency and higher amplitude. After the actuation signal opens the valves for a short moment, both microphone signals react simultaneously and in phase. This can be attributed to valve noise coming from both sides at the same time but also the effect of the Coanda jets disturbing the vortex formation structure. The difference signal is hardly affected by this at all. It can be concluded that the difference signal attenuates in-phase components of two signals while it amplifies out-of-phase components.

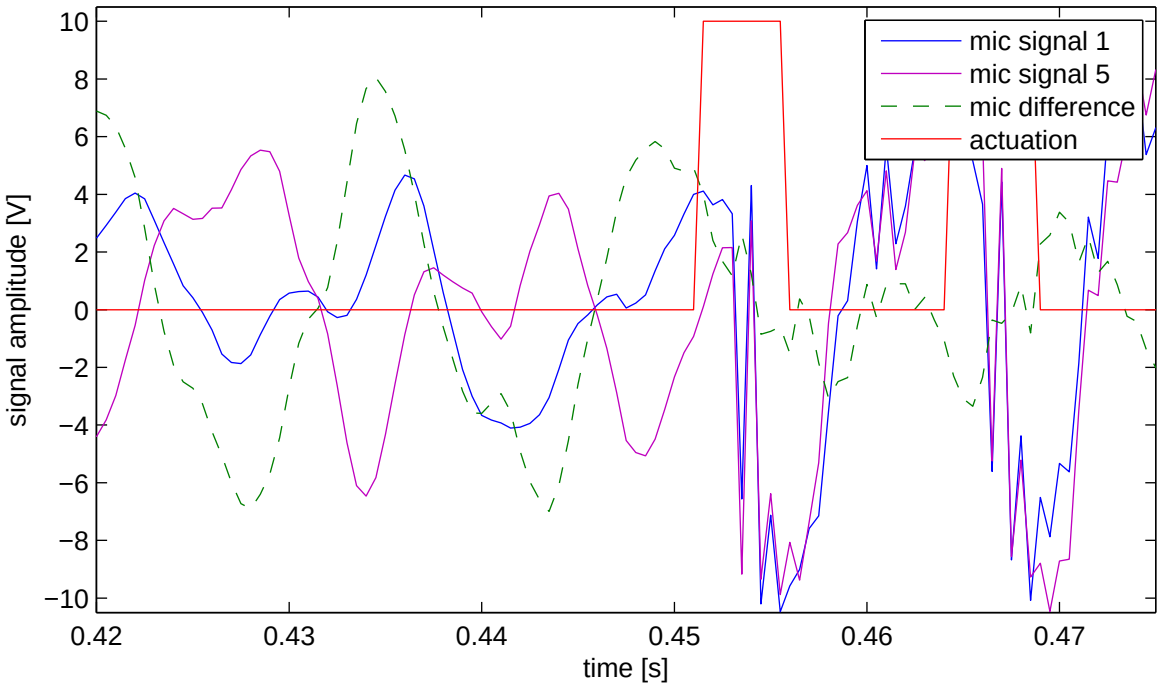

Figure 2.15: Signals of the microphones one and five, sitting closest to the trailing edges of the blunt base and the difference signal during partly actuated flow at $Re = 5.0 \cdot 10^4$

This observation is supported by analysis of the power spectral densities of the two microphone signals and the difference signal as shown in figure 2.16 for unactuated flow at $Re = 4.6 \cdot 10^4$. The peak at about 60 Hz that has already been linked to the natural vortex shedding frequency in figure 2.9 is stronger in the difference signal than in any of the raw microphone signals. This supports the claim that this part of the signal really is linked to the natural vortex shedding process. The peak at about 30 Hz has almost disappeared in the difference signal, further supporting the suspicion the at that it could be linked to noise from the wind tunnel motor sitting relatively far away from the model reaching both microphones at the same time.

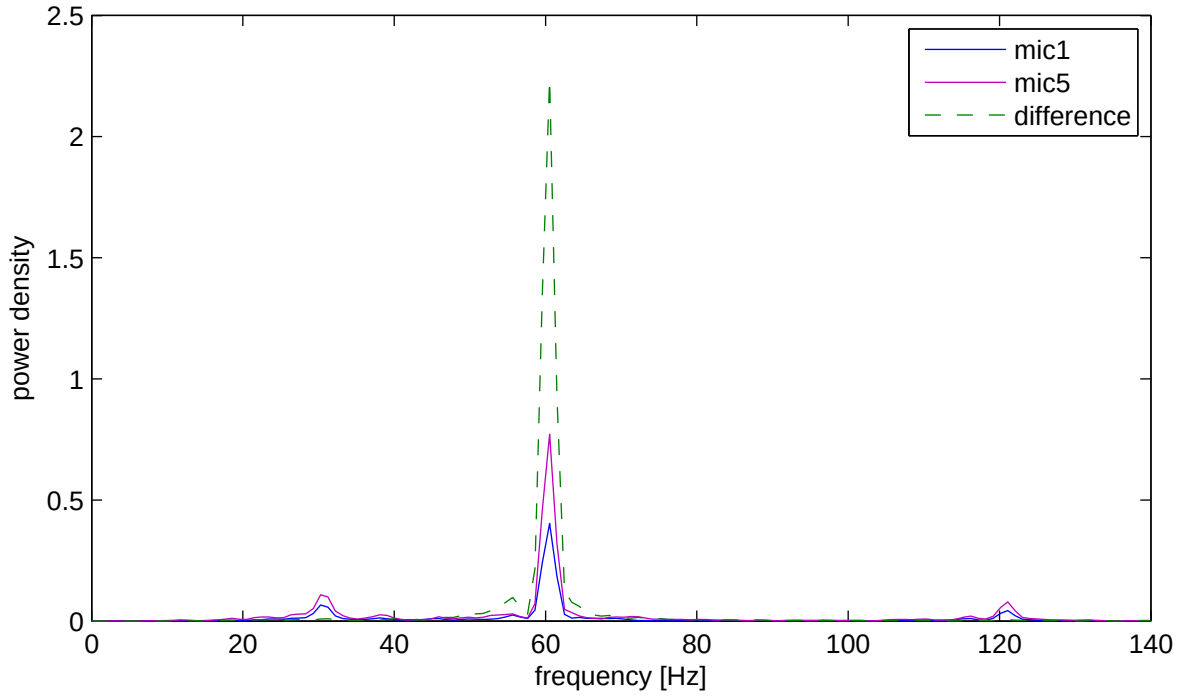

Figure 2.16: Power spectral density of microphones one and five, sitting closest to the trailing edges of the blunt base and the difference signal during unactuated flow at $Re = 4.6 \cdot 10^4$

The difference signal feature could also be seen as a branch of a subtraction node and two microphone signal leaves and MLC could have come up with this all by itself. It has been decided to explicitly give this as a feature nevertheless. This way the evolutionary process doesn't have to come up with the branch itself and the branch is also protected from being destroyed by mutation. This is expected to improve the convergence speed of MLC. MLC can however still come up with the same branch or variations of it that could be even more useful.

Finally, the last feature added to the list is a set of artificial sinus signals. Duriez et al [9] suggest using this as a steady, plant independent clockwork that can help stabilizing the flow. This can be combined with sensor signals in an expression tree to adjust the amplitude or superimpose other frequencies. Parezanović et al [23] suggest the introduction of time as an input variable to enable MLC based optimization of open-loop control. This is also achieved by the addition of artificial sinus signals depending only the elapsed time. The chosen frequencies are the natural vortex shedding frequency multiplied with different powers of the golden ratio. This ensures that no frequency is close to another frequency's harmonic and so a wide spectrum of frequencies and harmonics can be covered. The natural vortex shedding frequency under the conditions during closed loop experiments was 70 Hz. The chosen powers range from minus to plus three. The frequencies and corresponding Strouhal numbers are given in table 2.3.

For all features it has to be mentioned that while they provide additional information for MLC to work with, they also introduce a bias that could potentially prevent MLC from finding unexpected drag reduction mechanisms, as Duriez et al [9] argue for the application of filters to sensor signals. In terms of the search space, one could argue that this bias makes it easier to find certain minima that work with the flow characteristics the features are designed to detect but diverts the search from other potentially interesting minima. The choice of features therefore means a compromise between adding more information or adding less bias. The approach chosen for the following experiments is to provide as much information as possible to MLC and let it choose which

Golden ratio power	Frequency	Strouhal number
-3	16.52	0.055
-2	26.74	0.089
-1	43.26	0.144
0	70.00	0.234
1	113.26	0.378
2	183.26	0.612
3	296.52	0.990

Table 2.3: List of sinus signal frequencies to be used by MLC as artificial sensors

features it can work with best.

Furthermore it is advantageous for all sensors and the derived features to be of the same order of magnitude and in the range of a sensible actuation command. The actuation command can be in a range from 0 to 10 V. The microphone signals have a maximum range of +/- 10 V. This satisfies the requirement. The Kulite pressure sensors provide a considerably lower signal due to their wider pressure range and therefore have to be scaled up. A test measurement under the same Reynolds number as used in the closed loop experiment has provided a typical signal range. A scaling factor of 200 has been found to be suitable to get a signal in the range of +/- 10 V also. All derived features can be expected to be of the same order of magnitude also.

2.2.3 Cost function

As mentioned in section 2.2.1 MLC can be used to optimize more than one objective. In order to quantify how good an individual performs in fulfilling the objectives, one or more cost functions have to be defined. For closed loop turbulence control two objectives are considered, reduction of drag and reduction of energy invested in actuation. The drag reductions is determined by the drag coefficient as explained in section 2.1. The energy invested in actuation by blowing jets is commonly characterized by the momentum coefficient C_μ defined as,

$$C_\mu = \frac{\rho_j u_j^2 S_j}{\frac{1}{2}\rho_\infty u_\infty^2 S_0}, \tag{2.15}$$

with the subscript j referring to jet properties, S_j being the cumulative slot cross-section and S_0 a reference surface area. As described by Chabert et al. [4] based on Greenblatt and Wygnanski [14], for periodic blowing the oscillatory momentum coefficient $\langle c_\mu \rangle$ has to be considered. It is defined as,

$$\langle C_\mu \rangle = \frac{\rho_j \left\langle u_j^2 \right\rangle S_j}{\frac{1}{2}\rho_\infty u_\infty^2 S_0}, \tag{2.16}$$

with the time averaging operator $\langle\rangle$. The valves used to control blowing can only be opened or closed. For sufficiently large actuation periods in comparison to the valve opening time, the jet velocity can in good approximation be described as,

$$u_j(t) = \begin{cases} u_j & \text{if} \quad 0 < t < \alpha T, \\ 0 & \text{if} \quad \alpha T < t < T, \end{cases} \tag{2.17}$$

with α being the duty cycle and T the period of the periodic actuation signal. For the time average this means,

$$\left\langle u_j^2 \right\rangle = \alpha \cdot u_j^2. \tag{2.18}$$

Inserting this into equation 2.16 yields

$$\langle C_\mu \rangle = \alpha \frac{\rho_j u_j^2 S_j}{\frac{1}{2}\rho_\infty u_\infty^2 S_0}. \tag{2.19}$$

Due to time constraints, the actual jet velocity u_j could not be measured and thus the actual momentum coefficient could not be determined for the following experiments. However, assuming that periodic actuation results in the same jet velocity as constant actuation and comparing equation 2.15 to equation 2.19, one can find that,

$$\langle C_\mu \rangle = \alpha \cdot C_\mu. \tag{2.20}$$

This shows that the oscillatory momentum coefficient depends linearly on the momentum coefficient and the duty cycle. For a given slot geometry, free stream conditions and jet supply pressure, the momentum coefficient is constant. Then the oscillatory momentum depends only on the duty cycle. Furthermore, by

$$\alpha = \frac{\langle C_\mu \rangle}{C_\mu}, \tag{2.21}$$

one could understand the duty cycle as a oscillatory momentum coefficient scaled to a range of 0 to 1 by the momentum coefficient. The duty cycle therefore serves as an abstract measure for the energy invested in actuation. This does not allow a direct comparison between energy saved by drag reduction and energy invested in actuation but it allows the comparison of actuation energy used by different control laws.

For open loop control with a periodic actuation at single frequency, the frequency and duty cycle are set directly. For closed loop control on the other hand, the duty cycle has to be determined from the, not necessarily periodic, actuation signal. Instead of considering what percentage of a period the valves are opened, it is calculated what percentage of the full time one control law is tested the valves are opened. As the valves are either fully opened of fully closed and the actuation signal is either zero or a fixed opening voltage, similar to equation 2.17, one can write for each slot i,

$$u_{j,i}(t) = \begin{cases} u_j & \text{if} \quad b_i(t) = b_{open}, \\ 0 & \text{if} \quad b_i(t) = 0, \end{cases} \tag{2.22}$$

with $b_i(t)$ being the current actuation signal for slot i and b_{open} the fixed opening voltage. The duty cycle can then be calculated as,

$$\alpha = \frac{\sum_{i=1}^{n} \sum_{t=0}^{T_{test}} b_i(t) \cdot \Delta t}{n \cdot T_{test} \cdot b_{open}}, \tag{2.23}$$

with n being the number of blowing slots, T_{test} the full time one control law is tested and Δt the time step for the update of the actuation signal. As $b_i(t)$ remains constant over Δt the summation equals an integration in time.

The duty cycle is used as a measure for how well the objective of minimal actuation energy is met. For multi-objective optimization the drag coefficient and duty cycle are used as two separate cost functions. For single-objective optimization, both cost functions are merged into one by a weighted linear combination similar to equation 2.13,

$$J = C_D + \omega \cdot \alpha. \tag{2.24}$$

To determine the weighting factor ω, the drag coefficient and duty cycle for a case without blowing and with constant blowing are considered. From this it can be concluded how much the

drag can be lowered when the maximum amount of actuation energy is invested. By defining ω so that J for the constant blowing case is the same or higher than J for the case without blowing, a control law will only be considered better than any of the two extreme cases if it uses a more efficient drag reduction mechanism than constant blowing. Equal cost function values J for both extreme cases would result from a weighting factor ω of 0.222. To leave a margin for measurement errors a slightly higher value of 0.25 is chosen. The resulting values are summarized in table 2.4.

	C_D	α	ω	J
no blowing	0.759	0	0.25	0.759
constant blowing	0.537	1	0.25	0.787

Table 2.4: Comparison of the drag coefficients C_D and duty cycles α for a no blowing and constant blowing case of the model with attached Coanda flaps at $Re = 5.0 \cdot 10^4$ and the resulting cost function values J for a given weight ω

Chapter 3

Experimental setup

3.1 Wind tunnel

The experiments are conducted at the LNB ("Leiser Niedriggeschwindigkeitswindkanal Braunschweig") at the insitute for fluid mechanics of TU Braunschweig. It is a continuous atmospheric Eiffel type open return wind tunnel with room recirculation and a closed test section. It has a Burger-type nozzle with a contraction ratio of 16:1. The outside of the nozzle and the inside of the diffuser are covered with acoustic foam to minimize noise reflection. To reduce turbulence, incoming air flows through a 30 mm fleece mat, a 133 mm honeycomb and a fine woven screen. The resulting degree of turbulence is below 0.1 % at 10 m/s. The test section has a width of 400 mm, a height of 600 mm and a length of 1500 mm. To compensate for the growth of the boundary layer on the walls of the test section, the rest section has a horizontal opening angle of 1 degree.The flow is driven by a 9-blade fan sitting at the end of the diffuser.

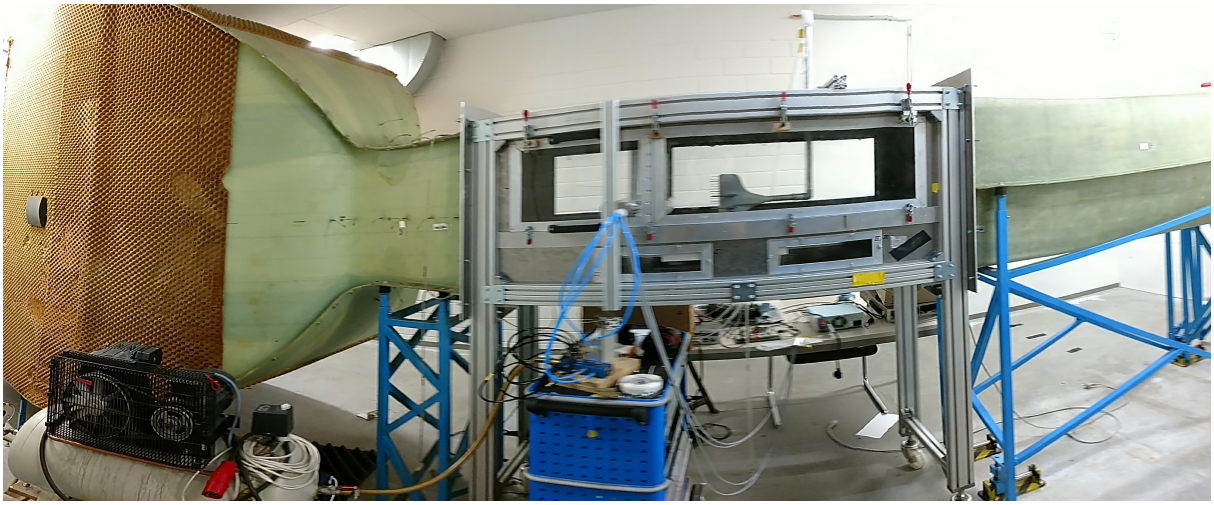

Figure 3.1: LNB wind tunnel with foam covered nozzel on the left, windowed test section in the middle and diffuser on the right

3.2 Model

The model used in the experiments is a D-shaped bluff body with a blunt trailing edge. It has a height of 53.4 mm, a length of 190.6 mm and a width of 390 mm. It is mounted horizontally

in the wind tunnel and held by one steel tube from each side. The model spans the entire width of the test section. The flow is therefore assumed to be two-dimensional, apart from wall effects on the side-walls of the tunnel.

Figure 3.2 shows a sketch of the shape of the model together with the positions of 36 pressure taps that are distributed over the models surface along it's span-wise centre line. The pressure taps are connected to a pressure measurement system outside the test section by rubber tubes. and provide information on the surface and base pressure distributions.

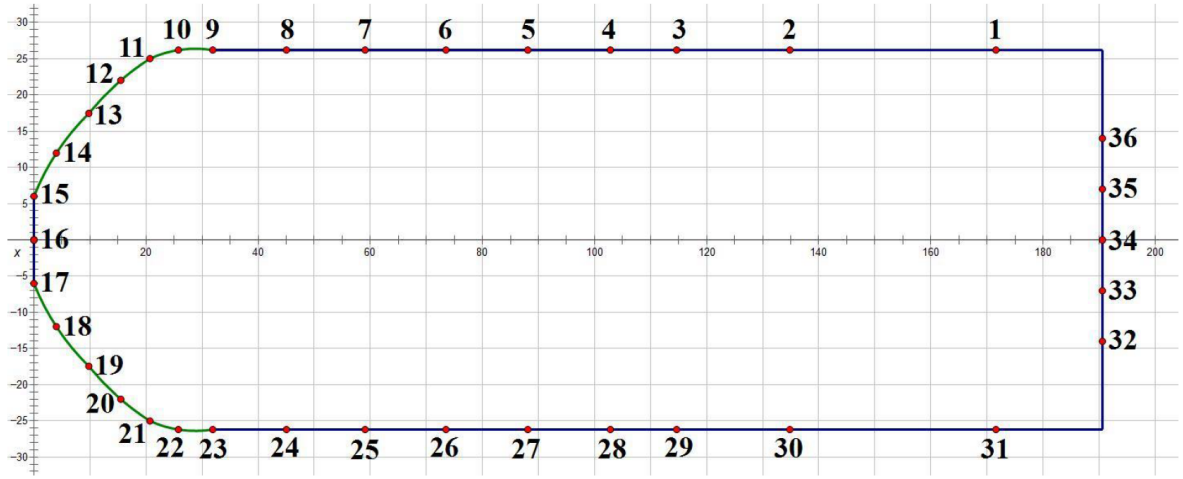

Figure 3.2: Geometry of the D-shaped body model and distribution of pressure tabs indicated by red dots and numbered

The base configuration of the model with its blunt trailing edge can be modified by the addition of trailing edge flaps or Coanda surfaces. Trailing edge flaps for passive drag reduction are attached in a way that their surface is sitting flush with the upper/lower surface of the body and no gap is formed in horizontal or vertical direction. They form a direct continuation of the body. Four different flap geometries are tested. Two linear flaps, inclined inwards with angles of 5 degrees and 10 degrees are tested to provide comparison for two flap geometries optimized numerically by a genetic algorithm in a previous investigation at the institute. The optimized flap geometries follow polynomial shapes. One was optimized with the constraint of a horizontal tangent at the attachment to the model, the other was optimized free of constraints. The four geometries are shown in figure 3.3. Figure 3.4 shows one pair of flaps attached to the base of the model.

The model furthermore has two blowing slots at the trailing edges that are covered in the base configuration. Coanda flaps can be attached from the inside of the model and extend outwards through the slots. Outside the model the Coanda flaps have a round shape with a radius of 9.4 mm that was also determined by numerical simulations and a genetic algorithm. The passive trailing edge flaps and Coanda surfaces have been manufactured by rapid prototyping and are therefore made of plastic. After manufacturing they have been sanded carefully with sand paper of a grit size of up to 4000 to ensure a smooth surface.

With installed Coanda flaps, the slot height can be adjusted by a set of fine threaded adjusting screws that push against the inner surface of the flaps. The adjusting screws allow to ensure a defined, uniform slot height. A slot height of 0.25 mm is set with and checked with the help of a feeler gauge. The uniformity of blowing from each slot was tested by inserting a fish mouth probe into the Coanda jet emerging from the blowing slot and traversing the probe in spanwise direction. The measured pressure distributions relative to ambient pressure are shown in figure 3.5 for both slots. Both distributions show four peaks exceeding 10 % deviation from the mean. The deviations could not be compensated by adjustments to the slot height and are

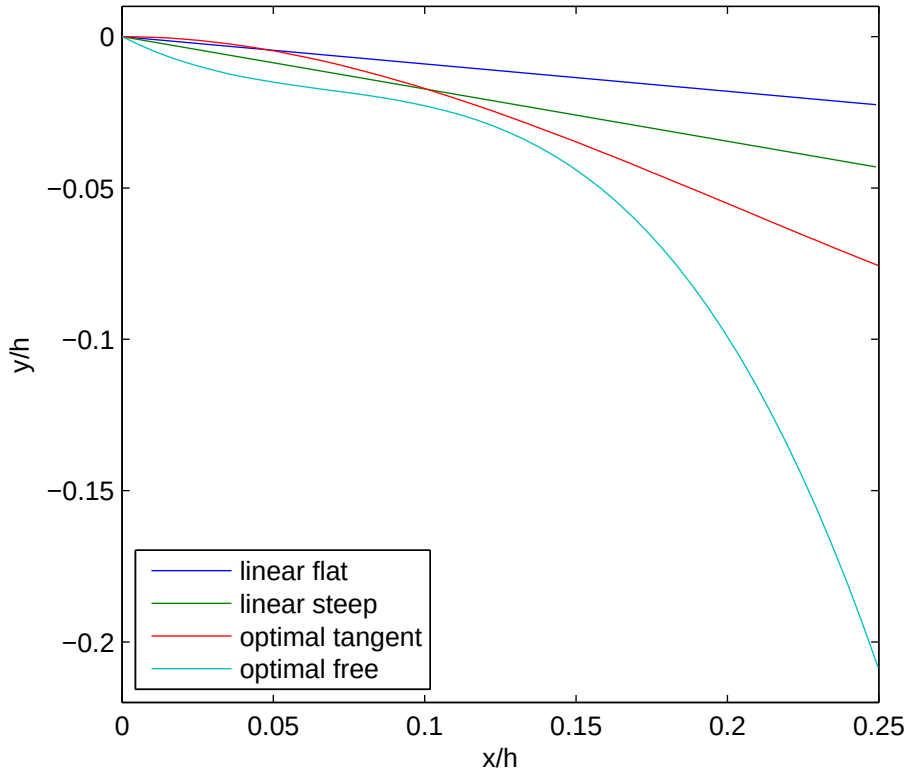

Figure 3.3: Passive flap geometries in coordinates normalized by the body height

Figure 3.4: Pair of trailing edge flaps attached to the model base

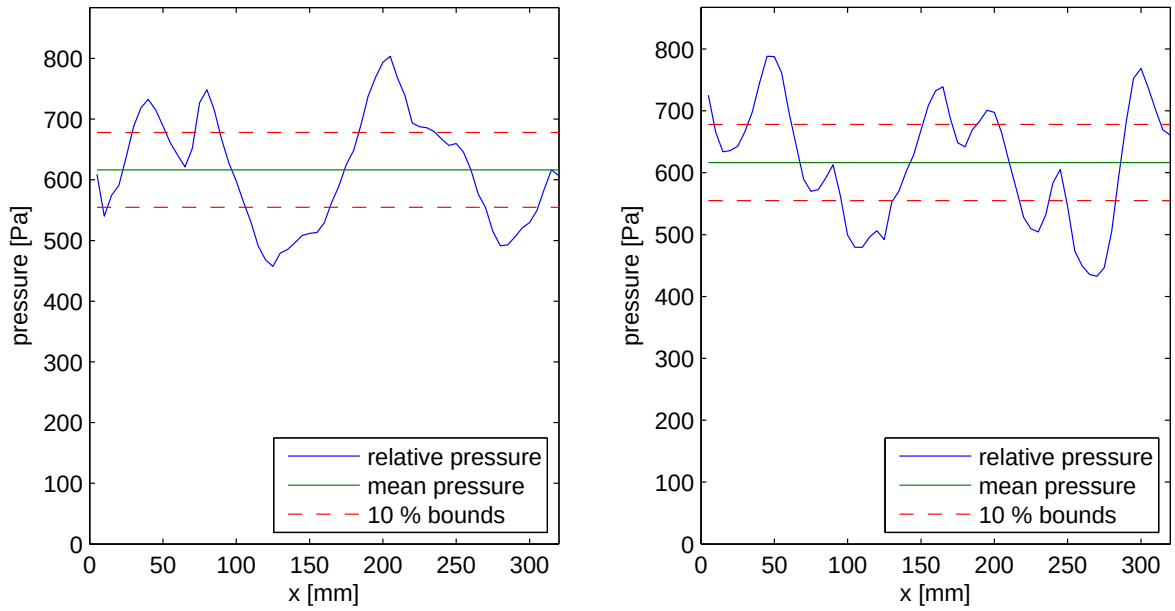

(a) Pressure distribution upper slot

(b) Pressure distribution upper slot

Figure 3.5: Distribution and mean of the pressures measured by a fish mouth probe in the jet, traversed in spanwise direction

likely linked to uneven pressure distribution between four blowing chambers that feed each slot. As the jet velocity depends on the root of the dynamic pressure, fluctuations in the jet velocity can be expected to be considerably lower. Due to time constraints the jet velocity could not be measured directly with a hotwire probe.

Unsteady actuation is enabled through eight Festo MHJ9-QS4-MF monostable 2/2-way valves with an operating pressure range of 0.5 to 6 bar. The valves can be operated at maximum frequency of 1000 Hz, the switching times depend on the supply voltage and operating pressure. For a supply voltage of 24 V and an operating pressure of 4 bar an opening time of 0.8 ms and a closing time of 0.4 ms are given in the data-sheet. Each blowing chamber is connected to a valve through 4 mm tube which are then progressively bundled to four 6 mm tubes and then a 12 mm hose and connected to a pressurized tank. The tank serves as a reservoir to reduce pressure fluctuations when opening and closing the valves.

Furthermore, five TOM-1545P-R microphones are located along the backside of the body to detect pressure fluctuations in real time. They are installed in small cavities on the inside of the models back, facing outward through holes similar to pressure taps. The microphones have a sensitivity of -45 dB and a signal-to-noise ratio of more than 60 dB. Their output signal is amplified to be in the range of ± 10 V. They are placed in a vertical line next to the actual pressure taps on the back of the model, at the same vertical positions.

3.3 Measurement techniques

Two different rakes are used for the measurement of the pressure distribution in the wake of the model. For measurements with the base configuration and passive trailing edge flaps a smaller rake is used that has to be traversed vertically to cover the whole wake. For active drag reduction experiments a newly built wider rake is used that can cover the entire wake in a single position. The ability to measure the entire pressure distribution without traversing the rake significantly

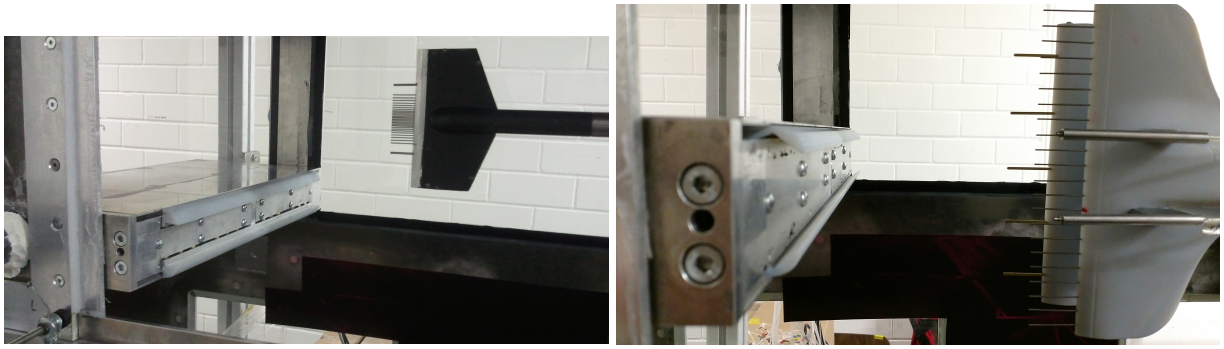

(a) Small rake

(b) Wide rake, with additional mounting points for Kulite pressure sensors

Figure 3.6: Both pressure rakes used for different experiments

reduces the workload and time spent on one measurement. This time reduction is necessary to enable machine learning control experiments.

The small rake, shown in figure 3.6a, consists of 27 Pitot probes to measure total pressure, surrounded by 2 Prandtl probes to measure total and static pressure. The Pitot probes are distributed unevenly with a higher density towards the middle of the rake. The Prandtl probes need higher distances to other probes to prevent an influence of the tip of a neighbouring probe on the static pressure taps of the Prandtl probe. The small rake spans 59.2 mm between both Prandtl probes.

The wider rake consist of 22 Pitot probes and 5 Prandtl probes. Pitot and Prandtl probes are mounted on two separate arms of the rake to allow full coverage of the static pressure distribution, sufficient space between Prandtl probes and neighbouring probes and a dense coverage of the total pressure distribution by Pitot probes. The probes on both arms have a uniform vertical distribution. The Pitiot tubes are arranged at 9 mm distance to each other. The Prandtl probes are spaced 40 mm apart. The wider rake spans 160 mm between the Prandtl probes and 189 mm between the Pitot probes.

The distance between the rake and the base of the model was chosen to be 130 mm for both rakes. As indicated by numerical simulation results shown if figure 4.6 this distance is sufficient to ensure that a rake is not in the recirculation region in the near wake of the body and the flow is at a low angle to the probes.

The pressures from the rakes and surface pressure taps are measured by a temperature compensated DTC Initium pressure measurement system with an ESP-64HD pressure scanner. The scanner has 64 channels and a pressure range of ± 7 kPa and a static accuracy of ± 0.03 % of the full range or ± 2.1 Pa. Measurement data can be accessed through a LabView VI via network connection.

Two Kulite time resolved pressure sensors are attached to the wider rake as additional inputs for the MLC experiments. They have a pressure range of $3.5 \cdot 10^4$ Pa and an accuracy of ± 0.1 % of the full scale or ± 35 Pa. The Kulite sensors are attached in parallel to the Pitot probes one above and one below the middle of the rake as seen in figure 3.6b.

3.4 MLC infrastructure

Closed loop control is implemented using an NI cRIO-9067 embedded real time controller with reconfigurable FPGA, an NI 9220 analogue input module and an NI 9264 analogue output

module. Evaluation of control laws is implemented directly on the FPGA allowing fast control, high determinism and fast access to sensor signals through the input module. The output of a control law is conditioned before it is returned as an actuation signal to the valves. First the output is compared to a trigger level to decide whether to open or close the valves. Furthermore the state of the actuation signal is held constant for a period of four milliseconds to ensure that the are given the time to fully open or close before their state is changed again. All features derived from the input signals are calculated on the FPGA within the control loop.

Besides the fast control loop between the FPGA and the experiment, MLC uses a slower learning loop to provide new control laws to the controller to be tested. The communication between all components of the MLC infrastructure is sketched in figure 3.7. The experiment is controlled from one PC that runs the genetic programming code "glyph" and a LabView program that handles communication with all involved components of the slow learning loop. The genetic programming code provides new generations of individuals based on the evolutionary process described in section 2.2.1. Each new generation is sent to the LabView program through the zeroMQ network interface. The LabView program then sends the control laws of single individuals to the FPGA controller through a FIFO stream where they are tested in the fast control loop for a chosen test period. During the test period, all sensor signals used in the fast control loop and actuation signals are sent by FIFO stream to a data logging VI running on the real time controller before they are passed on to the LabView program on the PC through a network stream. Furthermore the wake pressure data, acquired during the test period of one control law is sent to the PC via network communication with the pressure measurement system. The time averaged wake pressure distribution is used to calculate the drag coefficient achieved with the tested control law, calculated by a MatLab script implementing the method described in section 2.1. The fitness value for the tested individual is calculated from the drag coefficient and the duty cycle based on logged actuation data. Once all individuals of one generation have been tested, their fitness values are returned to the genetic programming code through zeroMQ and "glyph" sends the the next generation.

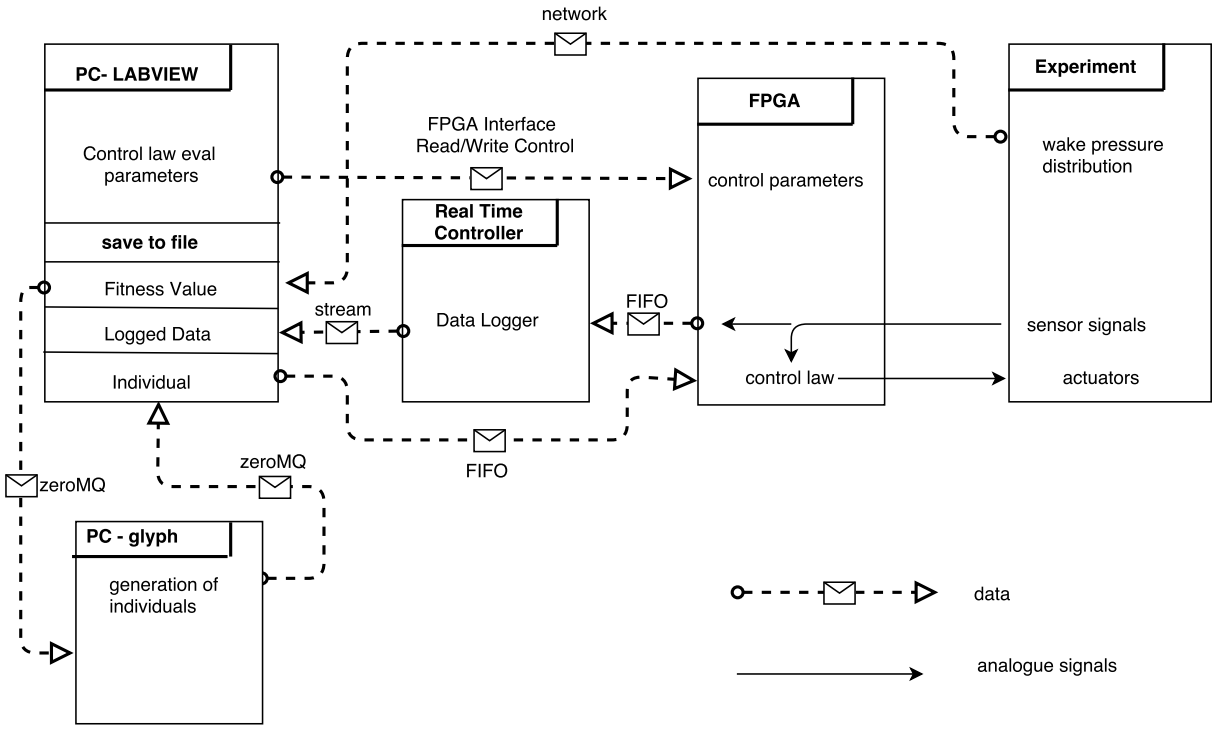

Figure 3.7: MLC infrastructure and communication

3.5 Test cases

This section summarizes all test cases that are investigated experimentally from the base configuration to closed loop machine learning experiments.

The base configuration and all passive trailing edge flaps are tested at different Reynold numbers in a range of 46000 to 71000. For all those tests the small rake is used and traversed vertically in 5 positions. Pressure data for each position is averaged over a 10 seconds at 100 Hz measurement frequency.

Open loop experiments are undertaken with attached Coanda flap for tank pressures of 1 bar, 2 bar and 4 bar. For each pressure a range of frequencies from 5 Hz to 100 Hz and duty cycles from 0 % to 100 % is tested. All open loop experiments are undertaken at a Reynolds number of 50000. The wake pressure distribution is measured with the wide rake in a single position and the pressure data is averaged over 10 seconds at 100 Hz measurement frequency.

Four MLC experiments are run at a Reynolds number of 50000 and a 4 bar tank pressure of 4 bar. The wake pressure distribution is measured with the wide rake in a single position and the pressure data is averaged over 5 seconds at 100 Hz measurement frequency. Their common MLC parameters are given in table 3.1. The operands MLC is given to build trees are addition, subtraction, multiplication and division. MLC is further given access to all sensors and derived features. An internal penalization of complexity of the control laws is activated as suggested by Duriez et al. [9] to prevent over-fitting. In the four runs all combinations of single- / multi-objective optimization and actuation of the slots by a single or two separate control laws are investigated.

Parameter	**Meaning**	**Value**
N_i	population size	40
N_g	number of generations	20
P_r	replication probability	0.1
P_c	crossover probability	0.6
P_m	mutation probability	0.3
N_p	tournament size	4
N_e	number of elite individuals	1

Table 3.1: Common MLC parameters for four experimental runs

Chapter 4

Results

4.1 Base configuration

Measurements with the model in the base configuration have been made to provide a reference value to compare the performance of all drag reduction methods to. Furthermore the measured drag in the base configuration can be compared to the drag measured in other experiments to confirm that the experimental setup is fine and the drag evaluation method is working properly. Table 4.1 shows all drag coefficients measured during this experiment and measured by Pastoor et al [24] for a similar model.

Reynolds number	**current C_D**	**Pastoor et al [24] C_D**
23000	-	0.89
35000	-	0.92
46000	0.86	0.89
50000	0.86	-
54000	0.87	-
58000	-	0.90
66000	0.85	-
70000	-	0.91

Table 4.1: Drag coefficients for the base configuration measured by current experiments and Pastoor et al [24] for a range of Reynolds numbers from $2.3 \cdot 10^4$ to $7.0 \cdot 10^4$

The measurements show good consistency in the drag coefficient values and the change of C_D with Re. In both experiments there is no clear dependency of the drag on the Reynolds number. This is similar to the behaviour of other bluff bodies like cylinders or vertical flat plates in the same Reynolds number regime and indicates that the separation points are not moving with an increasing Reynolds number, as it can be expected for blunt based bodies with sharp trailing edges. The difference between the mean drag coefficients over all Reynolds numbers is less than 5 %.

The wake pressure distribution at $Re = 4.6 \cdot 10^4$ can be seen in figure 4.1. The data points collected from five positions of the small rake show a clear pressure deficit in the wake for the total and static pressure. The fitted curves match the original data very well.

Figure 4.2 shows the pressure distribution measured by pressure taps on the model's surface at $Re = 4.6 \cdot 10^4$. The pressure values of the upper and lower side show a good agreement, confirming that the model was oriented completely horizontally. Pressure taps at the stagnation point correctly show a pressure coefficient of about one. The pressure distribution of taps around

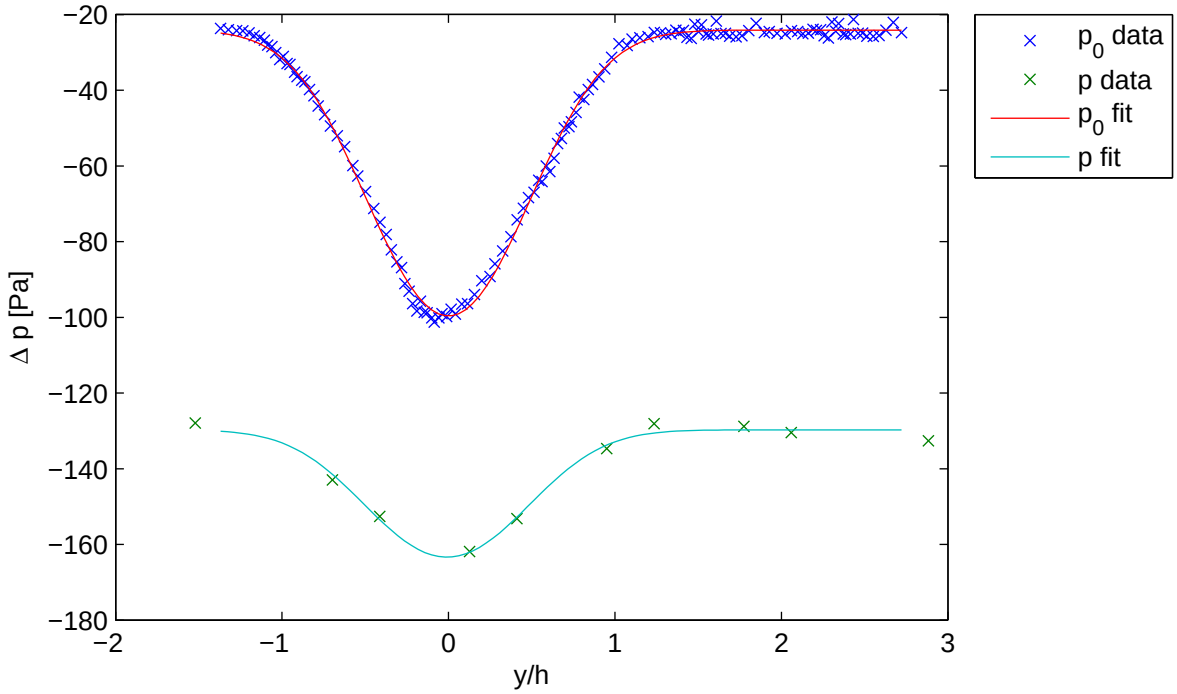

Figure 4.1: Wake pressure distribution for the base configuration at $Re = 4.6 \cdot 10^4$

the nose show an acceleration of the flow. Farther downstream the pressure coefficient settles close to a value of $C_p = 0.5$.

Table 4.2 shows the drag coefficients determined by experiment and RANS simulations of the base configuration conducted by Stollenwerk [27]. The measured drag is higher than in the RANS results. The lower drag coefficient in the RANS simulations can be explained by RANS simulations averaging over time and therefore underestimating the impact of unsteady vortex shedding. However the drag reductions between different configurations in experiment and simulation are of higher interest than the drag coefficient for a single experiments. The base configuration results set reference for further comparison.

	experiment	**RANS**
C_d base configuration	0.859	0.674

Table 4.2: Comparison of drag coefficients determined by experiment and RANS simulation at $Re = 5.35 \cdot 10^4$

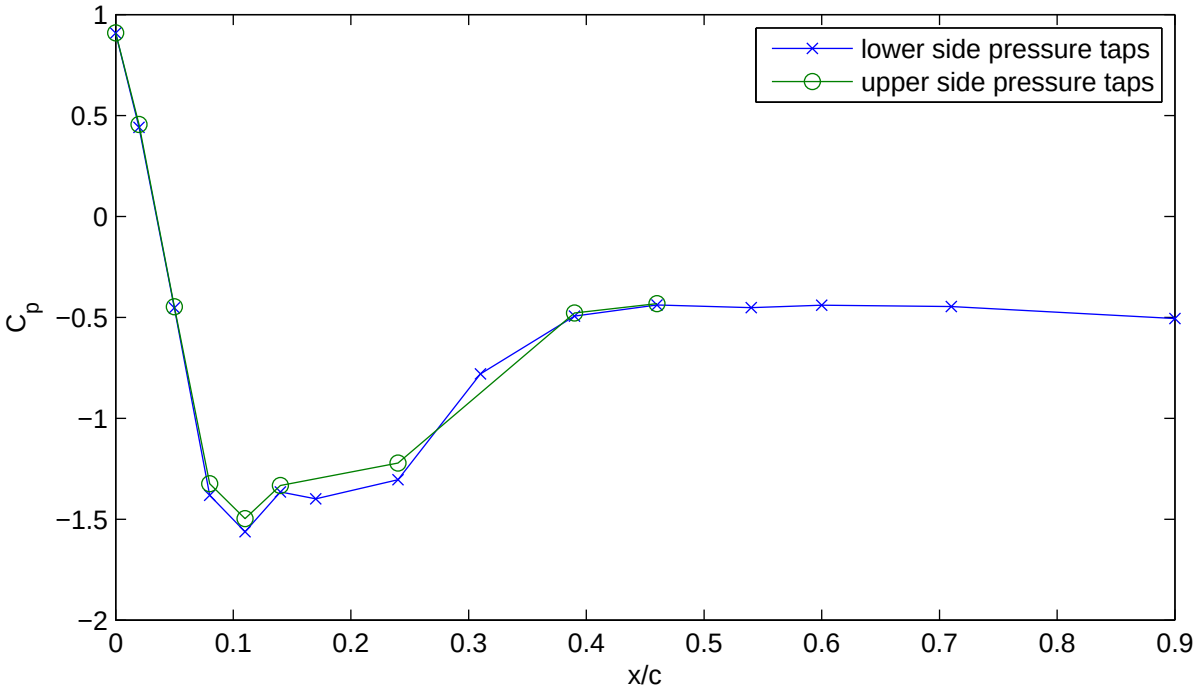

Figure 4.2: Surface pressure distribution measured by pressure taps on model in base configuration at $Re = 4.6 \cdot 10^4$

4.2 Passive drag reduction

Tests with passive drag reducing flaps have been undertaken with four different flap geometries at different Reynolds numbers. A summary of the results is presented in table 4.3. All flaps are successful in reducing the drag coefficient. The highest drag reduction was measured with the optimal tangent flaps. It seems physically sensible that a tangent connection between body and flap is advantageous. The flaps with optimal free geometry consequently performed slightly worse. As expected, both linear shapes perform worse than the optimized shapes. The drag coefficient achieved with the linear steep flap however are surprisingly close to those achieved with the optimal free flap.

Unlike the base configuration, the model with attached flaps shows a dependency of the drag coefficient on the Reynolds number. This dependency is very clear for all flap geometries except for the low angle, straight flap "linear flat", for which a decrease in drag for higher Reynolds numbers has been observed but it is too low to conclude a clear dependency. As the change of drag coefficient with the Reynolds number is introduced by the addition of flaps, it has to be connected to a change in the flow over the flaps. With increasing Reynolds number the turbulent boundary layer is becoming thinner and more energetic. It can therefore withstand higher adverse pressure gradients without separating. This means that the flow over the flaps likely stays attached longer for a higher Reynolds number, making the flaps more effective and further decreasing the drag coefficient. This is supported by an increase in the base pressure coefficient with increasing Reynolds number shown in figure 4.3 for the example of the optimal tangent flap geometry.

Figure 4.4 shows the distributions of total and static pressure in the wake of the model in base configuration and equipped with the optimal tangent flap at $Re = 4.6 \cdot 10^4$. One can see that total as well as static pressure in the wake are increased by addition of the flaps. Furthermore the flaps cause the deficit in total and static pressure in the wake to become more narrow. This indicates

	Re	C_D	drag reduction
linear flat	46000	0.706	18 %
	65000	0.704	18 %
linear steep	46000	0.603	30 %
	65000	0.571	34 %
optimal free	46000	0.591	31 %
	50000	0.569	34 %
	53000	0.554	36 %
	65000	0.553	36 %
	71000	0.541	37 %
optimal tangent	46000	0.576	33 %
	50000	0.570	34 %
	53000	0.556	35 %
	65000	0.515	40 %
	71000	0.515	40 %

Table 4.3: Drag coefficients with different passive drag reducing flaps for a range of Reynolds numbers from $4.6 \cdot 10^4$ to $7.1 \cdot 10^4$

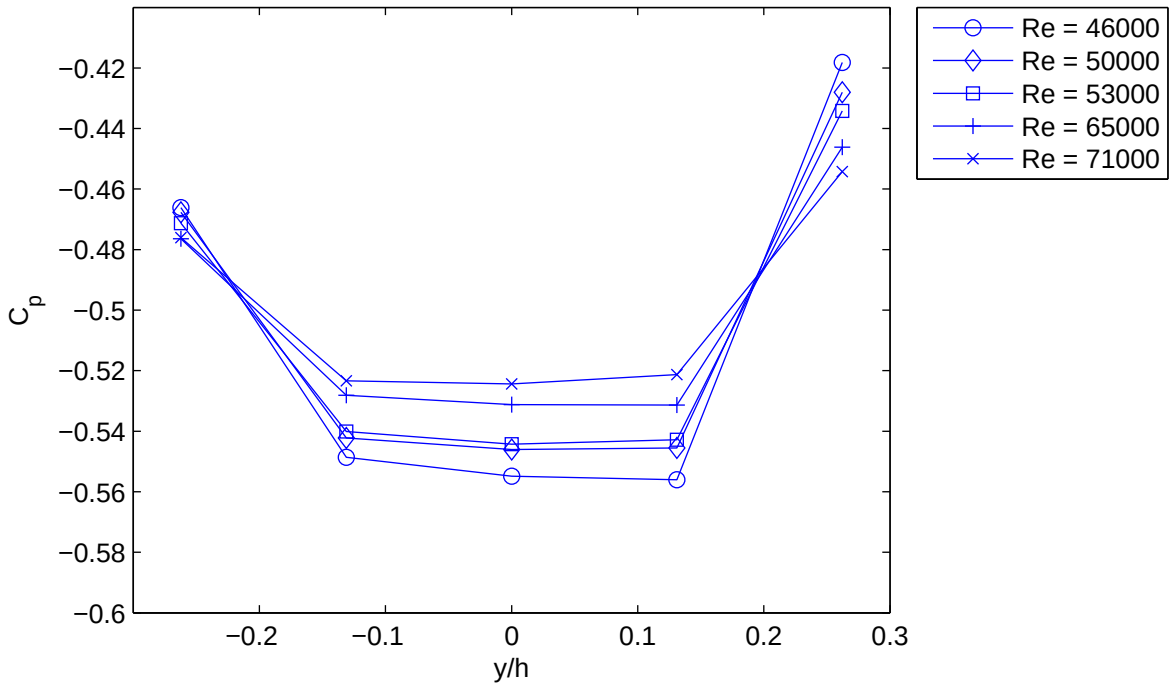

Figure 4.3: Distributions of the pressure coefficient over the model base with optimal tangent flap geometry at different Reynolds numbers

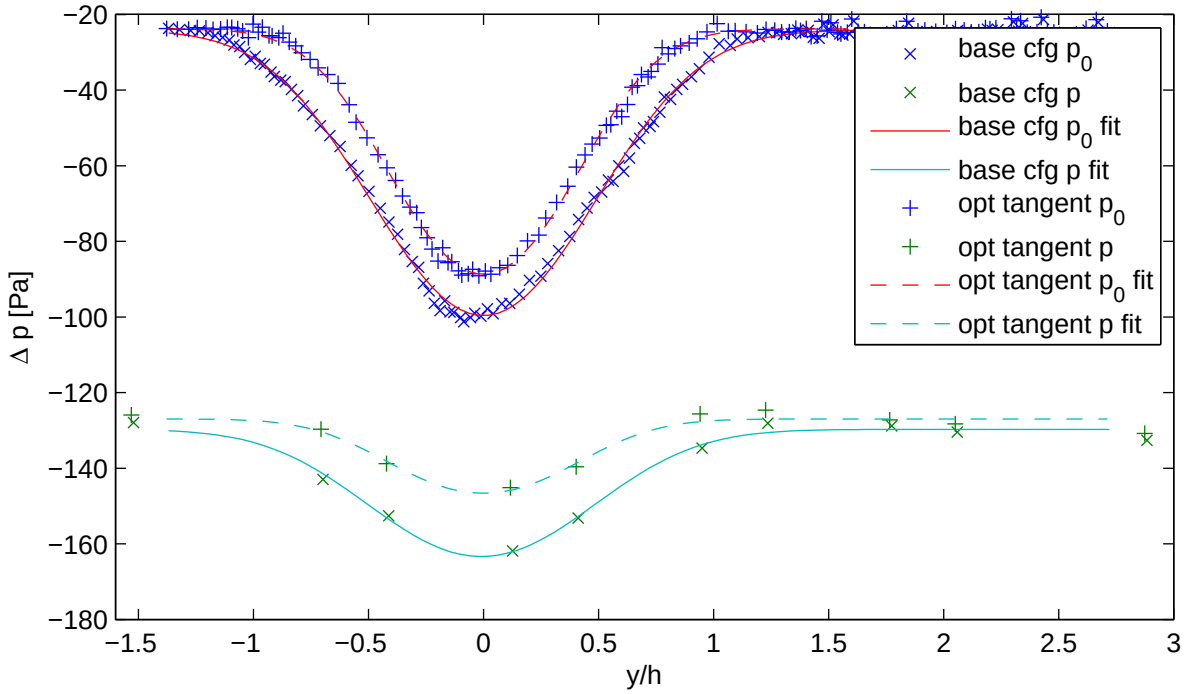

Figure 4.4: Distributions of total and static pressure in the wake of the model in base configuration and with the optimal tangent flap at $Re = 4.6 \cdot 10^4$

a lower momentum deficit and pressure loss in the wake, consequently leading to a smaller drag coefficient. Similar effects are visible for all flap geometries. Figure 4.5 shows the distributions of the pressure coefficient over the model base for the base configuration and all passive flap geometries at $Re = 4.6 \cdot 10^4$. The flap geometries yielding the lowest drag coefficients also show the highest base pressure levels. This trend is consistent with the increase of the pressure level in the wake.

Figure 4.6 shows stream lines and the pressure coefficient field obtained from RANS simulations for the "optimal free" flap geometry and the base configuration at $Re = 5.35 \cdot 10^4$ performed by Stollenwerk [27]. The simulation results match with the observations that the addition of the flap causes a narrower pressure deficit in the wake and higher pressures at the model base and in the wake. The base pressure levels visible in the simulation results are higher than the measured values. Consequently, the RANS simulation results yielded lower drag coefficients than the experiments. A comparison of the achieved drag coefficients is given in table 4.4.

	experiment	**RANS**
C_d base configuration	0.859	0.674
C_d optimal free	0.554	0.395
drag reduction	36 %	41 %

Table 4.4: Comparison of drag coefficients and drag reduction achieved by passive with passive devices, determined by experiment and RANS simulation at $Re = 5.35 \cdot 10^4$

The experimentally determined drag reduction for the optimal free flap shape is lower but close to the drag reduction determined by RANS simulations at the same Reynolds number. The good match between the drag reduction in the RANS simulations and the experiments indicates that the RANS simulation correctly model the significant drag reduction mechanisms for passive flaps.

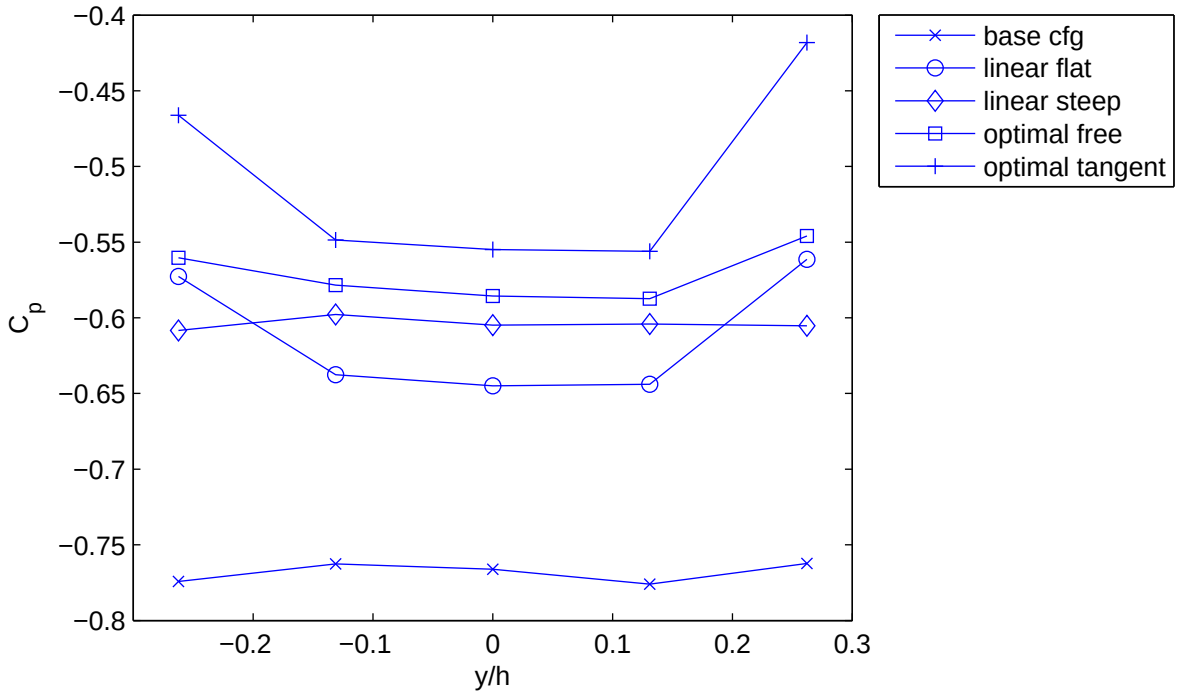

Figure 4.5: Distributions of the pressure coefficient over the model base for the base configuration and all passive flap geometries at $Re = 4.6 \cdot 10^4$

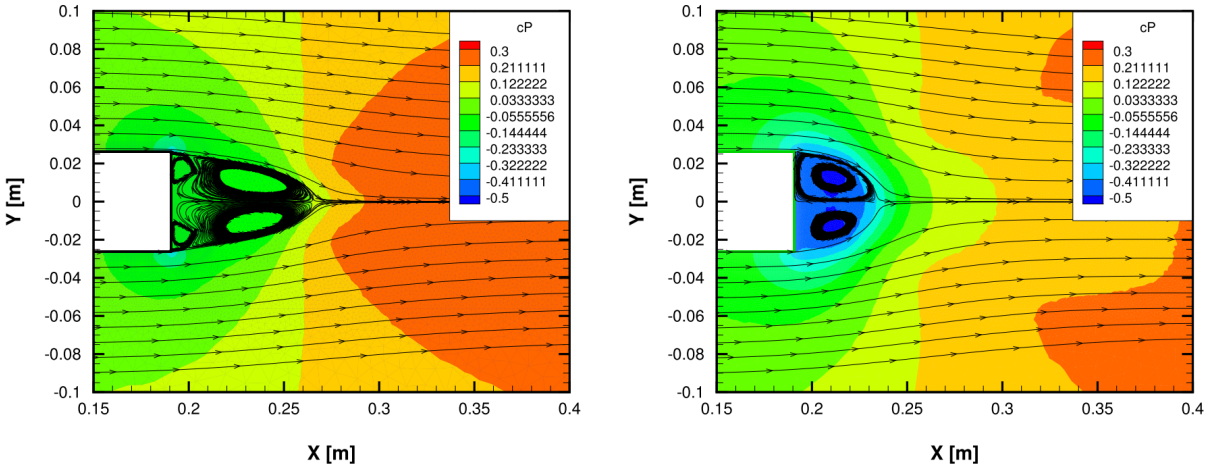

(a) (b)

Figure 4.6: Stream lines and pressure coefficient field obtained from RANS simulations for the "optimal free" flap geometry (a) and the base configuration (b) at $Re = 5.35 \cdot 10^4$, taken from Stollenwerk [27]

4.3 Open loop control

Open loop control experiments are conducted to investigate the drag reduction that can be achieved with Coanda blowing at fixed frequencies and duty cycles. Furthermore different tank pressures are tested to investigate the influence of different jet velocities on the drag reduction. All experiments were conducted at $Re = 5.0{\cdot}10^4$ with both blowing slots actuated simultaneously. The results are presented as contour plots in figure 4.7 for one bar tank pressure, figure 4.8 for two bar tank pressure and figure 4.9 for four bar tank pressure. Each figure shows the measured drag coefficients for a blowing frequency range of 5 Hz to 100 Hz and a duty cycle range from 0 % to 100 %. Independent of the the frequency, 0 % duty cycle means no blowing and 100 % duty cycle means constant blowing.

All three figures show a strong, non-linear dependency of the drag on the blowing frequency. Blowing at certain frequencies shows to have a detrimental effect for drag reductions. This is particularly clear for a frequency of about 70 Hz, corresponding to the natural vortex shedding frequency under the given test conditions or a Strouhal number of 0.23. For the one and two bar tank pressure cases, blowing at the natural vortex shedding frequency and with a duty cycle of about 30 % to 40 % even increases the drag coefficient over that of the model without blowing. For the four bar tank pressure case the drag is also particularly high at 70 Hz but it doesn't exceed the drag without blowing as the momentum added to the flow by blowing starts to become more significant. The highest drag for the four bar tank pressure experiments is found at a blowing frequency of 33 Hz which is close to a sub-harmonic of the natrual vortex shedding frequency.

A detrimental effect of blowing at the natural vortex shedding frequency has also been observed by Henning [15] in open loop control experiments on a D-shaped bluff body. The effect can be explained with blowing at the vortex shedding frequency strengthening the vortex shedding process that causes high pressure loss in the near wake. This explanation is further supported by Henning's findings that blowing at the natural vortex shedding frequency with a 180 degree phase shift between the upper and lower slot increases the drag even more.

For all tank pressures, the lowest drag values can be found at frequencies above the natural vortex shedding frequency. For one and two bar tank pressure the drag minima occur at frequencies of about 77 Hz, just slightly above the natural vortex shedding frequency and duty cycles of 40 % and 70 % respectively. However, similarly low drag coefficients can be seen at higher frequencies of up to 100 Hz also. For four bar tank pressure, the lowest drag coefficient is found at a frequency of 100 Hz and 50 % duty cycle.

The impact of the duty cycle on the drag coefficient is very diverse. Regions of particularly high or low drag coefficients that appear around the extrema in the contour plots are limited to a narrow spans of duty cycles. Effective influence on the flow structure appears to work only at certain combinations of frequencies and duty cycles. Apart from the extrema, higher duty cycles generally yield lower drag for the two and four bar tank pressure experiments. This can be attributed to more momentum being added to the flow. Especially at low frequencies a low duty cycle also means that the flow is completely undisturbed by actuation for a longer timespan. For the one bar tank pressure experiment, no clear trend is visible for the impact of higher duty cycles. The momentum and disturbance introduced to the flow might be too low to have a significant impact on drag when no interference with the natural flow dynamics is achieved.

Figure 4.10 shows the distributions of total and static pressures in the wake of the model with attached Coanda flaps, without blowing and with the Coanda blowing configuration that yields the lowest drag coefficient at $Re = 5.0 \cdot 10^4$. With actuation the total pressure deficit in the wake becomes narrower and less intense. The deficit in static pressure is reduced so drastically that it almost disappears. This shows a narrower, more energetic wake with a lower pressure loss. Comparison with figure 4.11 shows that the pressure increase in the wake is not just a result

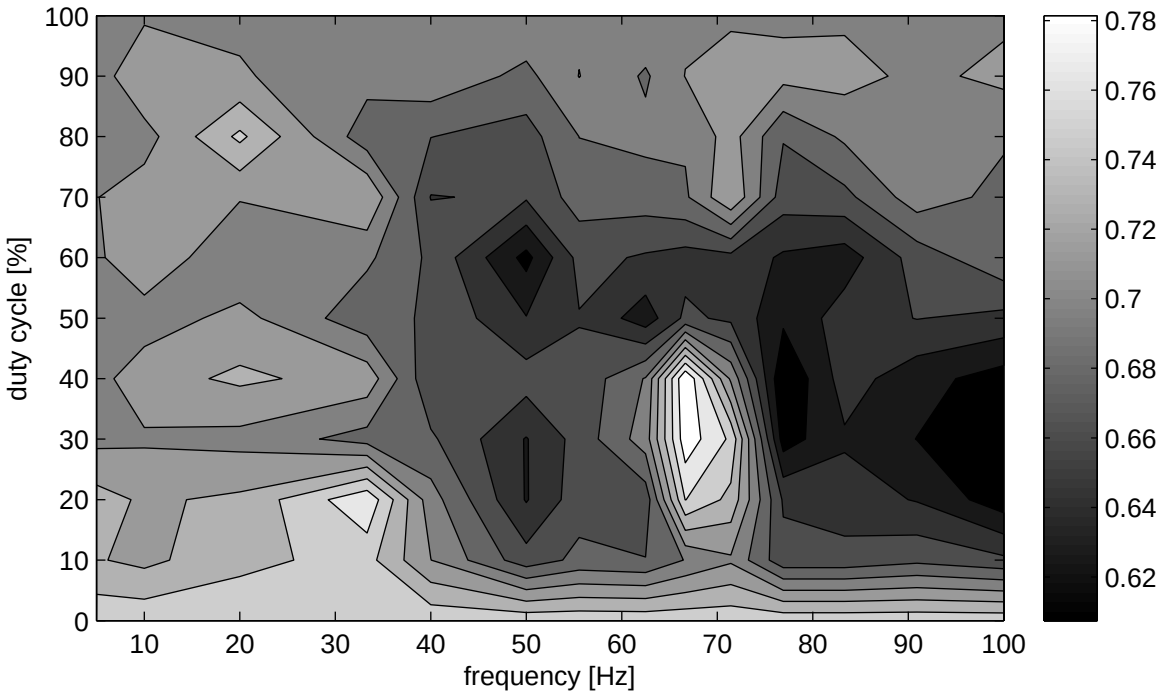

Figure 4.7: Drag coefficient over frequency and duty cycle, 1bar tank pressure

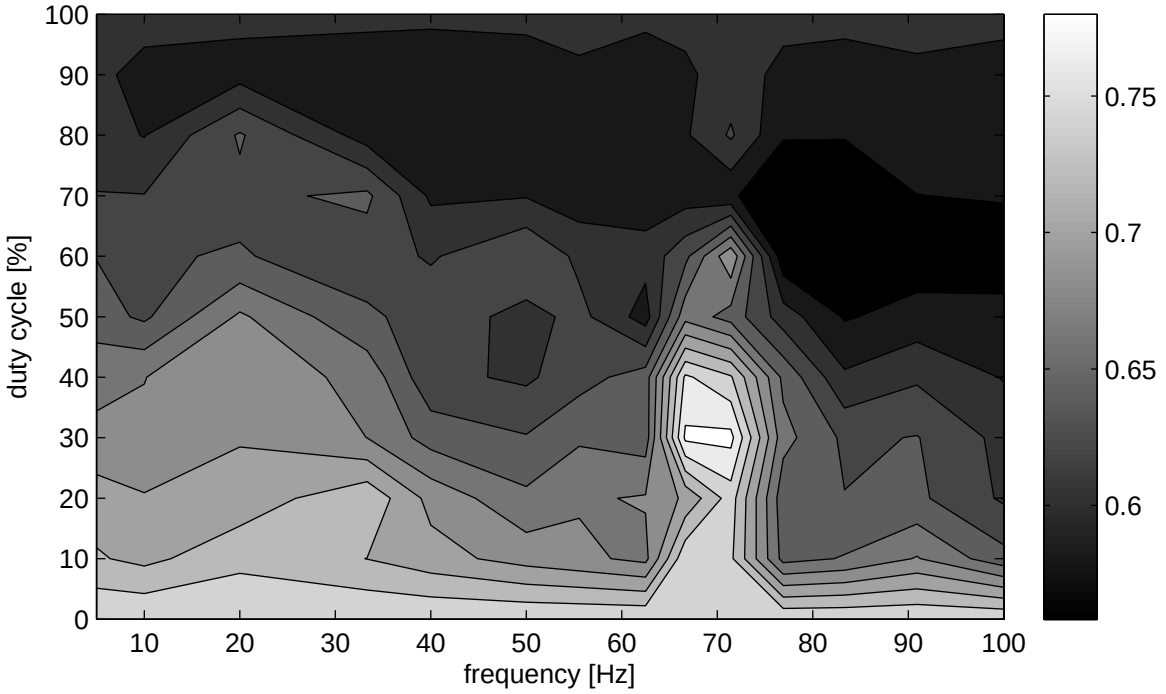

Figure 4.8: Drag coefficient over frequency and duty cycle, 2 bar tank pressure

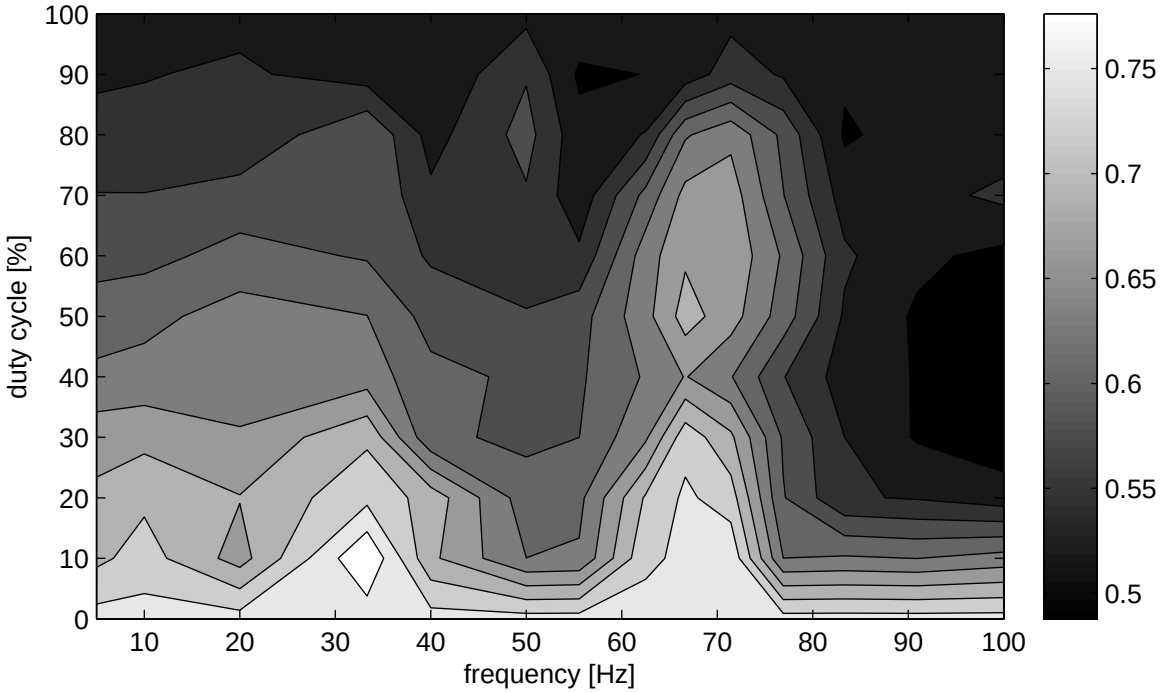

Figure 4.9: Drag coefficient over frequency and duty cycle, 4 bar tank pressure

	frequency [Hz]	**duty cycle [%]**	C_d	**drag reduction [%]**
no blowing base config	-	0	0.859	0
no blowing Coanda flaps	-	0	0.759	12
const blowing 1 bar	-	100	0.709	17
Min C_d 1 bar	76.9	40	0.601	30
Max C_d 1 bar	66.7	40	0.799	7
const blowing 2 bar	-	100	0.605	30
Min C_d 2 bar	76.9	70	0.558	35
Max C_d 2 bar	71.4	30	0.786	9
const blowing 4 bar	-	100	0.537	37
Min C_d 4 bar	100	50	0.488	43
Max C_d 4 bar	33.3	10	0.805	6

Table 4.5: Summary of open loop control Coanda blowing experimental results at $Re = 5.0 \cdot 10^4$

of more air being blown into the wake but a beneficial interference with natural flow process attenuating vortex formation. Figure 4.11 shows a comparison of the pressure distributions in the wake of the model with attached Coanda flaps, without blowing and with the Coanda blowing configuration that yields the highest drag coefficient. Despite the Coanda jets injecting momentum and pressure into the wake, the distribution of total pressure shows a wider and deeper deficit for the actuated case. The distribution of static pressure is comparable between the non-actuated and actuated case. Adding momentum to the flow appears to decrease the momentum in the wake, indicating an amplification of flow processes that increase drag and therefore loss of momentum, like vortex shedding.

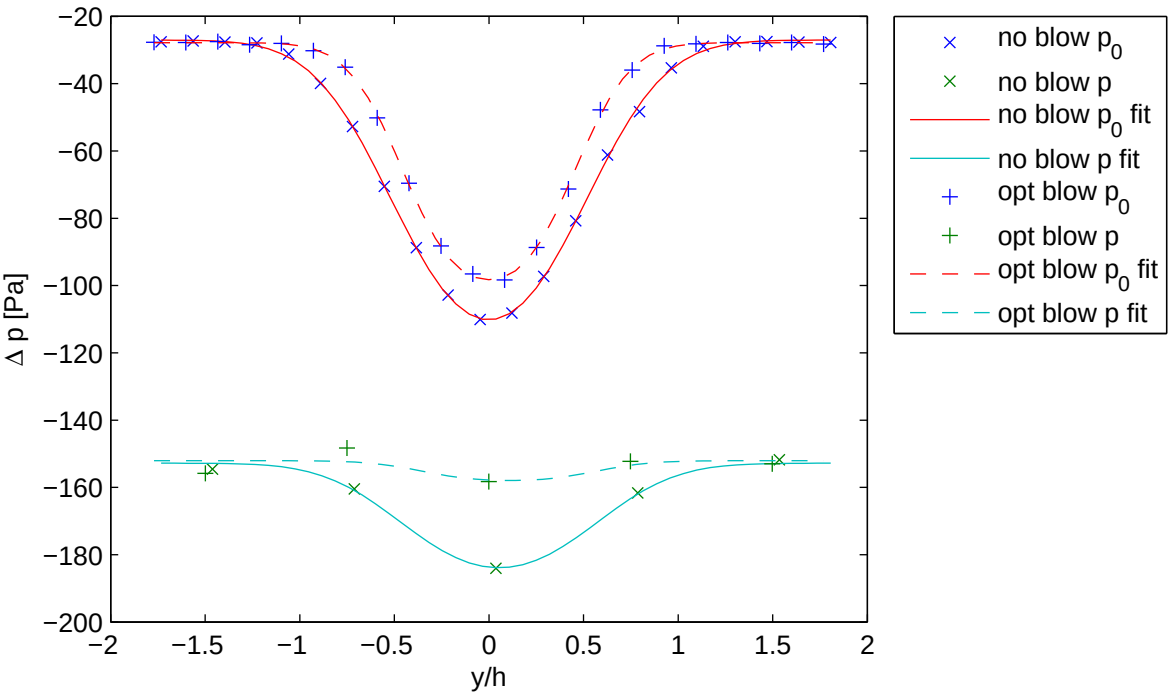

Figure 4.10: Comparison of pressure distributions in the wake of the model with attached Coanda flaps, without blowing and with Coanda blowing at 100 Hz and 50 % duty cycle at 4 bar tank pressure, yielding the lowest drag coefficient at $Re = 5.0 \cdot 10^4$

It is worth noting that blowing at fixed frequencies yields lower drag coefficients than constant blowing. The attenuation of vortex shedding appears to be stronger through intermittent blowing. This attenuating effect also appears to outweigh the higher momentum added to the flow by constant blowing. In conclusion, blowing at the right frequencies is more efficient than constant blowing, as higher drag reduction is achieved at lower cost of actuation energy. Blowing at the wrong frequency however has detrimental effects. The range of beneficial and detrimental frequencies depends on the natural vortex shedding frequency and the therefore on the flow conditions.

The experimental results for constant blowing can also be compared to the result of the simulations based on which the shape of the Coanda flap was determined. Drag reductions predicted by the simulations are significantly higher than what could actually be achieved in the experiment. The drag reduction observed in the experiments can not be confirmed by the experiments. Inaccuracies in the simulation as well as imperfections on the model could be responsible for the difference. On one hand two-dimensional RANS simulations are known to have a limited accuracy and a drag reduction of 82 % appears to be very high. On the other hand, different deviations of the real world model from the idealized simulation model could cause a lower performance. Possible sources for deviations are, manufacturing inaccuracies of the the Coanda flaps,

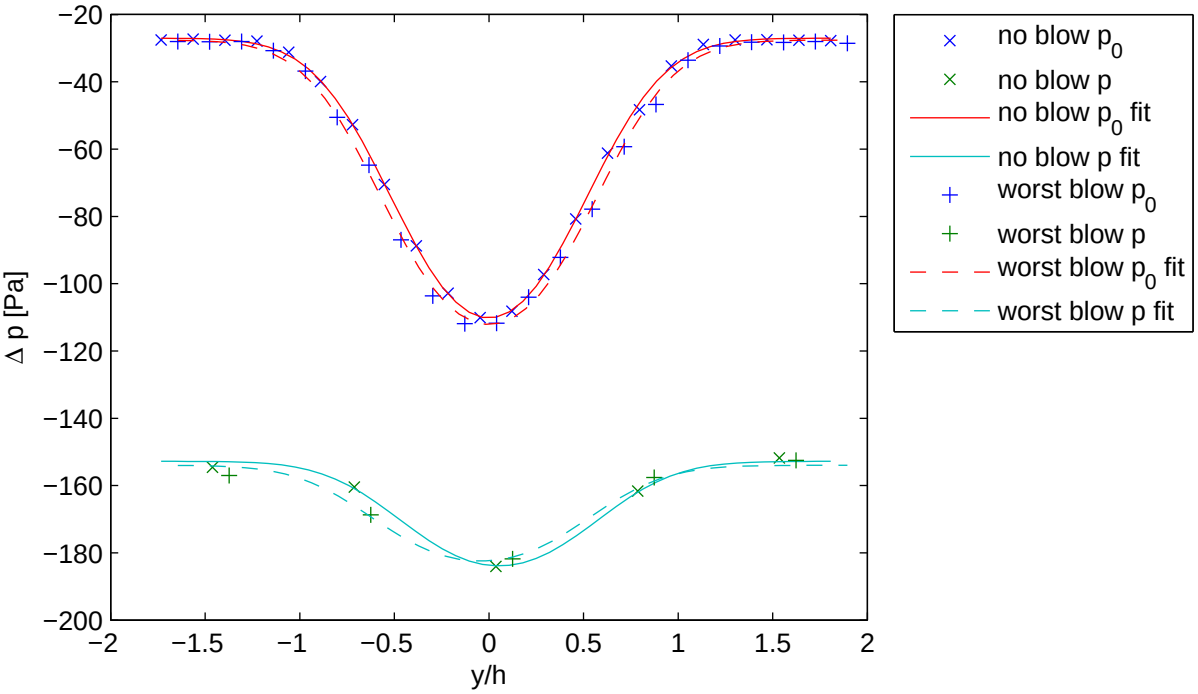

Figure 4.11: Comparison of pressure distributions in the wake of the model with attached Coanda flaps, without blowing and with Coanda blowing at 33.3 Hz and 10 % duty cycle at 4 bar tank pressure, yielding the highest drag coefficient at $Re = 5.0 \cdot 10^4$

the remaining degree of surface roughness after polishing of the flaps or small shape deviations introduced by sanding the flaps. As the attachment of the flow to the Coanda surfaces is sensitive to perturbations this could cause early too early flow separation and reduce the effecitveness of the flaps.

	experiment	**RANS**
C_d base configuration	0.859	0.674
C_d Coanda blowing	0.537	0.12
drag reduction	37 %	82 %

Table 4.6: Comparison of drag coefficients and drag reduction achieved by constant Coanda blowing, determined by experiment at $Re = 5.0 \cdot 10^4$ and RANS simulations at $Re = 5.35 \cdot 10^4$

4.4 Closed loop control

4.4.1 Genetic optimization convergence

4.4.1.1 Single objective single output

An initial MLC run has been undertaken with a single cost function combining the drag coefficient and duty cycle as described in section 2.2.3 and synchronized blowing from both slots based on a single actuation signal. Figure 4.12 shows the progression of the cost function values of the best five individuals of each generation over 20 new generations. The progression of the best value

that has been found up to a certain generation is shown as red line labelled "best". The initial generation is labelled as 0th generation.

The best cost function value initially improves but stagnates after the second generation. No better individual is found afterwards. This means that a global optimum is found earlier compared to separation control experiments by Debien et al. [8] where an optimum was reached after about 4 generations and mixing layer experiments by Gautier et al. [11] where an optimum was reached after about 7 generations. As very simple control laws have been found to perform surprisingly well throughout the experiments on the D-shaped body, it its possible that these have been found early in this experiment. The initial population did likely contain very good individuals already. Finding an even better individual than the best in generation two would have taken more generations or a larger population size or might not be feasible with this experimental setup.

From generation 9 onwards, a wider spread in the cost function values can be observed. Mutation and crossover operations with suboptimal individuals can move good individuals away form any optima temporarily. However, through elitism, the current global minimum is preserved and MLC's exploitation mechanisms can drive individuals back towards it.

Figure 4.13 shows a Pareto plot of all tested individuals. Even though MLC was used to optimize a single combined objective function here, it is interesting to observe the distribution of in individuals in a space spanned by the duty cycle and drag coefficient. The performances of all individuals tested throughout the evolutions are marked by crosses. The initial generation is emphasized by red colour. The green line is an isoline for the combined single objective cost based on a weighting factor $\gamma = 0.25$. All individuals on the isoline have the same cost while the biggest change in cost can be found in perpendicular direction. The isoline is put into the Pareto plot to pass through the best individual. The high density of individuals close to the best one shows how MLC exploited the found minima and tried to push the Pareto front forward on one corner that is favourable for the given weight.

The comparison between the best individual of the initial generation, the overall best individual of this experiment and the best open loop actuation, see table 4.7, shows that the best individual reach comparable performance to the best open loop case and that the initial generation contained well performing individuals already. Similar performance between a best open loop case and the MLC results have also been observed by Debien et al. [8], Gautier et al. [11] and Parezanović et al. [23].

	C_D	α	J
best gen 0	0.507	0.424	0.613
best gen 0 to 20	0.499	0.412	0.602
best open loop	0.488	0.50	0.613

Table 4.7: Comparison of the performance of the best individuals of the first generation and over all generations with the best open loop for a single objective single output MLC run

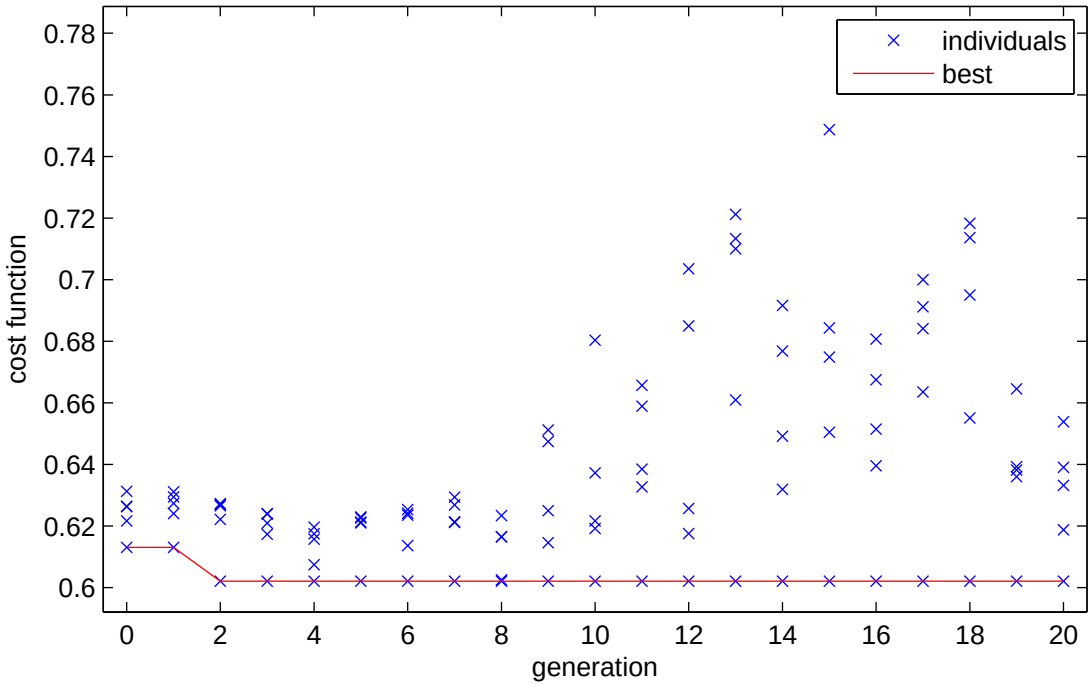

Figure 4.12: Progression of the cost function values for the best five individuals of each generation over 20 new generations and a cost function $J = C_D + 0.25 * \alpha$, optimized with respect to a single objective and synchronised actuation by a single control law

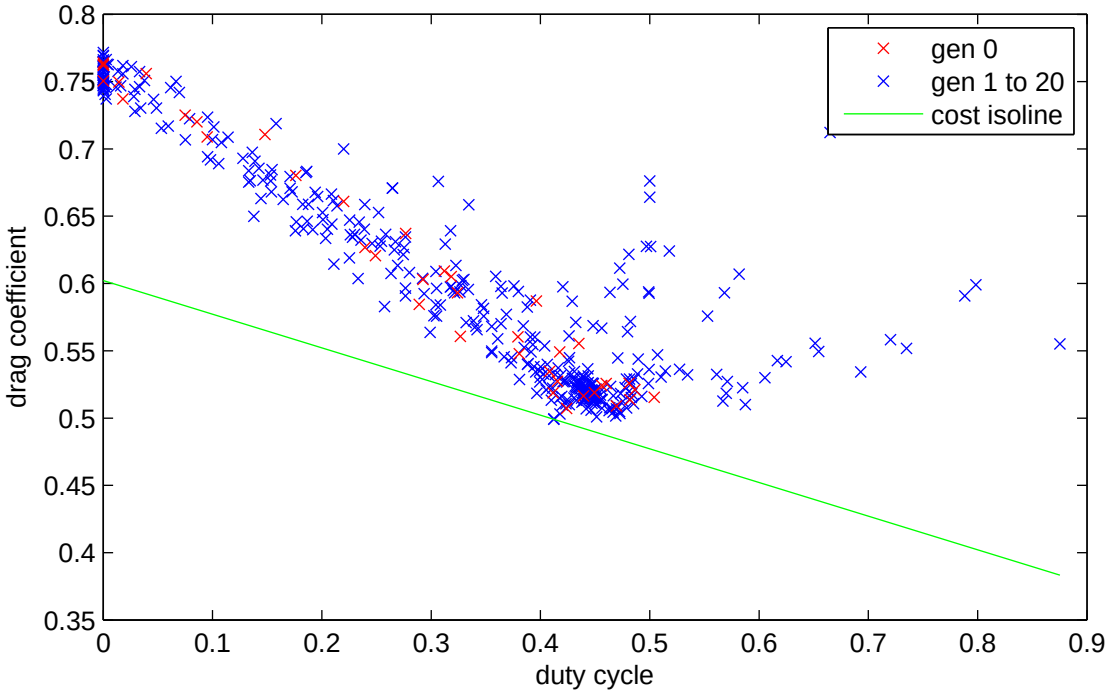

Figure 4.13: Pareto plot for all tested individuals over 20 new generations and isoline for cost function $J = C_D + 0.25 * \alpha$, optimized with respect to a single objective and synchronised actuation by a single control law

4.4.1.2 Single objective multiple output

A second MLC experiment is undertaken with the same single objective cost function used in the previous section but two independent actuation signals, each controlling the blowing from either the upper or lower slot. This enables a much wider variety of control mechanisms as all possible combinations of two control laws can be used. Figure 4.14 shows the progression of the cost function values of the best five individuals of each generation over 20 new generations. The progression of the best value that has been found up to a certain generation is shown as red line labelled "best".

The most improvement in the cost function can be seen within the first two new generation, smaller improvements however can be seen up to the 15th generation. The optimum is found later than in the single output experiment. The higher degree of freedom complicates the search for an optimum but allows for more gradual improvement in the cost function. In the end, the cost values achieved with independent actuation of both blowing slots are slightly higher than with synchronized actuation.

Through the evolutionary process some fluctuation can be seen in the cost function values of the best five individuals of each generation. As seen before, mutation and crossover operations with suboptimal individuals can move good individuals away form any optima temporarily. However, through elitism, the current global minimum is preserved and MLC's exploitation mechanisms can drive individuals back towards it.

Figure 4.15 shows a Pareto plot of all tested individuals. MLC was still used to optimize a single combined objective function but again it is interesting to observe the distribution of in individuals in a space spanned by the duty cycle and drag coefficient. The marking is in accordance with the previously described Pareto plot and the cost isoline is based on the same weighting factor $\gamma = 0.25$. The distribution shows a clustering of individuals near the global optimum where the isoline meets the Pareto front. This shows how MLC further exploited the minima found by an initial individual close by.

The comparison between the best individual of the initial generation, the overall best individual of this experiment and the best open loop actuation, see table 4.8, shows that the best individuals reach comparable performance to the best open loop case. Independent actuation of both slots performs slightly worse than synchronized actuation by a single control law.

	C_D	α	J
best gen 0	0.554	0.286	0.625
best gen 0 to 20	0.534	0.302	0.610
best open loop	0.488	0.50	0.613

Table 4.8: Comparison of the performance of the best individuals of the first generation and over all generations with the best open loop for a single objective multiple output MLC run

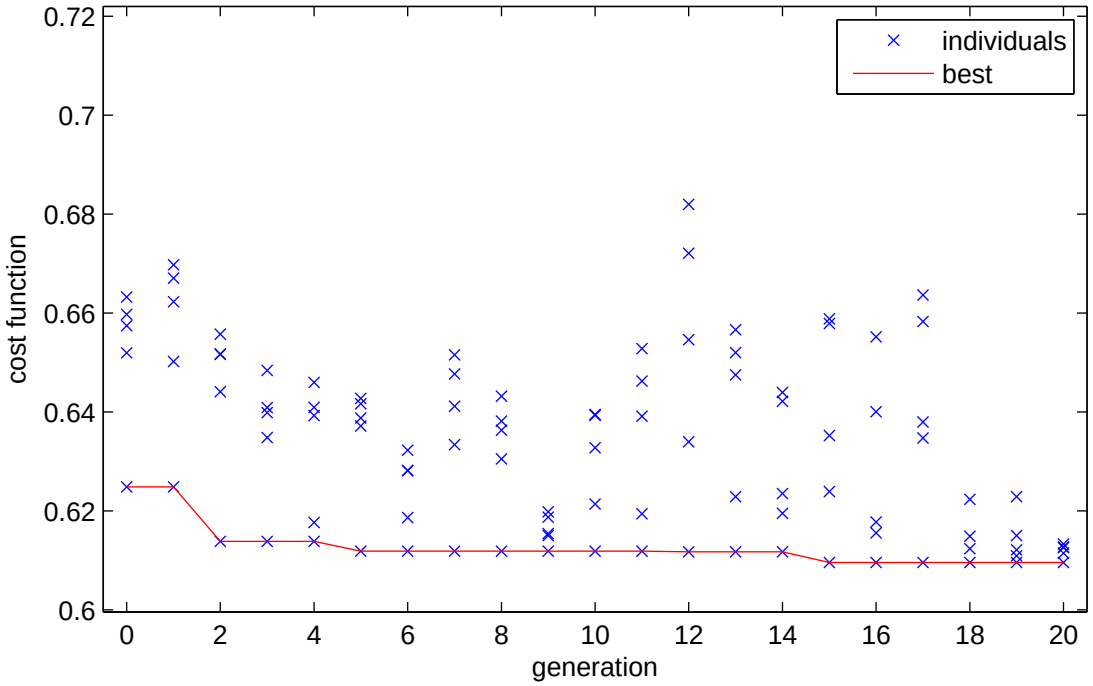

Figure 4.14: Progression of the cost function values for the best five individuals of each generation over 20 new generations and a cost function $J = C_D + 0.25 * \alpha$, optimized with respect to a single objective and independent actuation of both slots by a two control laws

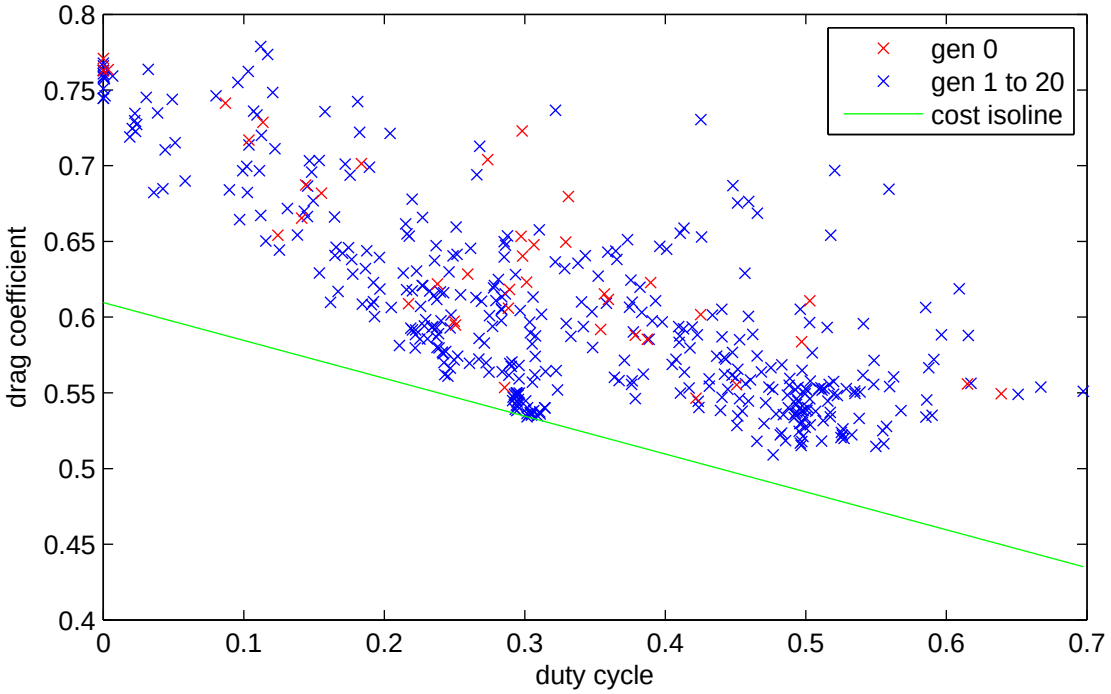

Figure 4.15: Pareto plot for all tested individuals over 20 new generations and isoline for cost function $J = C_D + 0.25 * \alpha$, optimized with respect to a single objective and independent actuation of both slots by a two control laws

4.4.1.3 Multi objective single output

As a third case, an MLC experiment is undertaken treating the drag coefficient and duty cycle as two separate cost functions for two objectives to be optimized and one single actuation signal controlling both blowing slots. This way no weighting between both objectives is necessary. However, as discussed in section 2.2.1 this also means that a single best individual is no longer defined. Convergence can therefore only be investigated by progression of the Pareto nondominated front.

Figure 4.16 shows the Pareto plot for a multi objective single output MLC experiment. Besides the performance of all tested individuals, the plot also shows the Pareto fronts formed by the initial population and the resulting front after 20 generations. In contrast to figure 4.13 the individuals stay distributed more evenly and no cluster forms. The Pareto front is moved forward almost entirely showing improvement for most Pareto optimal individuals. The fact that the final Pareto front is almost linear indicates that mechanisms with similar efficiency can be found working at different duty cycles The control laws are investigated in more detail in section 4.4.3.

As all individuals on the Pareto front are considered optima, there is not one best. For comparison with open loop results an individual on the lower end of the Pareto front is chosen. The drag coefficients, duty cycles and theoretical single objective cost values based on the previously used weighting are shown in table4.9. The closed loop control law achieves less than 1 % higher drag at about 18 % less actuation energy than the best closed loop actuation.

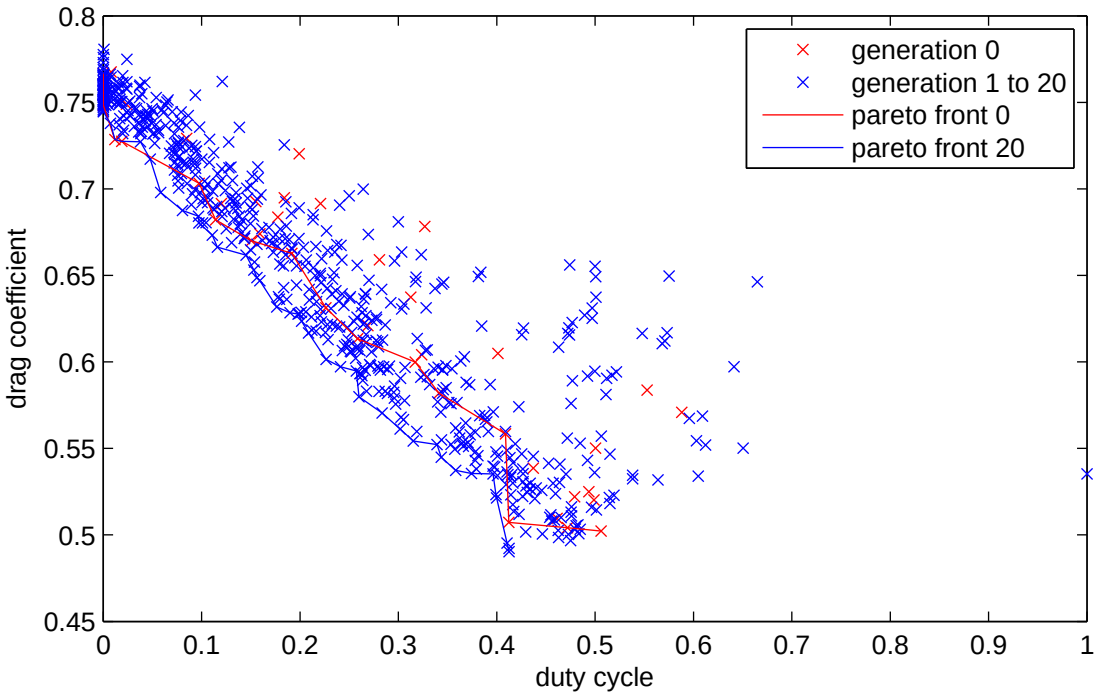

Figure 4.16: Pareto plot for all tested individuals over 20 new generations, optimized with respect to drag coefficient and duty cycle independently and synchronised actuation by a single control law

	C_D	α	J
pareto front individual	0.490	0.412	0.593
best open loop	0.488	0.50	0.613

Table 4.9: Comparison of the performance of a chosen Pareto front individual for a multi objective single output MLC run with the best open loop control

4.4.1.4 Multi objective multiple output

Experiments with drag coefficient and duty cycle as two separate cost functions for two objectives and two independent actuation signals, each controlling the blowing from either the upper or lower slot are undertaken as a fourth case. This setting gives MLC the highest freedom and lets it find good combinations of control laws implementing drag reduction mechanisms working with different duty cycles.

Figure 4.17 shows a Pareto plot of all tested individuals and the Pareto fronts formed by the initial and final populations. Like in figure 4.16 the individuals are distributed rather evenly along the Pareto front without dominant clusters in single corners. The final Pareto front shows improvement over the full length. Unlike in figure 4.16 the Pareto front is not linear but rather rounded, indicating that blowing mechanisms of different efficiencies are found. The control laws are investigated in more detail in section 4.4.3.

Table4.9 shows the drag coefficients, duty cycles and theoretical single objective cost values based on the previously used weighting for one individual on the final Pareto front and the best open loop actuation. The closed loop control law achieves less than 7 % higher drag at about 21 % less actuation energy than the best closed loop actuation. As for the single objective experiments, independent actuation of both slots performs slightly worse than synchronized actuation by a single control law.

	C_D	α	J
pareto front individual	0.522	0.396	0.621
best open loop	0.488	0.50	0.613

Table 4.10: Comparison of the performance of a chosen Pareto front individual for a multi objective multi output MLC run with the best open loop control

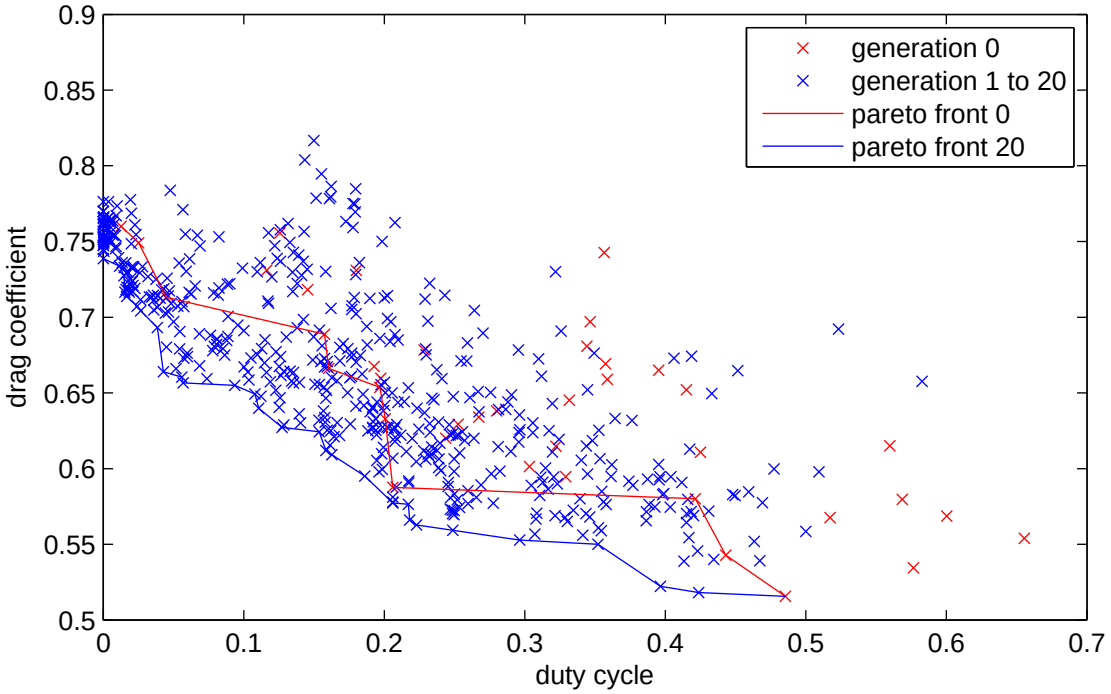

Figure 4.17: Pareto plot for all tested individuals over 20 new generations, optimized with respect to drag coefficient and duty cycle independently and independent actuation of both slots by a two control laws

4.4.2 Comparison of single- to multi-objective optimization results

When multiple objectives are to be optimized, multi-objective optimization is a generalization of single-objective optimization. When single-objective optimization is done using a weighted linear combination of the individual cost functions it finds an optimum for one specific weighting factor. Multi-objective optimization on the other hand finds multiple optima at the same time for a wide range of weighting factors. Single optima for arbitrary weighting factors can be chosen from the set of multi-objective optima subsequently.

The difference can be seen clearly in the Pareto plots also. When both objectives are optimized separately, MLC improves on all solutions along the Pareto front, considering the whole front as set of optimal solutions, as seen by the uniform distribution in figure 4.16. When a single objective is optimized, MLC attempts to improve solutions close to a single optimum on the Pareto front as seen by the clustering of individuals in figure 4.13. Figure 4.18 visualizes how different individuals on the Pareto front correspond to single objective optima with different weights. In return a different weight leads to a different individual on the Pareto front being considered as optimum. Graphically an optimum can be found by moving a cost isoline form the left towards the Pareto front and stopping once it passes through the first individual. The optimum chosen based on a specific weight is always a subset of all optima found by multi-objective optimization. It is worth noting that the cost isoline doesn't have to be tangent to the Pareto front in the optimum. The Pareto front is formed by a finite set of points and therefore neither continuous nor differentiable.

Figure 4.19 shows a Pareto plot of all individuals tested during a multi-objective single actuation output optimization run, the resulting Pareto front and a cost isoline through the optimum corresponding to a single objective cost function with weighting factor $\gamma = 0.25$. The resulting optimal individual is on the lower end of the Pareto front. This individual is compared to

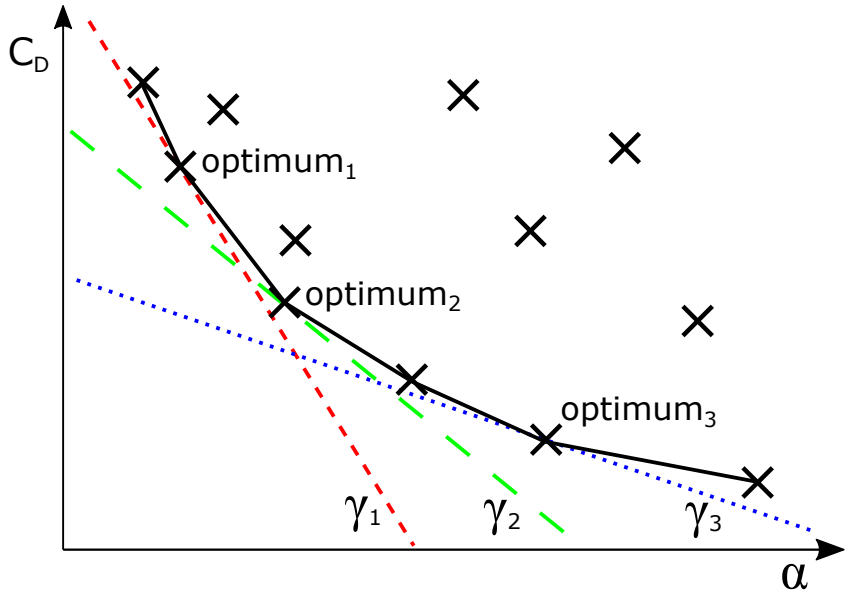

Figure 4.18: Exemplary Pareto plot for drag coefficient C_D and duty cycle α, showing the Pareto front, three cost isolines for different weighting factors ω for a single objective cost function $J = C_D + \omega \cdot \alpha$ and the corresponding optima on the Pareto front for each weight

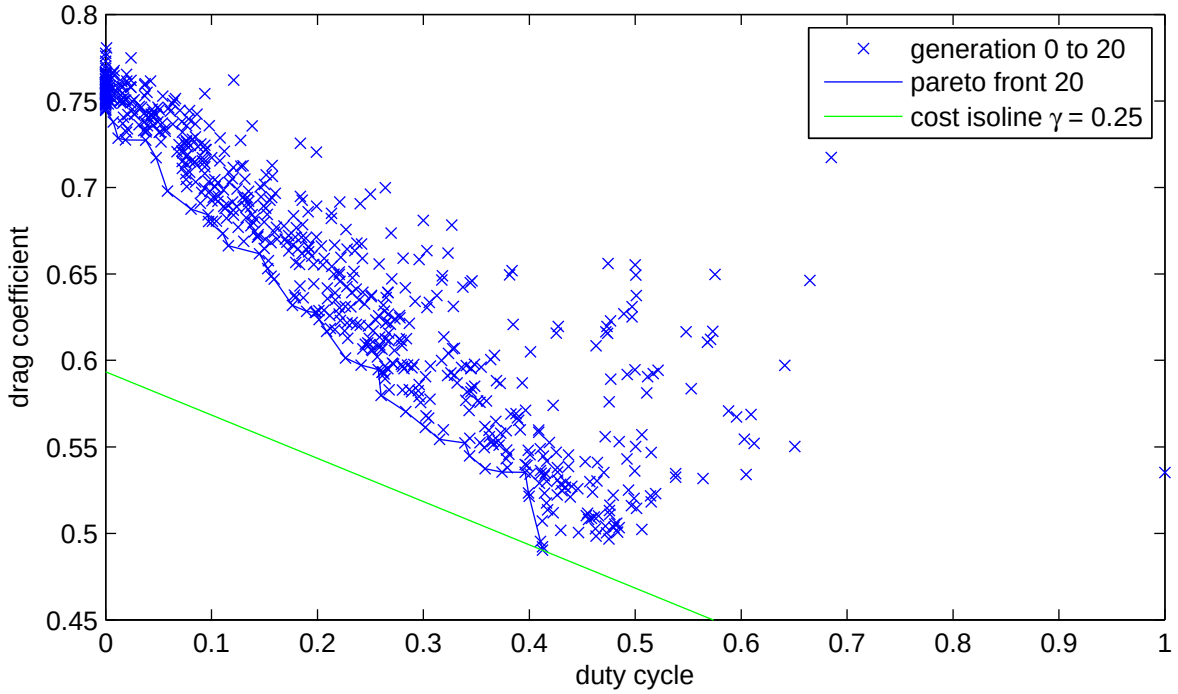

Figure 4.19: Pareto plot for multi-objective single output MLC run and with cost isoline for a weight $\gamma = 0.25$ fitted to corresponding single objective optimum

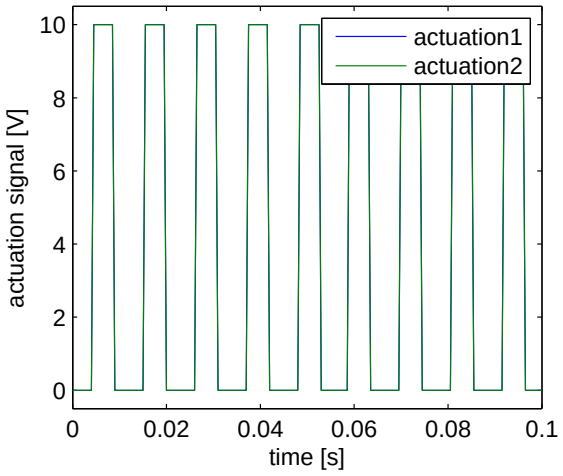

(a) actuation signals single-objective optimum

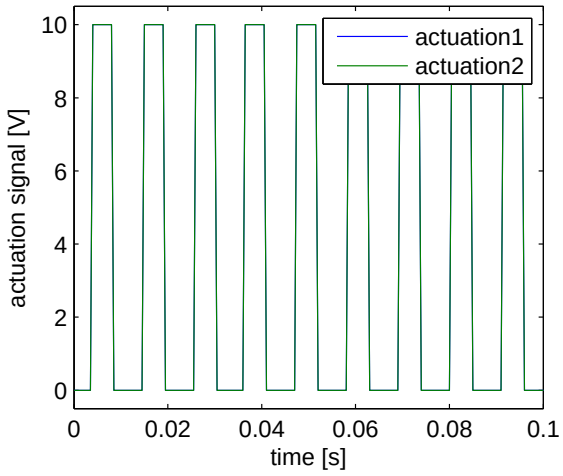

(b) actuation signals multi-objective optimum

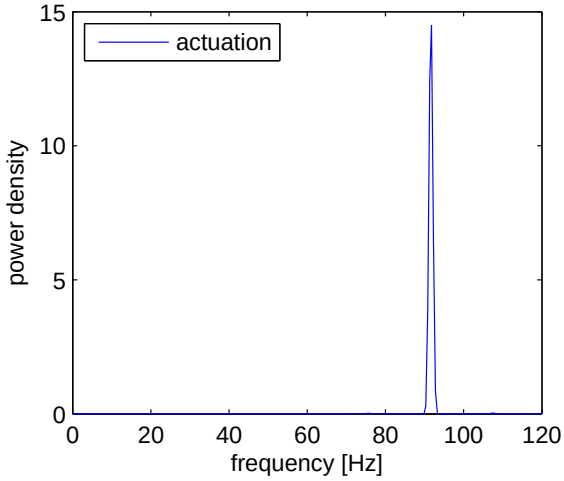

(c) actuation spectrum single-objective optimum

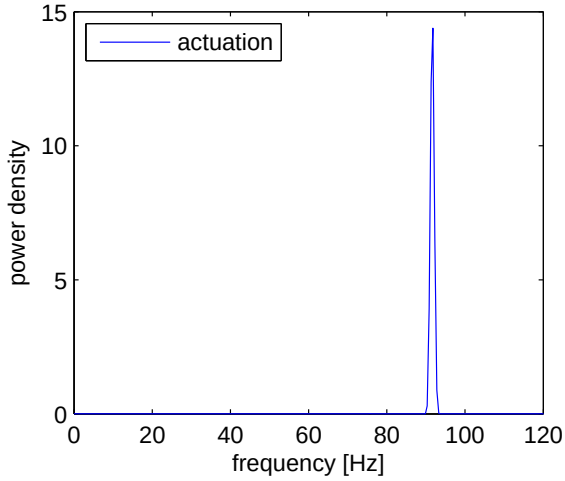

(d) actuation spectrum multi-objective optimum

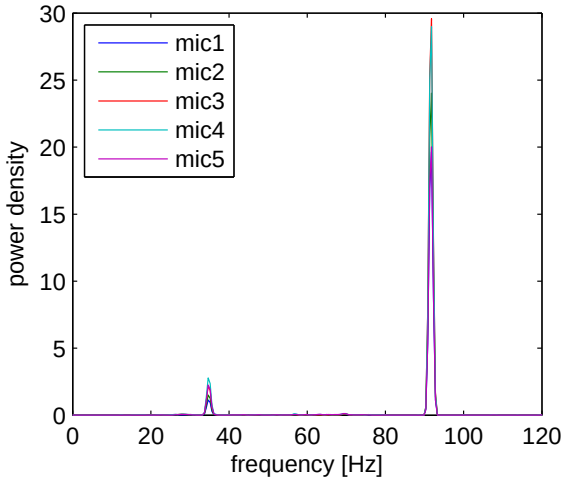

(e) microphone spectra single-objective optimum

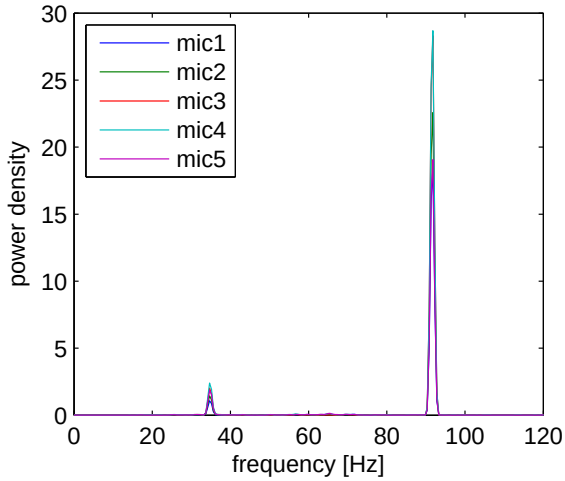

(f) microphone spectra multi-objective optimum

Figure 4.20: Comparison of the single-objective optimum to a corresponding multi-objective optimal individual by actuation signals and in- and output spectra. Single-objective on the left (a,c,e), mutli-objective on the right (b,d,f).

	control law	C_D	α	J
single-objective optimum for $\gamma = 0.25$	sinfnp2	0.499	0.412	0.602
multi-objective optimum for $\gamma = 0.25$	multiply(sinfnp2, stdd7)	0.490	0.412	0.593

Table 4.11: Comparison of the performance of the optimal individual found by a single-objective optimization run and one individual found by multi-objective optimization that is optimal with respect to the single-objective cost function

the optimal individual found by single objective optimization in figure 4.20 and table 4.11. Figure 4.20 shows a short time sequence of the actuation signals, the power spectral density of the actuation signals and the power spectral density of the microphone signals for the single objective optimum on the left hand side (subfigures a,c,e) and the optimum derived from the multi-objective optimization results on the right hand side (subfigures b,d,f). As the figures show, both solutions have virtually identical characteristics. Both show a periodic actuation signal with a clear single peak at 91.8 Hz in the actuation signal spectra and a dominating peak at the same frequency in the microphone spectra. Table 4.11 shows that the single-objective optimal control law is only using the artificial sine signal "sinfnp2" while the corresponding multi-objective optimum uses a slight variation, multiplying the same artificial sine signal with the standard deviation of one Kulite pressure sensor. The artificial sine signal has a frequency of 183.26 Hz, however, as the FPGA controller doesn't allow sufficiently state changes, the valves open and close on every second rising/falling face of the original sine signal, leading to an approximately halved actuation frequency. Both signals have the same duty cycle within the given accuracy. Nevertheless, the multi-objective optimum has a slightly lower drag coefficient. The modification of the artificial sine signal by multiplication with the standard deviation of a Kulite pressure sensors signal could slightly alter the switching moment at instants of particularly high or low fluctuation with little impact on the duty cycle but a small benefit in drag reduction. This would agree with observations made by Duriez et al. [9] that adjustment of the amplitude of a fixed frequency signal by a sensor signal can be beneficial. It is worth noting that the single-objective optimal control law does not use actual sensors and therefore implements open loop control. This is in agreement with what Parezanović et al. [23] expected as a possible result of the addition of an only timed-based signal.

The comparison shows that among the set of optima found by multi-objective optimization one can find an individual that is optimal with respect to a single objective cost function and similar to the optimum found by single-objective optimization based on the same cost function. This confirms that multi-objective optimization is a generalization of single-objective. The further sections will therefore focus on the MLC results obtained with multi-objectivity.

4.4.3 Investigation of individual control laws

4.4.3.1 Multi objective single output

To further the understanding of the optimization results, individuals along the Pareto front are investigated in more detail. Information on the performance in terms of the achieved drag coefficient and the duty cycle is combined with spectral analysis of the actuation signals and investigation of the used control laws themselves. This is done in this section for the results of multi objective optimization of single control laws controlling both blowing slots.

Figure 4.21 shows on the right hand side, a Pareto plot with all tested individuals and the resulting Pareto front. On the the left hand side, a short time sequence and the spectral power density of the actuation signal of three chosen individuals along the Pareto front are shown. These three individuals represent a trend that is visible throughout all of the 37 individuals on

the Pareto front. On the low drag coefficient end of the Pareto front, it is dominated by control laws that return a periodic, high frequency actuation command with a clear single frequency peak. Towards the middle of the Pareto front, the drag increases while the duty cycle decreases. Spectral analysis of the actuation signals show additional peaks at lower frequencies or even small bands of frequencies. Towards the high drag coefficient end of the Pareto front the duty cycle becomes close to zero and the actuation commands show no clear dominating frequencies anymore but a broad band of frequencies between zero and more than 100 Hz.

An overview of the control laws, performance and dominant frequencies is given in table 4.12. It is worth noting that the dominant frequency given here is that of the highest peak in the spectral analysis but not necessarily the only peak.

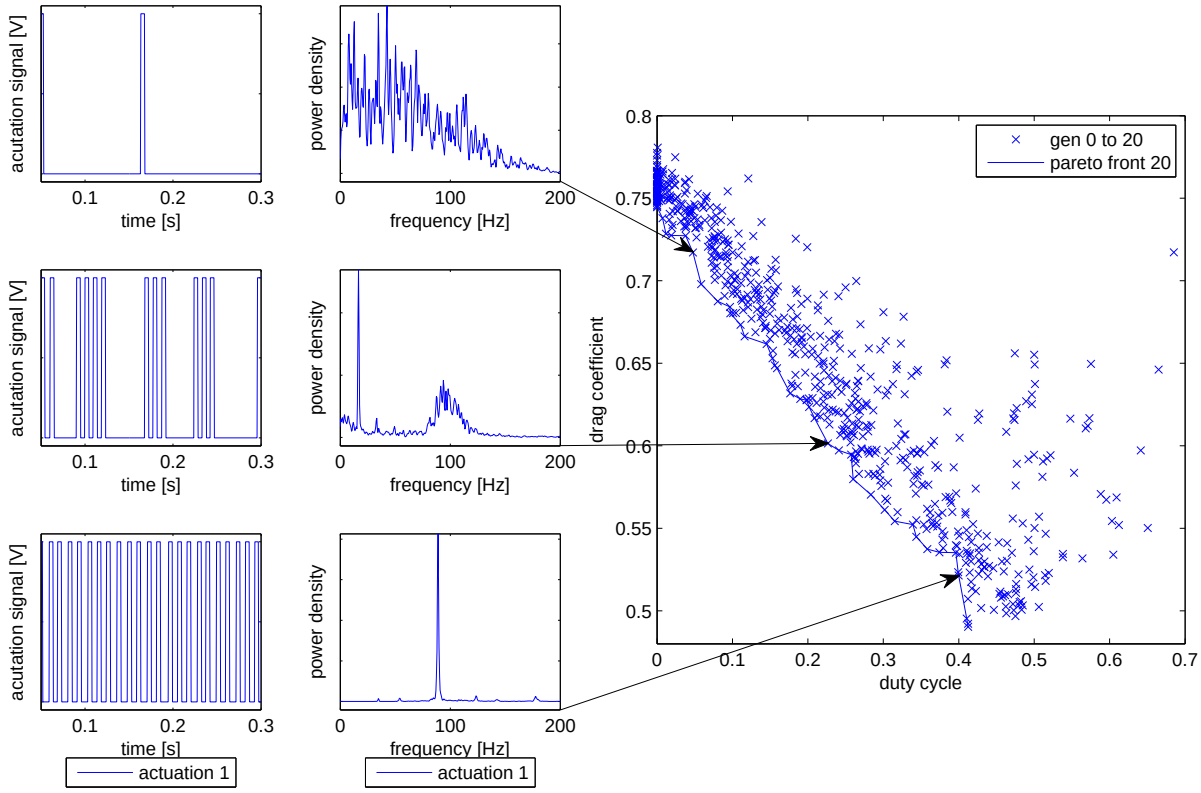

Figure 4.21: Pareto front for multi objective single output run and short actuation signal sequences and actuation spectra for chosen individuals

	control law	C_D	α	**dominant frequency**
individual 1	multiply(x6f, divide(x1mx2, xd7))	0.717	0.048	42.5 Hz
individual 2	multiply(x1mx2, subtract(divide ... ...(x1mx2, subtract(x6, xd1)), sinfnpm3))	0,601	0,227	16,6 Hz
individual 3	xd3	0,521	0.400	88,9 Hz

Table 4.12: Performance and characteristics of chosen individuals on the Pareto front for multi-objective single output optimization run

For further information on the control mechanisms it is helpful to look at the sensor and actuation signals. The microphone signals of the outermost microphones (mic1 and mic5) give a good indication of the temporal development of the base pressure and the vortex shedding process. Depending on the control law, further individual sensor signals can be important. For the actuation it is interesting to observe the direct output of the control law as well as the conditioned

actuation signal that is actually controlling the valves.

Figure 4.22 shows a short time frame of these signals for the control law of individual 1. The actuation is characterised by sparse, short moments of blowing. A single blowing cycle is seen to cause high amplitude base pressure oscillation for a short time before the pressure returns to unactuated levels. The control law output is seen to depend heavily on the level of the time delayed Kulite pressure sensor data "xd7" as it is standing in the denominator and heavily amplifies the signal amplitude when "xd7" is close to zero. Otherwise it attenuates the signal. As the pressure sensors measure relative to ambient pressure in the wind tunnel room and the pressure in the test section is lower than that, "xd7" oscillates around a negative value and the signal is attenuated most of the time. The microphone signals appear to loose their phase difference only for a short time span during actuation. This indicates that vortex formation is disturbed only very little, explaining the relatively high drag coefficient.

Figure 4.23 shows a short time frame of the signals for the control law of individual 2. The actuation is characterised by recurring spans of high frequency actuation, interrupted by spans without actuation. As seen before strong oscillation of the base pressure is measured by the microphones between the blowing cycles. A phase shift between the microphones is not visible. The control law output appears to be dominated by the artificial sine signal "sinfnpm3" that oscillates at 16.52 Hz between 0 V and 10 V. When the amplitude of the sine signal exceeds one it amplifies the pressure difference signal "x1mx2". The signal "x1mx2" is also present in the term of the control law that is unaffected by the sine signal but appears not to be strong enough to cause actuation without the amplification. While the sine signal is above one, the remaining pressure oscillations after one actuation period have a big enough impact on the control law to cause another actuation cycle. The control mechanism uses a fixed frequency signal to increase the sensitivity of the control law to pressure differences at model's base during limited time spans resulting in high frequency actuation during these times.

Figure 4.24 shows a short time frame of the signals for the control law of individual 3. The actuation is characterised by periodic actuation cycles at high frequency. The control law uses only the delayed signal of the middle microphone "xd3". It therefore uses almost direct feedback of the base pressure. As observed before, strong oscillation of the base pressure is measured by the microphones between the blowing cycles. The microphone signals drop steeply after the beginning of actuation with a slight time delay and increase again after the actuation is finished. The control law output follows the microphone signals with a small additional delay. An interdependency is formed where a blowing cycle causes pressure oscillations that trigger another blowing cycle. As expected, the resulting actuation at 88,9 Hz and 40 % duty cycle performs comparable to open loop control at a similar combination of frequency and duty cycle. The frequent actuation is likely to disturb the formation of large vortex structures.

For a complete understanding of what happens in the flow while a control law is active, a time resolved measurement of the velocity field in the wake of the model, e.g. a PIV measurement, would be helpful.

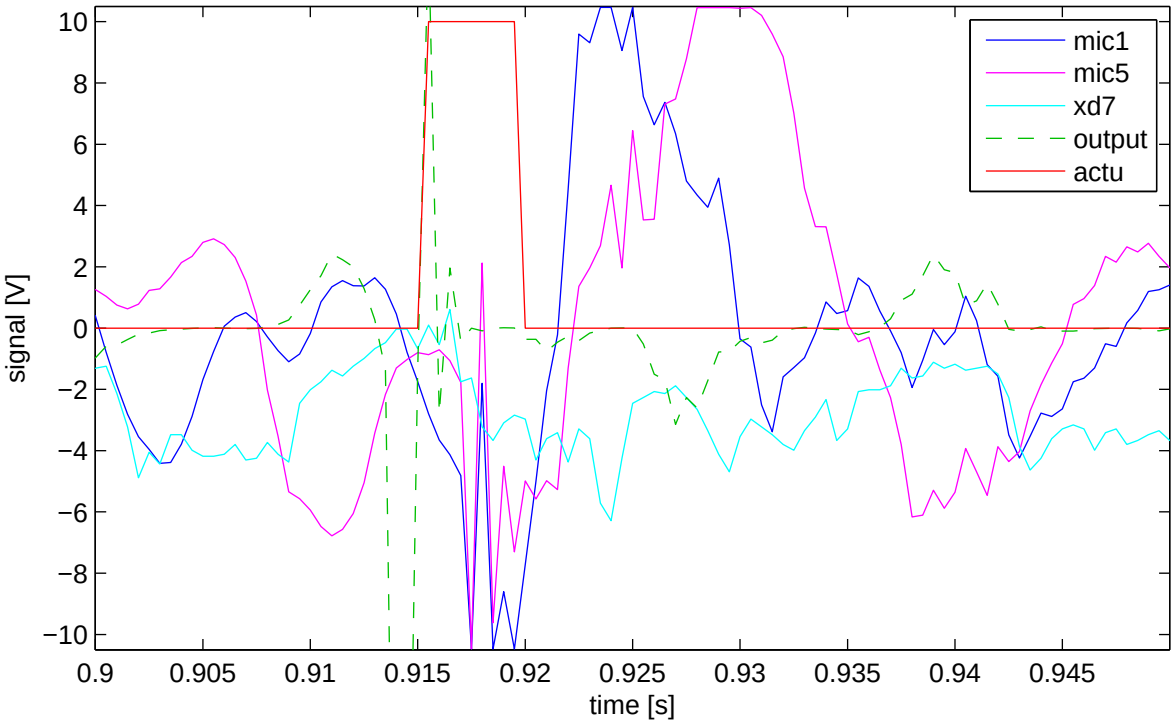

Figure 4.22: Short sequence of microphone, control law output and actuation signals for individual 1 from table 4.12 as part of the Pareto front for a multi-objective single output MLC run

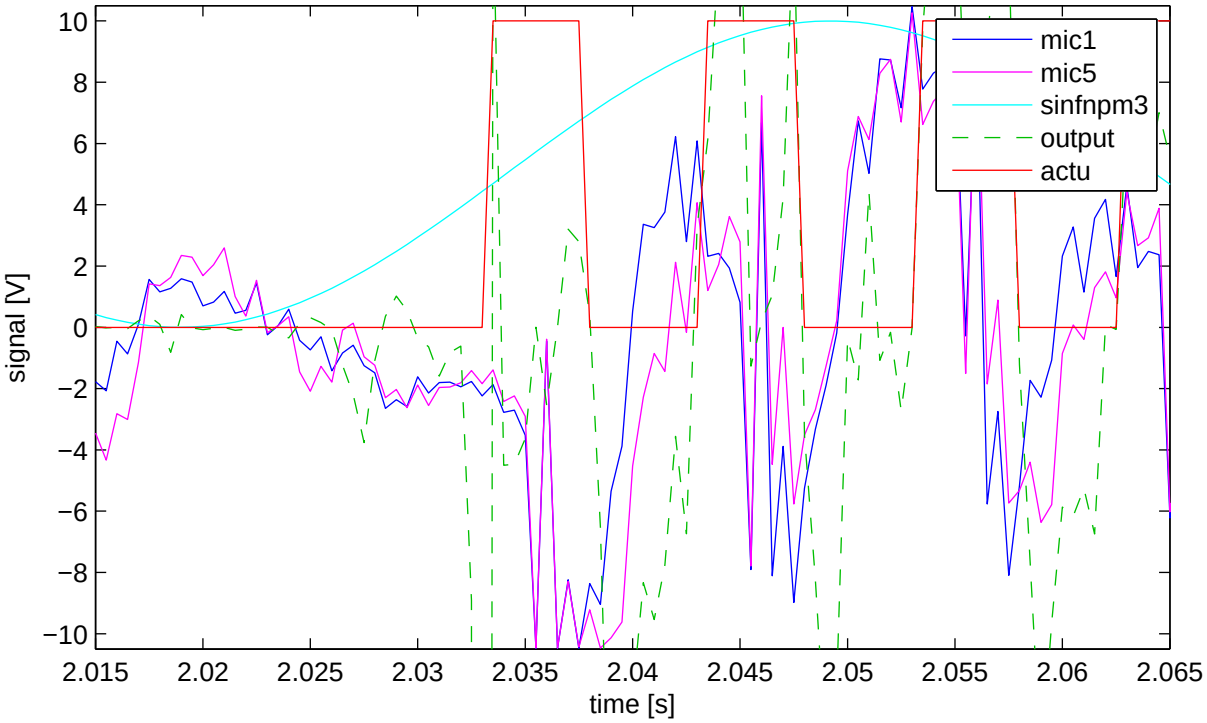

Figure 4.23: Short sequence of microphone, control law output and actuation signals for individual 2 from table 4.12 as part of the Pareto front for a multi-objective single output MLC run

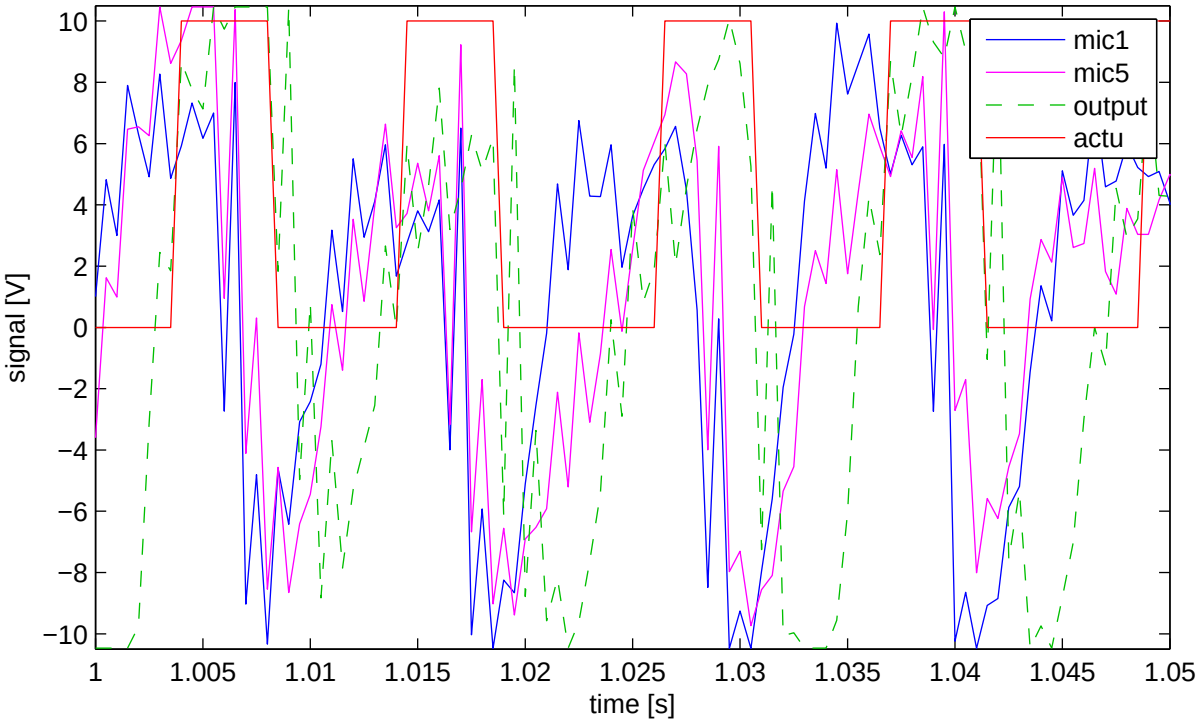

Figure 4.24: Short sequence of microphone, control law output and actuation signals for individual 3 from table 4.12 as part of the Pareto front for a multi-objective single output MLC run

4.4.3.2 Multi objective multiple output

This section provides a detailed investigation of the performance and characteristics of individuals along the Pareto front for results of multi objective optimization of two control laws controlling both blowing slots independently.

Figure 4.25 shows on the right hand side, a Pareto plot with all tested individuals and the resulting Pareto front. On the the left hand side, a short time sequence and the spectral power density of the actuation signal of three chosen individuals along the Pareto front are shown. These three individuals represent a trend that is visible throughout all of the 29 individuals on the Pareto front. The low drag coefficient end of the Pareto front is dominated by control laws that return a periodic, high frequency actuation command with a clear single frequency peak for both blowing slots. Towards the middle of the Pareto front, the drag increases while the duty cycle decreases. All individuals here use one-sided blowing from either just the upper or lower slot. Spectral analysis of the actuation signals show additional peaks at lower frequencies or even small bands of frequencies. Towards the high drag coefficient end of the Pareto front the duty cycle becomes close to zero and the actuation commands show no clear dominating frequencies anymore but a broad band of frequencies between zero and more than 100 Hz. The acutation is also just one-sided.

An overview of the two control laws per individual, performance and dominant frequencies is given in table 4.13. It is worth noting that the dominant frequency given here is that of the highest peak in the spectral analysis but not necessarily the only peak. A frequency of 0 Hz means no actuation. The duty cycle is calculated based on both actuation signals based on equation 2.23.

For further information on the control mechanisms, sensor and actuation signals are analysed.

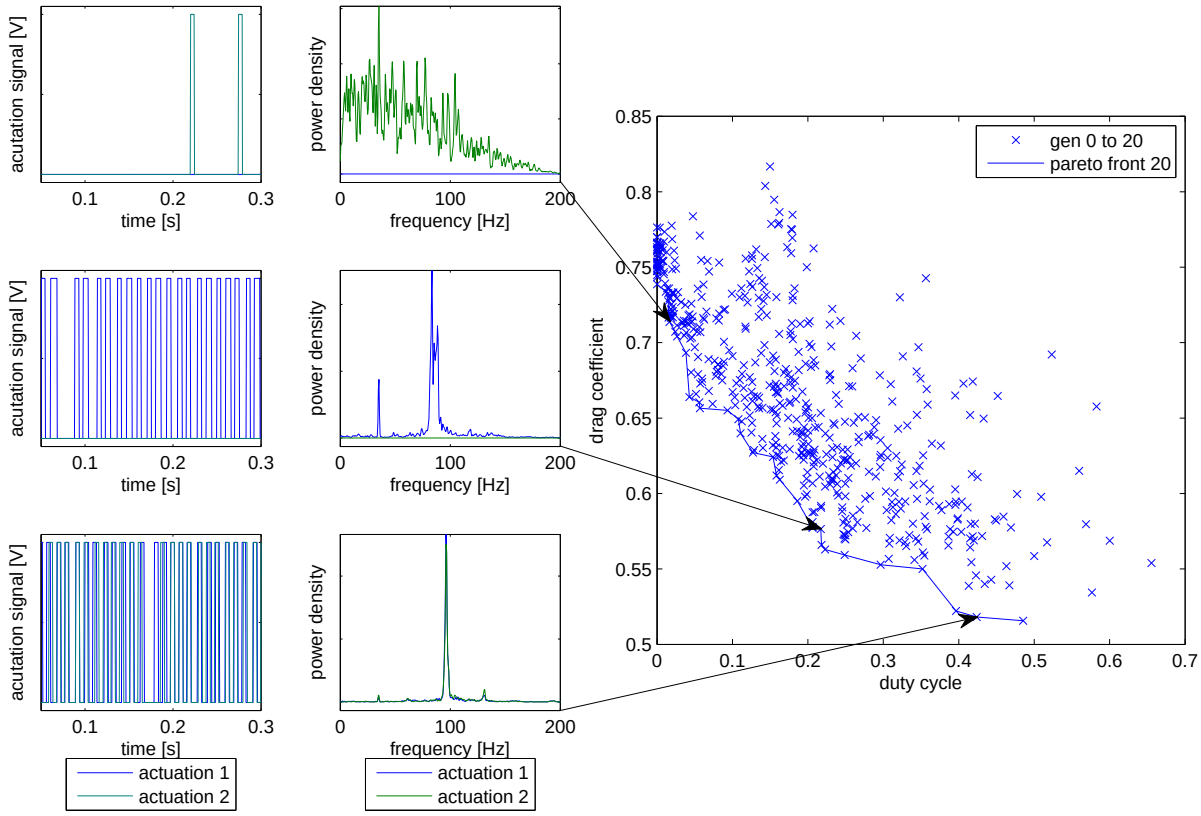

Figure 4.25: Pareto front for multi objective multiple output run and short actuation signal sequences and actuation spectra for chosen individuals

	control laws	C_D	α	**dominant frequency**
individual 1	subtract(x6, add(stdd3, stdd1))	0,714	0,017	0,0 Hz
	x1mx3			35,2 Hz
individual 2	multiply(x4f, stdd5)	0,576	0,217	83,5 Hz
	divide(x5, stdd5)			0,0 Hz
individual 3	subtract(x5, divide(xd5, x7))	0,518	0,424	96,2 Hz
	add(x3mx5, x5)			96,2 Hz

Table 4.13: Performance and characteristics of chosen individuals on the Pareto front for multi-objective multiple output optimization run

As for section 4.4.3.1, the outer microphone signals, the control law outputs and the conditioned actuation signals are of interest. In contrast, now there are two different control law outputs and two actuation signals for every individual. For better clarity the output signals are shown in separate plots in figures 4.26 to 4.28. Each plot does contain both actuation signals however, as they provide necessary context for the behaviour of the microphone signals.

Figure 4.26 shows a short time frame of the signals for the control laws of individual 1. The actuation is characterised by sparse, short blowing cycles from only one side. The microphone signals show oscillations with increasing amplitude and a clear phase shift, indicating alternating vortex shedding during the unactuated period. The first control law is made of a mostly negative Kulite pressure sensor signal "x6" from which strictly positive standard deviation signals are subtracted, leading to a negative control law output that never triggers actuation. The second control law consists of only a microphone difference signal that increases in amplitude with the out of phase microphone signals until it is large enough to trigger an actuation. As the microphones respond in phase to the start of the blowing, the difference signal is decreased again and the blowing stops quickly. The control mechanisms lets vortex structures build up to certain strength before it interrupts them by a short blow. This needs very little blowing but allows vortex formation to a certain degree, explaining the low drag reduction but also low duty cycle.

Figure 4.27 shows a short time frame of the signals for the control laws of individual 2. The actuation is characterised by periodic, high frequency actuation from one side. The oscillation of the microphone signals is dominated by the blowing cycles. As the blowing is only one-sided, the response of the microphones differs in amplitude. Control law one consists of a filtered microphone signal "x4f" multiplied with the standard deviation of the microphone 5, "stdd5". At times of high fluctuation, the multiplication with the standard deviation signal further amplifies the oscillating microphone signal. As seen for previous high frequency actuation control laws, an interdependency between blowing cycles and pressure oscillation forms. The frequency is slightly lowered by the time delay introduced by the filtering in the signal "x4f". The second control law consists of the microphone signal "x5" divided by its standard deviation. The division by the standard deviation leads to attenuation of the output signal during times of high signal fluctuation caused by the frequent blowing cycles triggered by the first control law. The second control law output therefore remains too low to trigger an actuation.

Figure 4.28 shows a short time frame of the signals for the control laws of individual 3. The actuation is characterised by periodic, high frequency actuation from both sides. The actuation is mostly synchronous, sometimes actuation signal 1 shows a low positive phase shift. Both control laws are dominated by feedback of microphone signals which, as seen before, cause self sustained high frequency actuation. The occasional delay of the first actuation signal relative to the second can be explained with the first control law containing a delayed microphone signal also.

A very interesting result of the analysis of the Pareto front individuals is that, given the option to control both slots separately, most Pareto front individuals only used one slot. One sided blowing has shown to be an efficient drag reduction method that is outperformed by two sided blowing only for very low drag coefficients. Figure 4.29 shows the Pareto fronts for multi-objective optimization of control laws with one and two outputs. Except for the low drag-coefficient end of the Pareto fronts, individuals with separate control of both slots achieved the same drag coefficients at lower duty cycles. All of those individuals implemented one-sided actuation.

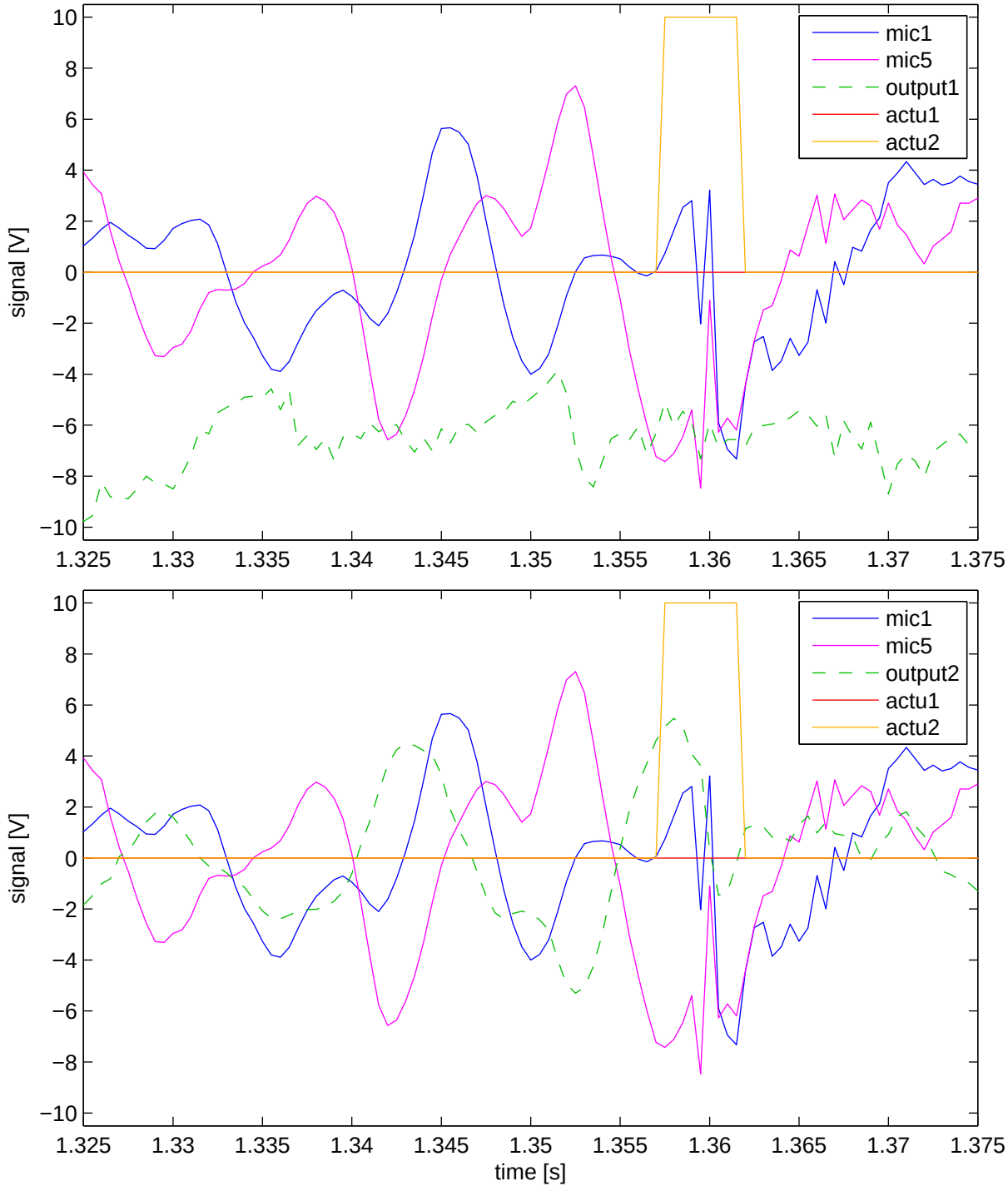

Figure 4.26: Short sequence of microphone, control law output and actuation signals for individual 1 from table 4.13 as part of the Pareto front for a multi-objective multiple output MLC run, split in upper plot containing the output of the first control law and lower plot containing the output of the second control law

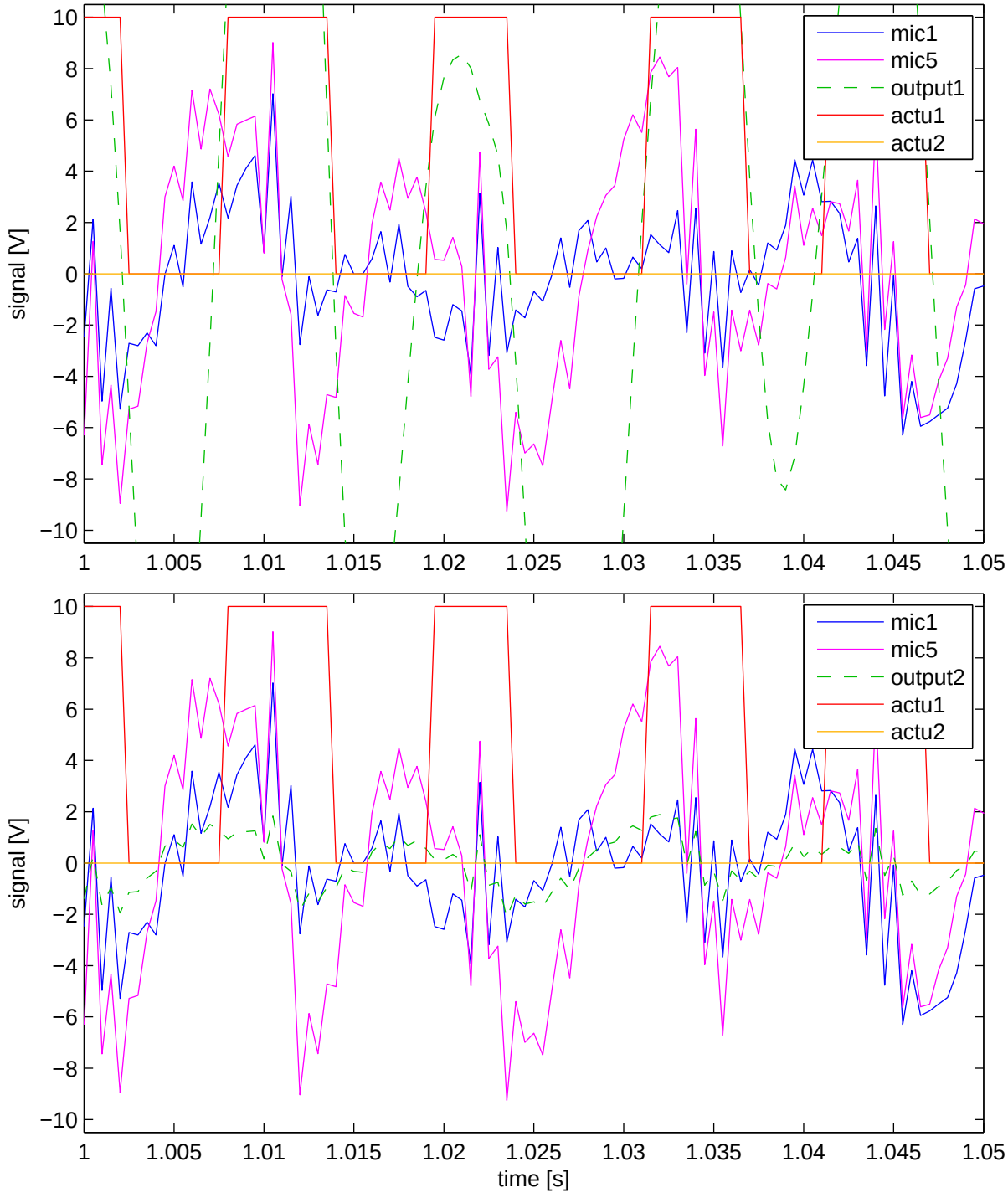

Figure 4.27: Short sequence of microphone, control law output and actuation signals for individual 2 from table 4.13 as part of the Pareto front for a multi-objective multiple output MLC run, split in upper plot containing the output of the first control law and lower plot containing the output of the second control law

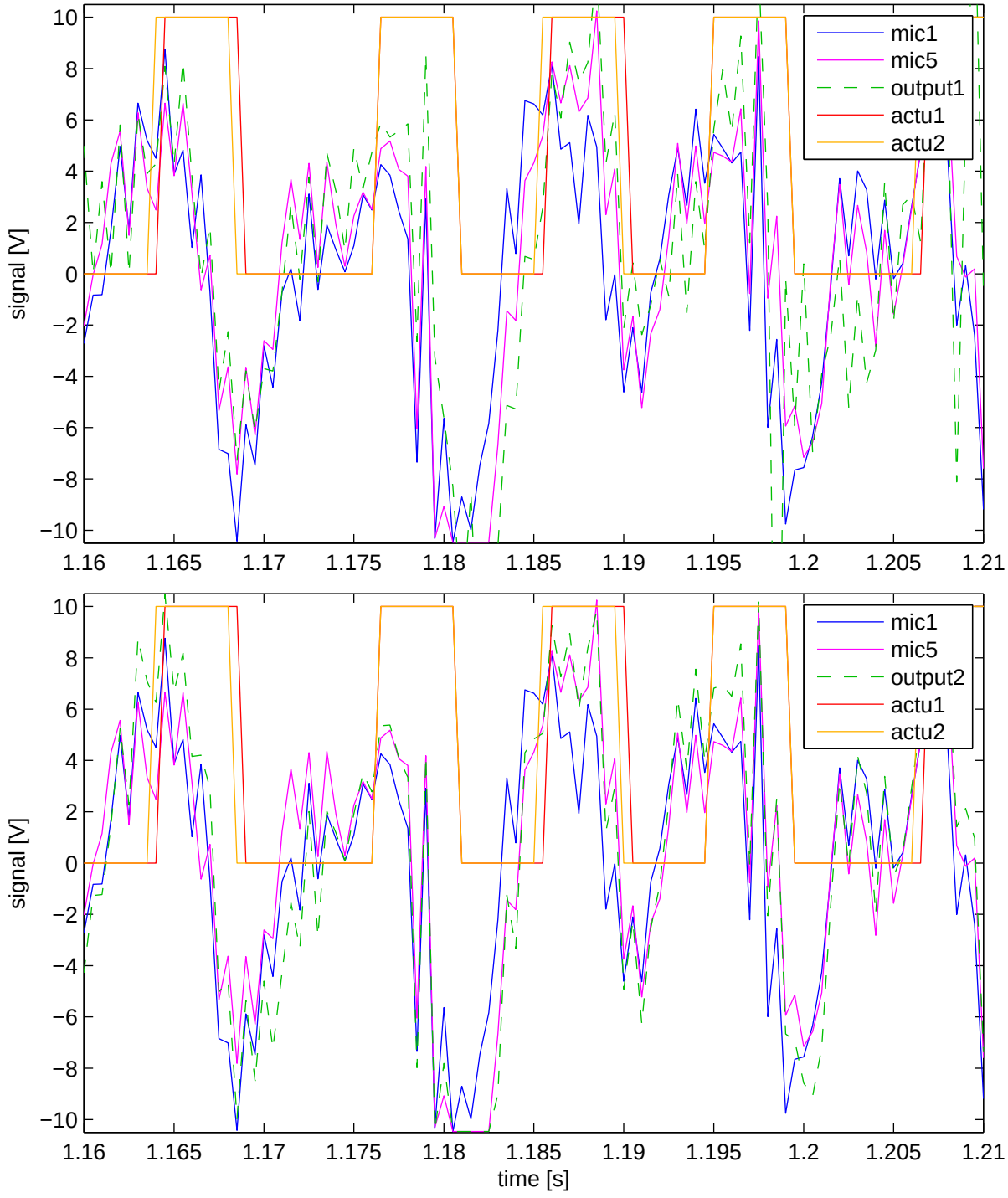

Figure 4.28: Short sequence of microphone, control law output and actuation signals for individual 3 from table 4.13 as part of the Pareto front for a multi-objective multiple output MLC run, split in upper plot containing the output of the first control law and lower plot containing the output of the second control law

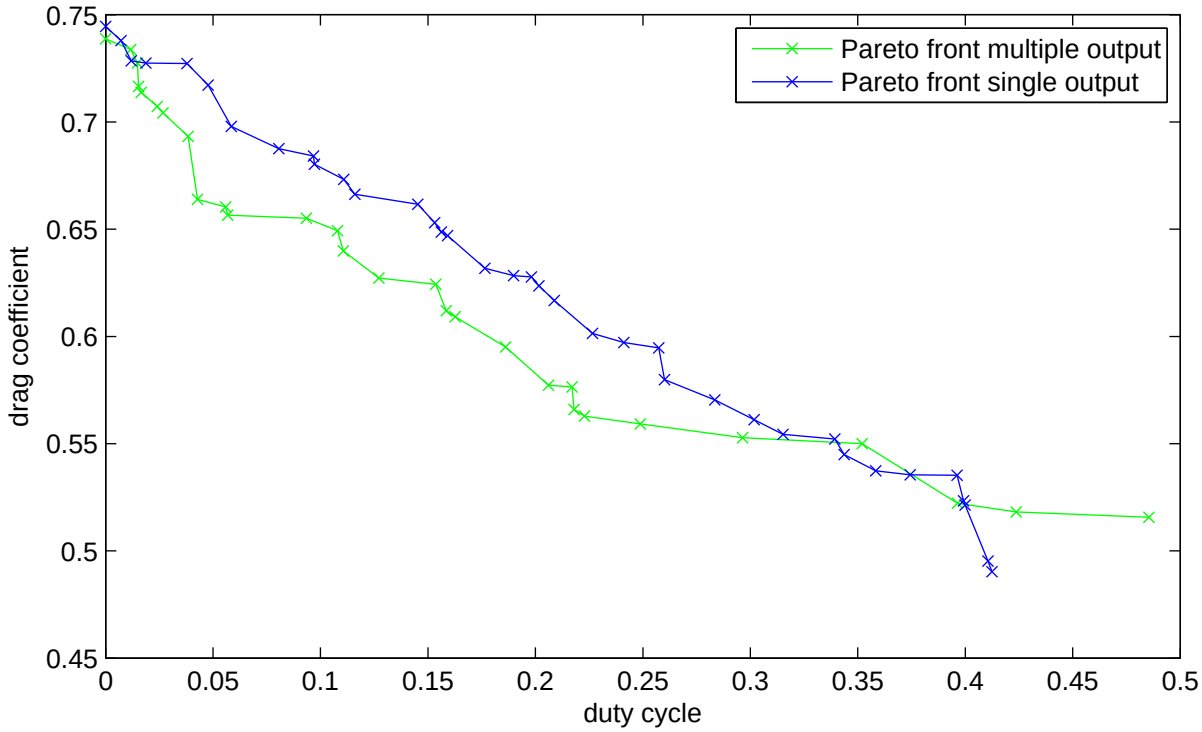

Figure 4.29: Comparison of the Pareto fronts for both multi-objective MLC runs, with single and multiple control outputs

4.4.4 Control landscapes

Plotting the control landscape for a set of individuals reveals the degree of similarity between their control laws. First, a suitable distance metric has to be chosen to determine a value for the distance or dissimilarity between the control laws of two individuals. In this investigation a variation of the distance metric suggested by Kaiser et al. [20] is used. The distance between two individuals is determined based on their actuation signals by the formula

$$D_{i,j} = \left\| \sum_{t=0}^{T_{test}} (\mathbf{b}_i(t) - \mathbf{b}_j(t))^2 \right\|, \tag{4.1}$$

with $D_{i,j}$ being the distance between individuals i and j, $b_i(t)$ being the vector of actuation signal values of individual i at the time t and T_{test} the period for which the individuals are tested. Calculation of the distances between all pairwise combinations of individuals of one MLC run gives a distance matrix D. Then, multi-dimensional scaling is used to find a set of two-dimensional coordinates $\boldsymbol{\beta}_i$ for each individual so that the distances between all individuals are preserved optimally in the two-dimensional space. Mathematically this means a minimisation of the error term $\epsilon_{i,j}$ in

$$\|\boldsymbol{\beta}_i - \boldsymbol{\beta}_j\| = D_{i,j} + \epsilon_{i,j}. \tag{4.2}$$

The coordinates are determined using the "mdscale" function provided by MatLab. To link the information of the position of an individual in the two-dimensional plane with it's performance, each circle representing one individual in the plot of the control landscape is colour-coded. The colour-code is based on the achieved drag coefficient of on individual relative to the others. An individual with a lower drag-coefficient than 100 % of the others is coloured white. An individual with a lower drag coefficient than 0 % of the others is coloured black. All percentiles in between are coloured in grey scales.

Figure 4.30 shows the control landscape for a multi objective single output MLC run. It can be seen that most individuals are close to a line of $\beta_2 = 0$. The majority of individuals with low drag coefficient are close a point of $[\beta_1\ \beta_2] = [2\ 0] \cdot 10^5$, indicating that they all had rather similar actuation signals. Most individuals with high drag are found at negative β_1. They are more scattered, suggesting that many different actuation signals have been tested that were unsuccessful in reducing drag.

Figure 4.31 shows the control landscape for a multi objective single output MLC run. The individuals appear to be more scattered than in figure 4.30 indicating that more different control mechanisms have been tested. This appears sensible as the combination of two control laws allows more variation. Individuals with low drag coefficients are found mostly in proximity to $[\beta_1\ \beta_2] = [2\ 0] \cdot 10^5$. Individuals with high drag coefficient are scattered wider, suggesting that again many different actuation signals have been tested that were unsuccessful in reducing drag.

Deeper analysis of a physical meaning of the coordinates could provide further insight in the characteristics of successful individuals. As stated by Duriez et al [9], the understanding of the topology of a control landscape is still subject of active research.

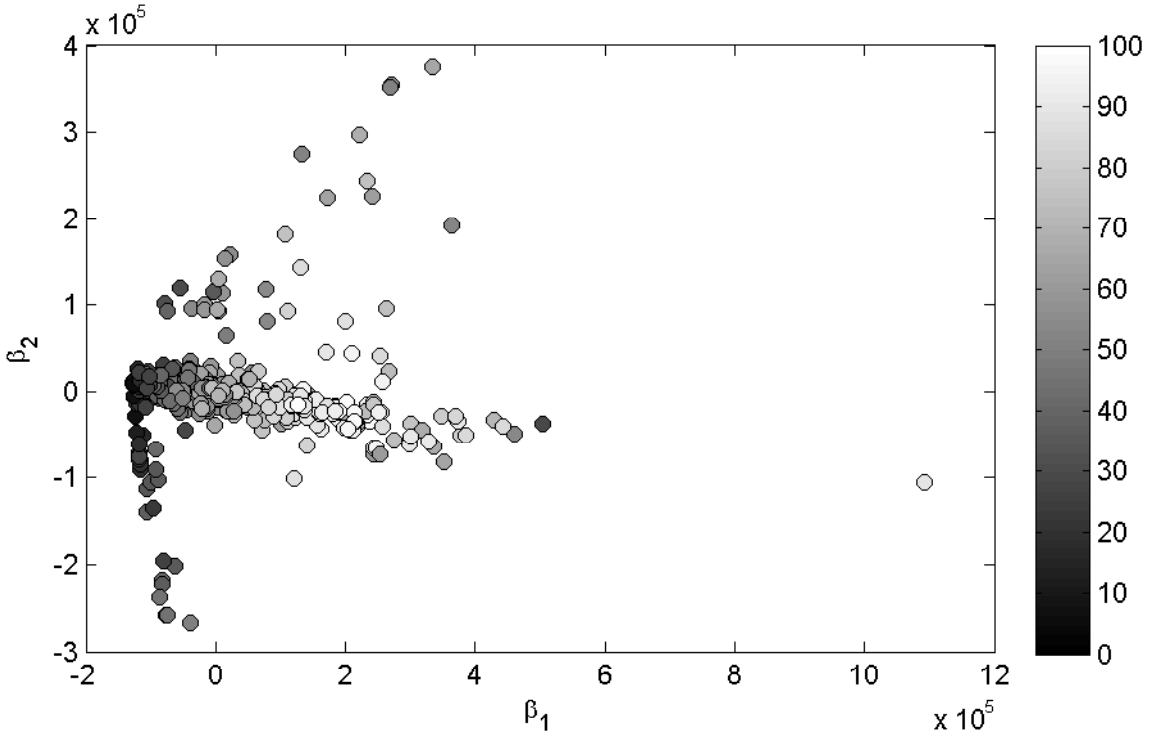

Figure 4.30: Control landscape of all individuals of a multi objective single output MLC run

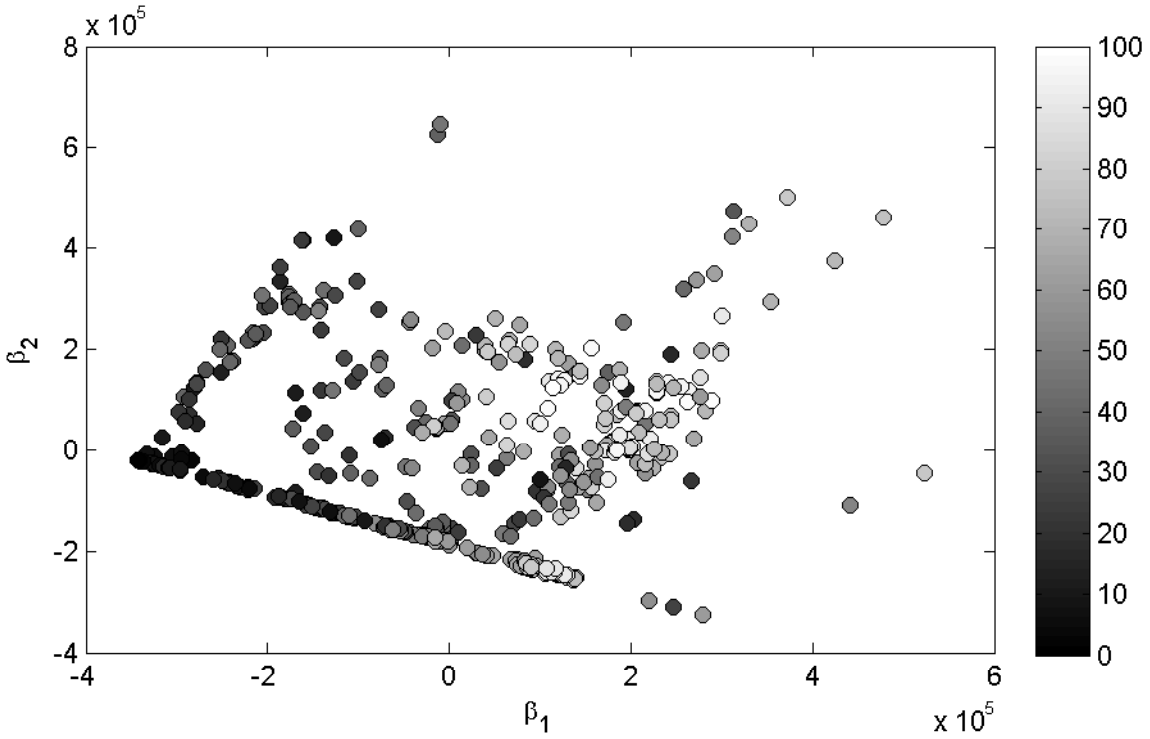

Figure 4.31: Control landscape of all individuals of a multi objective multiple output MLC run

Chapter 5

Conclusion

Drag measurements for the base configuration of a D-shaped bluff body and configurations with passive and active drag-reducing devices were undertaken. Active drag reduction was realized through open loop control and closed loop control. Closed loop control laws were optimized through genetic programming, implementing machine learning control. To enable machine learning control, a robust, automated drag determination strategy was found through curve fitting of the total and static wake pressure distributions. Furthermore a fast and reliable controller was implemented on an FPGA and integrated in the experimental setup. The duty cycle could be shown to be a good measure for invested actuation energy in case of an unknown momentum coefficient. Analysis of the results was done by comparison of achieved drag reduction, invested actuation energy, spectral analysis of sensor and actuation signals, Pareto plots and control landscapes.

The tested passive drag-reducing devices have shown a drag reduction of up to 40 %. In contrast to the base configuration, a dependence of the drag coefficient on the Reynolds number has been observed. All but one device showed a clear decrease of drag with increasing Reynolds number. Comparison passive trailing edge flaps of polynomial shape with numerical simulations indicated that the simulation accurately captured the drag-reducing mechanisms.

Open loop actuation was found to yield drag reduction of up to 43 % under an ideal combination of actuation frequency and duty cycle. Actuation close to the natural vortex shedding frequency or a sub-harmonic was found to increase drag over the unactuated case due to amplification of the natural shear layer instability. Comparison of different blowing intensities based on supply tank pressures has shown the highest drag reduction at the highest tank pressure. The performance of numerical simulation for the same setup could not be matched.

The drag reduction of the best closed loop control laws was found to match that of the best open loop actuation. Closed loop control laws often achieved the similar drag reduction at lower actuation cost. One control law achieved just 1 % higher drag at an 18 % lower duty cycle. Control laws that achieved the lowest drag reduction often showed actuation at a single, high frequency. This resulted either from control laws based on small modifications of an artificial sine sensor signal or control laws dominated by direct feedback of a microphone signal. Control laws based on direct feedback appeared to sustain high frequency actuation by locking on a resonance frequency. Further analysis should be undertaken to investigate if the resonance is an interaction with the flow field or if MLC has found a way to exploit resonance with parts of the experimental setup. Control laws that yielded higher drag reductions but were still found to be Pareto optimal were found to primarily use one sided actuation as a very efficient drag-reducing mechanism.

Bibliography

[1] PW Bearman. The effect of base bleed on the flow behind a two-dimensional model with a blunt trailing edge. *The Aeronautical Quarterly*, 18(3):207–224, 1967.

[2] Christopher M Bishop. *Pattern recognition and machine learning*. springer, 2006.

[3] Steven L Brunton and Bernd R Noack. Closed-loop turbulence control: Progress and challenges. *Applied Mechanics Reviews*, 67(5):050801, 2015.

[4] Timothée Chabert, Julien Dandois, and Éric Garnier. Experimental closed-loop control of flow separation over a plain flap using slope seeking. *Experiments in fluids*, 55(8):1797, 2014.

[5] Jeremy A Dahan, AS Morgans, and S Lardeau. Feedback control for form-drag reduction on a bluff body with a blunt trailing edge. *Journal of Fluid Mechanics*, 704:360–387, 2012.

[6] L Dalla Longa, AS Morgans, and JA Dahan. Reducing the pressure drag of a d-shaped bluff body using linear feedback control. *Theoretical and Computational Fluid Dynamics*, pages 1–11, 2017.

[7] Kalyanmoy Deb, Amrit Pratap, Sameer Agarwal, and TAMT Meyarivan. A fast and elitist multiobjective genetic algorithm: Nsga-ii. *IEEE transactions on evolutionary computation*, 6(2):182–197, 2002.

[8] Antoine Debien, Kai AFF von Krbek, Nicolas Mazellier, Thomas Duriez, Laurent Cordier, Bernd R Noack, Markus W Abel, and Azeddine Kourta. Closed-loop separation control over a sharp edge ramp using genetic programming. *Experiments in fluids*, 57(3):40, 2016.

[9] Thomas Duriez, Steven L Brunton, and Bernd R Noack. *Machine Learning Control-Taming Nonlinear Dynamics and Turbulence*. Springer, 2017.

[10] Kurt Frey. Verminderung des strömungswiderstandes von körpern durch leitflächen. *Forschung im Ingenieurwesen*, 4(2):67–74, 1933.

[11] Nicolas Gautier, J-L Aider, Thomas Duriez, BR Noack, Marc Segond, and Markus Abel. Closed-loop separation control using machine learning. *Journal of Fluid Mechanics*, 770:442–457, 2015.

[12] D Geropp and H-J Odenthal. Drag reduction of motor vehicles by active flow control using the coanda effect. *Experiments in fluids*, 28(1):74–85, 2000.

[13] JH Gerrard. The mechanics of the formation region of vortices behind bluff bodies. *Journal of fluid mechanics*, 25(2):401–413, 1966.

[14] David Greenblatt and Israel J Wygnanski. The control of flow separation by periodic excitation. *Progress in aerospace Sciences*, 36(7):487–545, 2000.

[15] Lars Henning. *Regelung abgelöster Scherschichten durch aktive Beeinflussung*. Dissertation, TU Berlin, 2008.

[16] T. Hofmacher. Einfluss von transitionsstreifen auf den profilwiederstand bei kleinen reynoldszahlen, 2016. Bachelorarbeit Nr. 683.

[17] Edward Lewis Houghton and Peter William Carpenter. *Aerodynamics for engineering students*. Butterworth-Heinemann, 2003.

[18] WH Hucho. *Aerodynamik der stumpfen Körper, 2. Auflage, Vieweg+ Teubner*. Springer, Wiesbaden, Germany, 2011.

[19] Thomas B Johansson, Anand Prabhakar Patwardhan, Nebojša Nakićenović, and Luis Gomez-Echeverri. *Global energy assessment: toward a sustainable future*. Cambridge University Press, 2012.

[20] Eurika Kaiser, Bernd R Noack, Andreas Spohn, Louis N Cattafesta, and Marek Morzynski. Cluster-based control of nonlinear dynamics. *arXiv preprint arXiv:1602.05416*, 2016.

[21] Alfred Leder. *Abgelöste Strömungen: physikalische Grundlagen*. Springer, 1992.

[22] S Luke. Essentials of metaheuristics. a set of undergraduate lecture notes. (online version 2.2). department of computer science, george mason university, october 2015, 2015.

[23] Vladimir Parezanović, Jean-Charles Laurentie, Carine Fourment, Joël Delville, Jean-Paul Bonnet, Andreas Spohn, Thomas Duriez, Laurent Cordier, Bernd R Noack, Markus Abel, et al. Mixing layer manipulation experiment. *Flow, Turbulence and Combustion*, 94(1):155–173, 2015.

[24] Mark Pastoor, Lars Henning, Bernd R Noack, Rudibert King, and Gilead Tadmor. Feedback shear layer control for bluff body drag reduction. *Journal of fluid mechanics*, 608:161–196, 2008.

[25] Anatol Roshko. On the drag and shedding frequency of two-dimensional bluff bodies. 1954.

[26] B. Shao. Experimental investigation on a d-shaped bluff body with passive and active drag-minimizing devices, 2016. Bachelorarbeit Nr. 699.

[27] J. Stollenwerk. Shape optimization of a d-shaped bluff body. Studienarbeit, Institut für Strömungsmechanik, TU Braunschweig, 2016.

[28] M Tanner. Reduction of base drag. *Progress in Aerospace Sciences*, 16(4):369–384, 1975.

[29] N Tombazis and PW Bearman. A study of three-dimensional aspects of vortex shedding from a bluff body with a mild geometric disturbance. *Journal of Fluid Mechanics*, 330:85–112, 1997.

[30] Stephen A Whitmore and Jonathan W Naughton. Drag reduction on blunt-based vehicles using forebody surface roughness. *Journal of spacecraft and rockets*, 39(4):596–604, 2002.

[31] Ming-Hsun Wu, Chih-Yung Wen, Ruey-Hor Yen, Ming-Cheng Weng, and An-Bang Wang. Experimental and numerical study of the separation angle for flow around a circular cylinder at low reynolds number. *Journal of Fluid Mechanics*, 515:233–260, 2004.

List of Figures

List of Tables

List of Algorithms

Appendix A

Codes

A.1 Drag calculation

```
function [Cd] = wake(pressure)

% separate pressures
total_pressure = pressure(1:22);
static_pressure = pressure(28:32);

% positions as designed
position_pitot = 0:9:9*21;
position_prandtl = [0:40:160] + 14.5;

% fit total pressure
data = total_pressure;
pos = position_pitot;
[~,id] = min(data);
middle = pos(id);
beta = [0.001,-0.001,min(data),max(data),-middle];
formula1 = @(beta,x) (1+beta(1).*(x+beta(5)).^2) .* exp(beta(2).*(x+beta(5)
    ).^2) * (beta(3) - beta(4)) + beta(4);
[beta1,R1,~,~,~,~] = nlinfit(pos,data,formula1,beta);
display(mean(abs(R1/data(:,2))))

% fit static pressure
data = static_pressure;
pos = position_prandtl;
beta = [min(data),max(data),beta1(5)];
formula2 = @(beta,x) (1+beta1(1).*(x+beta(3)).^2) .* exp(beta1(2).*(x+beta
    (3)).^2) * (beta(1) - beta(2)) + beta(2);
[beta2,R2,~,~,~,~] = nlinfit(pos,data,formula2,beta);
display(mean(abs(R2/data(:,2))))

% calculate Cd
dyn_pressure_fs = beta1(4) - beta2(2);
static_pressure_fs = beta2(2);
ref_length = 0.0534;

fun = @(x) (2 * sqrt((formula1(beta1,x) - formula2(beta2,x)) /
    dyn_pressure_fs) .* (1 - sqrt((formula1(beta1,x) - static_pressure_fs) /
     dyn_pressure_fs)));
Cd = integral(fun,min(position_prandtl),max(position_prandtl))/1000/
    ref_length;
```

```
36
37 % plot
38 x = linspace(min(position_pitot),max(position_pitot),51);
39 ref_length = ref_length * 1000;
40 x_plot = (x + beta1(5)) / ref_length;
41 position_pitot_plot = (position_pitot + beta1(5))/ref_length;
42 position_prandtl_plot = (position_prandtl + beta1(5))/ref_length;
43
44 figure()
45 plot(position_pitot_plot,total_pressure,'x',position_prandtl_plot,
       static_pressure,'x',x_plot,formula1(beta1,x),x_plot,formula2(beta2,x))
46
47 title(['Cd:␣',num2str(Cd)])
48 ylabel('\Delta␣p␣[Pa]')
49 xlabel('y/d')
50 set(gca,'box','on')
51 legend('p_0␣data', 'p␣data', 'p_0␣fit','p␣fit','location','northeastoutside
       ')
52
53 end
```